BUBBLE COMPRESSION AND CONDENSATION IN SINGLE COMPONENT CO-CURRENT DOWNFLOW

by

IAN I CHANG

B.A.Sc., The University of British Columbia, 1983

A THESIS SUBMITTED IN PARTIAL FULFILLMENT OF

THE REQUIREMENTS FOR THE DEGREE OF

MASTER OF APPLIED SCIENCE

in

THE FACULTY OF GRADUATE STUDIES

Department of Mechanical Engineering

We accept this thesis as conforming

to the required standard

THE UNIVERSITY OF BRITISH COLUMBIA

October, 1986

In presenting this thesis in partial fulfilment of the requirements for an advanced degree at the University of British Columbia, I agree that the Library shall make it freely available for reference and study. I further agree that permission for extensive copying of this thesis for scholarly purposes may be granted by the head of my department or by his or her representatives. It is understood that copying or publication of this thesis for financial gain shall not be allowed without my written permission.

Department of Mechanical Engineering

The University of British Columbia
1956 Main Mall
Vancouver, Canada
V6T 1Y3

Date October 15, 1986

ABSTRACT

In an investigation of the process termed hydraulic vapour compression (HVC), a photographic study of bubble compression and condensation rates in single component co-current downflow has been performed. Supplemental to the photographic study, measurements of the deliverable mass flowrates of the HVC process were also carried out.

The downward flow of a gas and liquid mixture, as occurs in the HVC process, results in the compression of the gas phase because of the increasing hydraulic pressure. Bubble compression heating provides the driving temperature difference for both heat and mass transfer to occur. The minimization of the transfer processes is desirable to ensure a high compression efficiency.

Experiments were carried out using near saturated Freon-11 in a 2.54 cm I.D., 1.7 m long glass downcomer. Bubbles were filmed during travel along the downcomer. Histories of the decrease in individual bubble size were determined from silhouette traces obtained from sequenced single frames selected from the exposed films. Bubble volumes and surface areas were inferred by numerically revolving digitized images of the traces about their principal centroidal axes. The inferred volumes and surface areas provided the basis upon which heat and mass transfer rates were calculated. Delivered vapour mass flowrates were measured by hot film anemometry.

Results showed that mass condensation rates increased along the length of the downcomer. Local external Nusselt numbers used to characterize the transfer processes at the bubble wall, ranged from 0.1 to 16. The deliverable mass flowrates achieved by the HVC process were found to be comparable to those produced by the well known process of hydraulic air compression.

TABLE OF CONTENTS

TABLE OF CONTENTS (Continued)

LIST OF TABLES

LIST OF FIGURES

LIST OF FIGURES (Continued)

LIST OF FIGURES (Continued)

LIST OF FIGURES (Continued)

NOMENCLATURE

A	calibration constant in King's law
A_b	bubble surface area [m^2]
A_{ex}	vapour exhaust tube cross section area [m^2]
B	calibration constant in King's law
c_p	liquid specific heat capacity [J/kg °C]
D_{se}	bubble spherical equivalent diameter based on the ratio of volume to surface area [m]
D_{sev}	bubble spherical equivalent diameter based solely on volume [m]
e_g	vapour specific internal energy corresponding to the local pressure [J/kg]
e_ℓ	liquid specific internal energy corresponding to the local pressure [J/kg]
E	internal energy in the first law of thermodynamics [J]
E_b	hot film anemometer bridge voltage [V]
F_g	mass fraction of vapour derived from the law of partial pressures
g	gravitational constant [m/s^2]
h_g	vapour specific enthalpy corresponding to the local pressure [J/kg]
h_ℓ	liquid specific enthalpy corresponding to the local pressure [J/kg]
h_{st}	liquid depth in the separation tank [m]
k_a	air thermal conductivity [W/m°C]
k_f	liquid thermal conductivity evaluated at the film temperature [W/m°C]
k_g	vapour thermal conductivity [W/m°C]
k_m	vapour/air mixture thermal conductivity [W/m°C]
L	latent heat of condensation corresponding to the local pressure [J/kg]

L_f hot film probe heated length [m]

m_c instantaneous mass condensed [kg]

m_g retained vapour mass [kg]

m_ℓ retained liquid mass [kg]

n exponent in King's law

N number of 1 cm distance increments along the tracking length for a given bubble

Nu bubble overall local external Nusselt number

Nu_p hot film probe Nusselt number

p_d calibration wind tunnel dynamic pressure [Pa]

p_{ex} pressure at the downcomer exit [Pa]

p_{st} pressure in the separation tank [Pa]

p_{vc} pressure in the vacuum chamber [Pa]

Pr liquid Prandtl number

$\dot{q}_\ell$ total heat transported from the vapour into the liquid [W]

Q heat transferred in the first law of thermodynamics [J]

Q_ℓ downcomer inlet liquid flowrate [ℓ/s]

R_3 hot film anemometer bridge series resistance [ohms]

R_c hot film probe cold resistance [ohms]

R_o hot film probe operating resistance [ohms]

R_p hot film probe resistance [ohms]

Re bubble Reynolds number

Re_p hot film probe Reynolds number

t elapsed time referenced to the start of the tracking length for a given bubble [s]

T_e hot film probe calibration ambient temperature [°C]

T'_e hot film probe ambient temperature [°C]

T_f film temperature [°C]

T_g vapour temperature in the separation tank [°C]

T_ℓ downcomer inlet liquid temperature [°C]

T_p hot film probe operating temperature [°C]

T_s saturation temperature corresponding to the local pressure [°C]

u_a calibration wind tunnel air velocity [m/s]

u_{ex} liquid velocity at the downcomer exit [m/s]

u_g bubble nominal absolute velocity [m/s]

u_ℓ inlet liquid velocity [m/s]

u_m vapour/air mixture average velocity [m/s]

u_r bubble nominal relative velocity [m/s]

U_ℓ bubble overall local external heat transfer coefficient [W/m^2 °C]

U'_ℓ volumetric bubble overall local external heat transfer coefficient [W/m^3 °C]

v_g vapour specific volume corresponding to the local pressure [m^3/kg]

v_ℓ liquid specific volume corresponding to the local pressure [m^3/kg]

V_b bubble volume [m^3]

W work done in the first law of thermodynamics [J]

W_f hot film probe heated width [m]

x_m denotes any thermodynamic property of the vapour/air mixture

z position along downcomer length [m]

Greek

ρ_g vapour density [kg/m^3]

ρ_ℓ liquid density [kg/m^3]

ρ_m vapour/air mixture density [kg/m^3]

μ_g vapour dynamic viscosity [kg/m.s]

μ_ℓ liquid dynamic viscosity [kg/m.s]

μ_m vapour/air mixture dynamic viscosity [kg/m.s]

Subscripts

1 initial incremental position

2 final incremental position

i initial value at start of the tracking length

f final value at the end of the tracking length

Superscripts

- overbar denotes position averaged values

ACKNOWLEDGEMENT

The author wishes to express his sincerest gratitude to Dr. E.G. Hauptmann for his considerable insight and constant encouragement throughout the course of this investigation. The technical and administrative staff of the mechanical engineering department are to be acknowledged for their conscientiuous assistance. The author would also like to thank his fellow graduate students for their invaluable discussions and advice.

Special thanks are reserved for my parents for their motivating support and unbounded understanding.

Financial support for this study by the Natural Sciences and Engineering Research Council of Canada is gratefully acknowledged.

CHAPTER I

INTRODUCTION

1.1 Hydraulic Vapour Compression (HVC)

The downward flow of a gas and liquid mixture will result in the compression of the gas phase because of the increasing hydraulic pressure. Figure 1.1 shows a schematic of the compression process achieved in a large diameter pipe or "downcomer". Following the entrainment of the gas into the liquid, the gas phase typically assumes bubble form and the bubbles are gradually reduced in size by hydraulic compression as they are carried downward by the liquid flow. This principle has been utilized in the well known process of hydraulic air compression (HAC), where water is commonly used as the compression fluid. A similar process termed hydraulic vapour compression might employ a single component flow such as water and water vapour. The processes of HVC and HAC differ because compression heating results in the partial condensation of the vapour in HVC, whereas, the air in HAC does not condense. The primary motivation for this investigation is derived from the current lack of knowledge concerning vapour condensation rates in the HVC process.

A proposed application of the HVC process is in a novel open cycle heat pump which will use sea water as the working fluid. The primary benefit of such a heat pump is the possibility of using the oceans of the world as a source of low grade heat (Ryan [1]). A schematic of a single compression stage open cycle heat pump is shown in Figure 1.2. Sea water is pumped into a chamber located at the apex of a siphon loop. The vacuum maintained in the chamber causes partial flashing of the

inflowing liquid resulting in the formation of a vapour cavity above the liquid. The draining of the liquid into a large downcomer located beneath the chamber induces vapour into the downflow thus initiating the HVC process. Separation of the liquid and compressed vapour follows at the bottom of the downcomer with the heated vapour being delivered to a condenser. The heat recovered by the condenser can be used for space heating of commercial and/or residential buildings. The temperature-entropy diagram for the HVC process is also shown in Figure 1.2. Sub-cooled liquid at position 0 is flashed to saturated vapour at position 1. The vapour is compressed from position 1 to 2. Point 2s denotes isentropic compression. The superheated vapour is condensed from position 2 to 3.

The feasibility of the heat pump is dependent on the efficient compression of large quantities of the extremely low density water vapour generated by the flashing of the sea water. Preliminary calculations have shown that the HVC process may be capable of providing a sufficiently high vapour flowrate (in excess of 8 m^3/s) necessary to achieve the economies of scale required for practical application. Judging from the fact that hydraulic air compressors are capable of generating air flowrates in excess of 18 m^3/s (Langborne [2]), similarly sized hydraulic vapour compressors can be expected to produce comparable vapour flowrates.

The HVC process can produce any pressure given a sufficient downcomer length. The amount of compression is necessarily less than the hydrostatic pressure difference across the height of the downcomer completely filled with the compression liquid. This is a result of the reduction in the mean density of the downflow caused by the presence of the vapour. The lowered density dictates that the downcomer height must be greater than the liquid hydrostatic height in order to achieve a

compression ratio equal to that as defined by the liquid hydrostatic height.

Condensation, or overall heat transfer plays an important limiting role in HVC. If the compression occurs extremely slowly, or if the heat transfer rate is sufficiently large, the vapour is simply returned to the liquid state as the evaporation or flashing stage of the process is reversed. If the compression occurs very quickly, or if the heat transfer rates from the vapour to liquid are low, the vapour essentially undergoes adiabatic compression before being delivered to the separation vessel at the bottom of the downcomer. The heat flux from the bubble wall thus plays the dominant role in determining the amount of compressed vapour which the HVC can deliver.

During vapour compression, the driving temperature difference for condensation forms between the vapour and liquid phases because the liquid temperature remains essentially constant. This temperature gradient varies from the center of each bubble out to the surrounding liquid and increases in magnitude along the length of the downcomer. Condensation occurs when the vapour is cooled sufficiently below the saturation temperature corresponding to the local system pressure. For a vapour bubble suspended in a liquid which is slightly below the saturation temperature, condensation will occur at the bubble wall. A hypothetical temperature profile is shown in Figure 1.3 extending from the center of a vapour bubble out to the surrounding liquid. The temperature at the bubble center will likely be a maximum and will be slightly above saturation because of compression heating and imperfect heat transfer. The temperature will decrease from the center to the bubble wall. In a high purity single component system, the wall

temperature is very near the saturation temperature corresponding to the liquid pressure (Isenberg, Moalem, and Sideman [3]). The temperature decreases from the wall to the bulk liquid temperature. The vapour temperature is extremely difficult to accurately measure. It is for this reason that the heat transfer from bubbles is usually calculated based on the temperature difference between the bubble wall and bulk liquid temperatures.

The HVC process occurs in a two-phase bubbly flow regime within the downcomer. The flow pattern is characterized by a suspension of discrete bubbles in a continuous liquid. Within this regime, void fraction (vapour cross-section area fraction) can range from less than 1% to approximately 30% for pure liquids. The existence of contaminants or the addition of chemical foaming agents can allow bubbly flow to persist virtually up to 100% void. The absolute and relative directions of vapour and liquid flow also influence the void fraction. Only vertical co-current downflow is considered here.

The governing forces acting within the bubble flow regime include surface tension, viscosity, inertia, and buoyancy (Wallis [4]). The complex interactions of these forces dictate the velocity and pressure fields of the flow around individual bubbles. In vertical co-current downflow, a slip or relative velocity tends to develop between individual bubbles and the surrounding liquid. Individual bubble size and shape determine the balance of buoyancy to viscous and form drag. This force balance in turn determines the magnitude of the slip velocity. The effect of the slip velocity is to cause convection heat transfer off the bubble surface. Bubble trajectory as well as oscillation also influence convection off the bubble surface.

1.2 Literature Review

Literature specifically dealing with the process of HVC is not yet available. There is, however, information of interest in work related to the subject. The literature reviewed includes previous work in HAC, bubble dynamics, and heat transfer from bubbles.

1.2.1 Hydraulic Air Compression (HAC)

The concept of HVC was evolved directly from the process of HAC. Accordingly, the importance of gaining a basic understanding of HAC cannot be overemphasized. Langborne [2] has managed to trace the history of HAC back to an Italian invention called the "trompe" built in 1588. The operating principle of the HAC is identical to that of the trompe; induced air entrained in a downward flow of water is compressed by the increasing local hydraulic pressure. In the first decade of the 20th century, 13 large HAC plants had been installed in Canada, Germany, United States, Sweden and Peru. Published operating compression efficiencies ranged from 55 to 83% with deliverd air flowrates ranging from 0.13 to 18.87 m^3/s at pressures up to 806.7 kPa.

Rice [5] conducted experimental and numerical work in an attempt to predict HAC performance for varying ratios of air-to-water mass flow-rates. Air was blown rather than induced into a laboratory scale HAC downcomer in order to accomplish this. It was found that for a fixed net applied head, there was a maximum air to water mass flowrate ratio for which operation was possible. A HAC freely inducing air rather than having a throttled source of air will operate at the maximum air-to-water mass flowrate ratio. Compression efficiency was found to increase linearly with the mass flowrate ratio. The maximum compression

efficiency was thus achieved at the maximum possible mass flowrate ratio for a given fixed, net, applied head.

Rice and Chen published three papers [6-8] concerned with the effects of air solubility on compression efficiency during HAC. They found that the amount of air dissolving in the water during compression was diffusion rate controlled. The slowness of the diffusion process effectively prevented the achievement of the equilibrium amount of dissolved air during the downflow period. Accordingly, for identical downcomer geometries, they found that higher mass flowrate compression processes were much less affected by air mass losses through dissolution. For any given total mass flowrate, however, it was concluded that compression efficiency degradation due to air solubility effects was severe.

Vapour condensation during HVC can be considered to be a similar process to air dissolution during HAC. Both events result in finite rate mass transfer to the liquid medium. As forced convection mass is significantly greater in magnitude than diffusive mass transfer it can be expected that vapour condensation will degrade the vapour production of HVC at least as much as air dissolution degrades the air production of HAC.

Berghmans and Ahrens [9], constructed a numerical model to predict HAC performance characteristics as a function of water flowrate and system geometrical parameters. Their model assumed a downcomer entrance void of 0.3 for all calculations. Of particular interest was that system efficiency was found to be a weak function of downcomer cross-sectional area. Once a relatively high flowrate was achieved, system efficiency ceased to increase.

Summarizing, the important HAC parameters appear to include the available head, the air induction scheme, and the total flowrate. These parameters are likely to be important in the HVC process as well as the two processes are very similar.

1.2.2 Bubble Dynamics and Heat Transfer

A comprehensive critical review of the previous work on the fluid dynamics, heat trasnfer, and mass transfer of single bubbles, drops and particles has been compiled by Clift, Grace and Weber [10]. The book has an extremely broad emphasis and is useful as a general reference on single bubble behaviour. Of specific interest is previous work concerned with the dynamics and heat transfer of single vapour bubbles during collapse in one component systems. Research on nucleate boiling has produced a great deal of empirical data on this subject. The bulk of the data obtained, however, does not adequately characterize bubble collapse in HVC because of the extreme pressure and temperature environments under which bubble collapses occurred. A few works conducted under moderate pressure and temperature environments are discussed. Research into desalination has also contributed bubble collapse data though under more comparable conditions to the HVC environment. Both bubble collapse in miscible and immiscible liquids have been studied. Only bubble collapse in miscible liquids are applicable. A number of experimental and theoretical studies are discussed.

1.2.2.1 Experimental

With few exceptions, previous experiments conducted were photographic studies of vapour bubble collapses initiated by the application

of step pressure increases. The methods of step pressure application varied. All methods however, were motivated towards the establishment of an easily controllable subcooled environment. Due to the suddenness of the applied pressure rises, collapse times were extremely short, ranging from milliseconds to hundreds of milliseconds. The pressure difference between initial and final system presures were presented in corresponding degrees of subcooling, defined as the difference between the vapour saturation temperature (at the final system pressure) and the bulk liquid temperature far from the bubble.

One of the pioneering experimental studies was performed by Levenspiel [11]. Liquid side heat transfer coefficients were estimated on the order of 50 kW/m^2 °C from steam bubbles collapsing in water. Bubble shapes were observed to be highly irregular during collapse but bubbles did approach a spherical shape near the end of collapse. On average, bubble volumes decreased 100 fold during collapse periods approximately 100 ms long. Mean bubble diameters ranged from 3 to 9 mm. Final system pressure was atmospheric with subcoolings ranging from 0.6 to 11 °C.

Bankoff and Mason [12] estimated the turbulent heat transfer from steam bubbles collapsing in a water jet. Bubble Nusselt numbers were correlated with bubble Peclet and Strouhal numbers. The extremely high rates of collapse necessitated that Peclet numbers be based on bubble wall velocities since these were of the same order of magnitude as the liquid jet velocities. The bubble Strouhal numbers were defined as the ratio of bubble wall velocities to liquid jet velocities. This was an attempt to account for observed bubble shape pulsations. Nusselt numbers ranging from 398 to 1485, are considered to be large owing to

the highly turbulent conditions. The flow field surrounding each bubble in the HVC process is much less turbulent than that generated in Bankoff and Mason's study.

Florschuetz and Chao [13] studied the mechanics of vapour bubble collapse under free fall conditions in order to maintain bubble sphericity. It was shown that the collapse mode could be controlled by liquid inertia or heat transfer or both, depending on system conditions. During heat transfer controlled collapse, it was noted that vapour pressure is nearly equal to system pressure due to the relatively slow rate of collapse as compared to liquid inertia controlled collapse. The possible effects of bubble translation on collapse rates were acknowledged but not studied. Wittke and Chao [14,15] later found that bubble translation significantly increased collapse rates for heat transfer controlled collapse. Further experimental work by Hewitt and Parker [16], Board and Klimpton [17], and Delmas and Angelino [18] supported their findings.

The previous experimental works reviewed so far have been performed at or slightly below atmospheric pressure. Brucker and Sparrow [19] have studied steam bubble condensation in water at pressures ranging from 10.3 to 62.1 bar with subcoolings ranging from 15 to 100 °C. Calculated heat transfer coefficients were on the order of 10 kW/m^2 °C with Peclet numbers of the freely rising bubbles ranging from 2000 to 3000. In general, heat transfer coefficients were found to increase with pressure though there was no clear trend with subcooling. An interesting observation was made that average Nusselt numbers obtained were within 50% of those for a solid sphere having a diameter equal to the initial bubble diameter and a velocity equal to that of the bubble.

The presence of noncondensable gases within vapour bubbles have been observed by Florschuetz and Chao [13], Wittke and Chao [15], and Brucker and Sparrow [19]. The estimation of the amounts of gas present have been based on the remaining volumes of bubbles which did not collapse completely. It is apparent that the presence of noncondensables retards heat transfer. A plausible postulate forwarded is that gas molecules tend to pile up at the interface as bubble collapse proceeds. This accummulation is not necessarily uniform, however, it does form a screen against vapour condensation.

Moalem, Sideman, Orell and Hetsroni [20] have experimentally examined the effects of bubble interaction on collapse rates in freely rising bubble trains in one and two component systems. The extent of bubble interaction was controlled by the variation of bubble generation frequency. At low generation freuqencies, bubble collapse rates were observed to decrease in comparison to the collapse rates of freely rising single bubbles. It was postulated that preceding bubbles increased the temperature of the liquid such that the temperature driving force was reduced for the following bubbles. At higher generation frequencies, following bubbles were observed to enter the wake region of preceding bubbles. The increased convection counteracted the effects of the reduced temperature driving force, thus resulting in collapse rates approaching that of single bubbles.

Sekoguchi, Fukui, and Sata [21] statistically studied the void fraction distribution in vertical bubble flow. For bubbly downward co-current flow, it was observed that vapour flow was concentrated near the pipe center. Bubble paths away from the pipe wall were observed to be spiral in pattern.

1.2.2.2 Theoretical

Ruckenstein [22] analyzed the effect of bubble translation on bubble growth by assuming it was a quasi-steady process and the liquid flow around the bubble could be modelled by potential flow. The basis of these two assumptions was that the bubble wall velocity was small in comparison to the bubble velocity and that the thermal boundary layer was small in comparison to the bubble radius. Isenberg et al. [3], Moalem and Sideman [23], and Dimic [24], adhering to the assumptions forwarded by Ruckenstein, obtained simple analytical solutions for bubble collapse times with and without the presence of noncondensables. Wittke and Chao [15], and Prisnyakov [25] began with a more general approach but were unable to significantly improve predictions of collapse times over that of the simpler solutions. Collapse times were presented in dimensionless form parameterized by Peclet number, Jacob number, and initial bubble radius. The collapse times predicted by these models does not adequately describe the bubble collapse rates in the HVC process.

In addition to their experimental work, Moalem, Sideman, Orell, and Hetsroni [20,26] have theoretically modelled the condensation of vapour bubble trains in stagnant liquid. Their results show that bubble collapse times increased with increased bubble frequency and increased number of bubbles per unit flow cross-sectional area. Sideman and Moalem [27] proceeded one step further and studied the condensation of vapour bubble trains under counter and co-current flow. Their findings were as expected, condensation rates were lower in co-current flow in comparison to counter-current flow. In both cases, increased bubble density decreased the condensation rate. At low superficial vapour velocities ranging from 0.0063 to 0.065 m/s, the calculated volumetric heat transfer coefficients ranged from 12 to 232 kW/m^3 °C.

1.3 Scope of the Present Investigation

The review of previous work in the areas of HAC, and single bubble dynamics and associated heat transfer has been performed to provide sufficient background information for the present investigation The constant pressure environments for bubble collapse under which all previous work has been conducted may not adequately model the bubble condensation or collapse environment in the HVC process. Bubbles in a hydraulic vapour compressor are subjected to an increasing hydraulic pressure during collapse as they travel along the downcomer. As a consequence, the rate of collapse may significantly deviate from the rates measured in previous studies. The lack of experimental data of collapse rates under a pressure gradient, as required for the design of a hydraulic vapour compressor, thus motivated a preliminary experimental study of the phenomenon.

The primary objective of this study was to obtain estimates of the vapour condensation rates present during the compression process. Appropriate generalizations of these estimates can provide the designer with quantitative information concerning the possible vapour mass losses through the HVC process for given sets of operating conditions. To this end, vapour condensation rates were estimated from photographic histories of bubble size decrease in an experimental apparatus modelling a hydraulic vapour compressor. To quantify the heat transferred through condensation, bubble Nusselt numbers were correlated with the operating parameters described by the Peclet number and the dimensionless downcomer length. Vapour mass flowrates were also measured to determine a range of possible compressor outputs.

CHAPTER II

EXPERIMENTAL APPARATUS

2.1 General Concept

The essential purpose of the experimental apparatus used in this investigation was to allow for the photographic study of vapour bubble condensation during travel along the downcomer. The apparatus used was built previously for another experiment. Modifications were made where necessary, however, the basic circulation loop was kept intact. A description of the apparatus follows with detailed information being referenced to Ryan [28].

Photographs of the apparatus and instrumentation are presented in Figures 2.1 and 2.2. A schematic of the flow circuit and associated instrumentation is shown in Figure 2.3. The flow circuit was comprised of two separate flow paths, a main circulation loop and a siphon loop. The flow in the main circulation loop was entirely liquid. The flow was pumped from the separation tank, continued through a coaxial counterflow heat exchanger, and discharged into the overflow vessel. The main circulation loop had two primary functions; the first was to maintain a constant level in the overflow vessel, the second was to provide a degree of control over the liquid temperature. Building supply water was used as the cooling medium in the heat exchanger.

The upward leg of the siphon loop drew an entirely liquid flow from the overflow vessel. The flow proceeded through a flowmeter and partially filled the vacuum chamber. The downward leg of the siphon was in effect the test section. The entrance of the test section was located inside the vacuum chamber. Two-phase flow, formed in the

entrance of the test section, was drained into the separation tank. Bubbles in the two-phase flow were photographically tracked along the test section.

The placement of the vacuum chamber and downcomer test section in the siphon loop was chosen based on several factors. The primary concern was of course to accurately model the actual HVC process. Other factors were:

(a) Relatively easy attainment and maintenance of near saturation conditions in the vacuum chamber. This was achieved by the placement of the vacuum chamber at the apex of the siphon loop, the point of lowest pressure in the system.

(b) Efficient removal of noncondensable air in the vacuum chamber. This was achieved by the continual evacuation of small amounts of vapour from the top of the vacuum chamber which resulted in the generation of additional vapour. This process minimized the possibility of air entrainment into the flow entering the downcomer test section.

(c) Elimination of pressure pulses due to pumping since the vacuum for the siphon was pulled through a large accumulator tank instead of being pulled directly by the vacuum pump. This allowed smooth steady flow of liquid through the siphon up-leg and into the downcomer.

The inducement of vapour into the flow at the top of the downcomer test section proved to be a difficult problem. Ideally, single bubbles were to be introduced into the flow in order to minimize the effects of bubble interaction. Many unsuccessful attempts were made using a

variety of induction tube geometries. Eventually vapour generation and entrainment was achieved via the breakup of supercavitation jets formed at the base of a square ended, solid, cylindrical rod placed at the downcomer entrance. Figure 2.4 contains a photograph of a typical supercavitation jet at the entrance of the test section.

Supercavitation jets are a type of 'fixed' cavity as described by Knapp, Daily, and Hammitt [29]. The formation of the supercaviation jets was due to the static pressure drop created by the rapid acceleration of saturated liquid flowing by the end of the rod. The shapes of the jets varied depending on liquid flowrate and degree of subcooling. For high subcoolings and high flowrates, the jets produced were small and bullet shaped, usually 1 to 1.5 rod diameters in diameter and 1 to 3 rod diameters in length. Lower subcoolings and lower flowrates produced jets that were umbrella shaped, 2 to 3 rod diameters in diameter and 3 to 5 rod diameters in length. The breakup of these jets occurred at their bases where bubbles were observed to be torn off from the jets by the turbulent liquid flow. An obvious and important advantage of this method of bubble generation was the virtual certainty that air bubbles would not be present in the downflow. The disadvantage lies in the controllability of the number and size of vapour bubbles generated. Every attempt was made to keep the cavitation jets as small as possible to limit the number of bubbles generated. The sizes of bubbles could only be controlled to a minor extent. In general, larger and fewer bubbles were generated at lower subcoolings and flowrates.

2.2 Working Fluid

The reasons for the use of Freon-11 in the present investigation are given in [28, p.15]. The most important reason for using Freon-11 was that it had a low boiling point, 23.8°C at atmospheric pressure. Mayinger [30] has noted that in general, Freon is a suitable modelling fluid for scaling steam-water mixtures. This observation was based on a literature survey and his own scaling experiments. Freon-11 has a boiling point of 23.8 °C at atmospheric pressure. Typical working temperatures ranged from 10 to 15 °C at pressures ranging from 75 to 104 kPa.

2.3 Piping, Tubing, Hose, and Fittings

The sizes and materials of the piping, tubing, hose, and fittings are given in [28, p.17]. A number of PVC valves and associated fittings were replaced with identical components due to breakage apparently caused by Freon embrittlement. Freon embrittlement caused minute cracks to appear in the PVC material. All o-ring seals were replaced as a precautionary measure.

2.4 Vacuum Chamber, Separation Tank, Overflow Vessel, and Vacuum Accummulator Tank

The vacuum chamber configuration (Figure 2.5) was slightly modified from the description presented in [28, p.18]. A new Nalgene bell jar replaced the old cracked jar along with a new o-ring seal. The false floor was removed as was the chamber inlet wire basket. The support stand for the cavitation rod was screwed and bolted into the aluminum floor for stability.

The separation tank (Figure 2.6) was constructed out of a 15.24 cm high section of 50.8 cm I.D. PVC pipe sealed at either end by aluminum

plates. Three tube sections were welded into the top plate connecting to the circulation pump intake, the overflow vessel outlet, and the downcomer outlet. A 1.27 cm I.D., 20.4 cm long section of tube screwed into the top plate was used as a vapour exhaust. A regulating valve was attached to the end of the exhaust to meter the vapour outflow. An additional toggle operated shut-off valve was installed as an emergency pressure release. The overflow vessel and vacuum accumulator tank were not modified.

2.5 Circulation and Vacuum Pumps

Pump details are given in [28, p.20]. The circulation pump impeller was overhauled before the start of experimentation, however, the pump continued to sieze occasionally. Prolonged use of the circulation pump often resulted in the motor overheating. A 30 cm diameter axial flow fan was installed to cool the pump motor. The vacuum pump ran without problems.

2.6 Downcomer Inlet Orifice and Cavitation Rod

A sketch of the downcomer entrance orifice used is shown in Figure 2.7. The purpose of the venturi-type design was to smoothly accelerate the flow into the downcomer to attain velocities high enough to generate cavitation jets at the base of the inserted rod.

A number of rod sizes and base geometries were tested. It became apparent that rod size rather than rod base geometry influenced the formation of the caviation jets. A square-ended rod with a diameter of 6.35 mm was eventually chosen as it provided small and fairly stable cavitation jets.

2.7 Downcomer Test Section

In order to minimize the distortion of photographing a travelling bubble, the downcomer test section would ideally be square in cross-section. Square-section glass tubing in the desired length was not available. The alternative solution was to use a conventional round-section glass with a constructed aluminum-glass composite square-section tube sleeved over top. The inner round-section tube (actual test section) was 2.54 cm I.D. During the photographic tracking of vapour bubbles, the outer square-section tube was filled with Freon. Since the inner round-section tube contained Freon as well, based on Snell's law of refraction, the distortion caused by the curvature of the inner tube was effectively minimized.

2.8 Instrumentation

The instrumentation used in this investigation recorded the steady state values of the parameters of interest. Small fluctuations were either averaged over time or median values were taken.

2.8.1 Temperature Measurement

The liquid temperature in the vacuum chamber and the separation tank were obtained with two Omega type PR-11 platinum resistance thermometer probes (RTD) coupled with an Omega model 199P2 digital indicator through an Omega 6 position selector switch. The digital indicator produced analog output signals to 0.1 °C resolution for the data acquisition system. Vapour temperature in the separation tank was measured with a copper-constantan Y8103 type K bead thermocouple probe connected to a Fluke digital multimeter model 8024A. Temperature was displayed

directly to a resolution of 1 °C. Vapour temperatures ranged from 11 to 15 °C. All probes were calibrated at 0 °C and 100 °C. Fluctuations were averaged over time.

2.8.2 Pressure Measurement

Stagnation pressures were measured in both the vacuum chamber and the separation tank. Simple U-tube water manometers were used to measure pressures relative to atmospheric since only steady state pressure readings were required. Maximum and minimum values were averaged when fluctuations occurred. Ambient pressures were measured with a Mercury manometer. The vacuum chamber pressure ranged from approximately 75 to 81 kPa. Typical separation tank pressures ranged from atmospheric to 104 kPa.

2.8.3 Depth Measurement

Liquid depth measurements were manually recorded for both the vacuum chamber and separation tank using a graduated steel ruler for reference. Maximum and minimum values were averaged when fluctuations occurred. Operating liquid depth in the vacuum chamber ranged from 123 to 166 mm. Liquid depth in the separation tank rnaged from 49 to 88 mm.

2.8.4 Liquid FLowrate Measurement

Liquid volumetric flowrate in the siphon loop was determined with a paddlewheel type measurement device described in [28, p.22]. No attempt was made to measure the flowrate in the downcomer test section as the presence of bubbles in the flow would have made measurements highly unstable regardless of the measurement technique. Alternatively, the flowrate in the downcomer test section was inferred as follows. Assum-

ing that only small amounts of vapour were evacuated from the vacuum chamber, by holding the liquid level constant in the vacuum chamber, the volumetric flowrate passing through the downcomer can be considered to be equal to the volumetric flowrate measured by the paddlewheel device in the siphone up-leg. The total mass flowrate through the downcomer test section was obtained by multiplying the volumetric flowrate by the liquid density corresponding to the vacuum chamber liquid temperature. Fluctuations in the paddlewheel device output were averaged over time. Typical flowrates ranged from 0.36 to 0.57 ℓ/s.

2.8.5 Data Acquisition System

A Neff model 620 data acquisition system was employed to sample the analog signals generated by the two RTD probes and the paddlewheel flowrate measurement device. The program written for data acquisition allowed direct user input of all manually measured parameters as well as ambient pressure and temperature, and current apparatus geometry. A flowchart of the program is presented in Figure 2.8. The Neff proved to be unreliable, often breaking down completely. The data for run 8 was taken entirely without the aid of the data acquisition system.

2.8.6 Hot Film Anemometry

A Thermosystem Inc. (TSI) model 1235W hot film wedge probe was used to measure the velocities of the vapour/air mixture existing in the separation tank. The velocities obtained were used to measure the vapour mass produced in the test section. The hot film wedge probe was powered through a TSI model 1010A constant temperature anemometer. The anemometer output voltage was viewed and stored on a Nicolet model 3091

digital oscilloscope. The stored output was then transmitted onto floppy disc via an IBM PC. As a final step, the contents of the floppy discs were transferred to the VAX 11/750 for processing.

For all measurements, the hot film probe was positioned in the center of the vapour exhaust tube as shown in Figure 2.9. To ensure that the vapour flow was fully developed before measurement, the probe was inserted at the end of the exhaust tube which was over 40 tube diameters in length. The choice of using a hot film wedge probe over that of a hot wire probe was based on availability and ease of use. Only steady flow measurements were desired, therefore the frequency response capability of a hot wire was not required.

The hot film probe calibration was carried out in a wind tunnel for air speeds ranging from 1.14 to 14.9 m/s. The sensitivity of the alcohol manometer used limited the minimum measureable air velocity in the wind tunnel. The probe operating temperature was set at 64.1 °C corresponding to an overheat ratio of 1.15. The maximum probe operating temperature, as recommended by the manufacturer, was 66.7 °C.

Since the actual measurements were to be performed in a different medium (vapour/air mixture) than that of the calibration medium (air), it was necessary to use dynamic similarity to obtain the corrected velocities in the measurement medium. To this end, probe calibration Nusselt numbers were determined as a function of the calibration Reynolds numbers. Further, since the temperature differences between the measurement and calibration mediums were significant in comparison to the probe operating temperature, measurement bridge voltages were scaled using temperature correction factors based on the difference betwen the calibration and measurement fluid temperatures. The scaled

measurement voltages were used to calculate the vapour/air mixture Nusselt numbers based on fluid conductivities estimated from the ratios of the partial pressures of the vapour to air. From the calibration curve of air Nusselt versus air Reynolds numbers, the measurement Reynolds numbers were obtained. The exhaust velocities of the vapour/air mixture were then determined from the Reynolds numbers based on fluid kinematic viscocities also estimated from the ratios of vapour/air partial pressures. Details of the probe geometry, the anemometer used, and the calibration procedure are contained in Appendix A.

2.9 Photographic Equipment

The high speed photographic tracking of vapour bubbles was accomplished using the arrangement sketched in Figure 2.10. The camera was manually pivoted on the tripod in order to track individual bubbles travelling down the test section. The maximum tilt or included angle of travel necessary to view the entire legnth of the downcomer was 27.2 degrees. The maximum size distortion occurred at 13.6 degrees above or below the horizontal and can be estimated from the cosine of the angle. At 13.6 degrees this is approximately 2.8%. In view of the possible magnitudes of other inherent experimental errors, this error is acceptable.

The camera used was a Red Lake Hycam rotating-prism type 16 mm high-speed motion-picture camera. The framing speed of the camera was calibrated against the driving AC voltage. It was operated at a constant voltage setting to maintain a steady framing speed, however, it was observed that film speed through the camera varied considerably and a steady framing speed was not achieved after the initial acceleration.

This resulted in minor exposure variations within a single roll of film, but the variations were consistent from film to film. The framing rates used ranged from 600 to 1400 frames per second at a nominal applied voltage of 50 VAC. The camera was equipped with a Neon timing light which was driven at frequencies of 100 and 1000 Hz by a Red Lake model TLG-3 Millimite timing light generator. The marks produced by the timing light were used to estimate the instantaneous velocity of individual bubbles. Frequency calibration of the timing light generator showed less than a 0.5% deviation at both 100 and 1000 Hz.

The lens used was a Tamron 200-500 mm F/6.9 ultra-telezoom. All photography was performed at 500 mm F/6.9 resulting in a depth of field of approximately 3 cm. Extreme care was exercised when focussing but the inherent play in the tripod pivoting mechanism often shifted the focus of the lens and consequently a number of exposed films were discarded due to poor focus.

The pin-pointing of individual bubbles necessitated the use of a Spectra-Physics model 155 optic laser. This was because through-the-lens visual tracking was made impossible by film blockage of the camera eyepiece, a characteristic of rotating-prism type cameras. The laser was mounted on the same tripod platform as the camera and thus moved in synchronization with the camera allowing fairly precise location of the field of view of the lens.

To obtain the highest detailing of bubble shape and size, a back-lighting technique was used to silhouette the bubbles tracked. Two 1000 W quartz-Bromine studio lamps were placed behind the downcomer test section facing the camera. The light was dispersed through sheets of vellum placed over the glass of the refraction tube. In consideration

of the extreme heat put off by the two lights, they were only switched on during actual filming; these periods extended no longer than two minutes.

100 foot rolls of Kodak 4-X negative black and white film were used. Under the described lighting conditions, the effective ASA of the film was 400. The film is commonly used for industrial photography and has good depth of field qualities at low levels of illumination.

CHAPTER III

EXPERIMENTAL PROCEDURE

3.1 Initial Equipment Testing

The initial testing of equipment involved two stages. The first stage was simply to fill the circulation loop, the siphon loop, and the heat exchanger with water in order to check for leaks. All leaks found were stopped and the circuits refilled. During water batching, the paddlewheel flow measuring device, the two water manometers, the two temperature probes, and the data acquisition system were verified for proper operation. As the basic circuit of the apparatus had been unused for over two years, the water was allowed to freely circulate for a number of hours in attempt to flush out any residual debris in the pipes.

The second stage of initial testing involved the introduction of Freon to the circulation and siphon loops. Before the addition of the Freon, both loops were dismantled and blown free of any water with compressed air. The circulation pump was disassembled, dried and checked for roughness on the impeller body. The apparatus was reassembled and Freon was tested first in the circulation loop and then in the siphon loop. It was observed that considerably more vacuum had to be generated in the vacuum chamber with the Freon in comparison to the water. The Freon was apparently vapourizing in the chamber thus a higher vacuum was necessary to establish the flow in the siphon loop. The circulation pump was found to cavitate badly if either the Freon level in the separation tank was too low or the Freon temperature was too close to saturation. Particular care had to be taken to maintain a high liquid

level (> 15 cm) in the tank when the Freon temperature was over 16 °C. During the initial Freon testing, it was discovered that a large amount of Freon would gradually be lost through evaporation over a few hours. Additional Freon was invariably required to maintain a constant level in the separation tank.

Following the initial Freon tests, a number of days were spent in familiarization with the system reactions to pressure, temperature and flowrate changes. Maximum and minimum attainable values for each parameter were noted. Various bubble generation schemes were attempted until success came with the supercavitation jets.

The initial testing of the photographic equipment involved equipment arrangement and operation to obtain the correct exposure setting. The camera tilting mechanism on the tripod consisted of a manually cranked worm gear driving a curved rack gear. The mechanism was carefully shimmed and well greased for smooth operation but the inherent backlash in the gearing could not be removed. The camera was positioned level with the horizontal center of the test section at a distance of 3.5 m. Care was taken to ensure the lens was perpendicular to the face of the refraction tube. The optic laser was then mounted beside the camera. Viewed through the camera lens, the laser beam was aligned with the horizontal cross-hair of the lens. Vertical alignment was set such that the vertical cross-hair was lying on the test section centerline and the laser beam was pin-pointed on the right frame edge of the refraction tube. This was to ensure that the laser did not reflect into the downcomer.

The focussing of the camera involved both lens and camera eyepiece focussing. The camera eyepiece was focussed by sliding the eyepiece

along its sleeve, focussing on a line scratched on a frame of a dummy roll of film loaded in the camera. The film was then taken out, allowing the lens to be focussed. Obtaining a correct exposure setting proved to be a task complicated by the combination of an unreliable light meter and the speed variation in camera framing rate. Once the correct exposure setting was found, all films were shot at that setting.

3.2 Routine Apparatus Start-Up and Shut-Down

Routine apparatus start-up and shut-down procedures were adhered to in order to maintain proper equipment function and cleaniness. Prior to any actual experimental runs, all instrumentation was switched on and allowed to warm up. The separation tank, overflow vessel and vacuum chamber were cleaned and wiped down with rags soaked in Freon to remove contaminants. Compressed air was blown through the piping to remove collected dust. Preparation of the vacuum chamber involved the centering of the cavitation rod in the downcomer orifice and the filling of the refraction tube with Freon since the filler hole was located in the floor of the vacuum chamber. The chamber was subsequently closed by gently forcing the Nalgene bell jar over the o-ring seal around the base of the chamber. The vacuum pump was started, evacuating the accumulator tank in preparation for the priming of the siphon loop. The water for the heat exchanger was turned on.

Freon was manually poured into the overflow vessel through a plastic funnel to fill the circulation loop. Once the separation tank was half-filled, the circulation pump was switched on. This was to give the circulation pump a sufficient starting inlet head. Further addition of Freon was continued until the separation tank was two-thirds filled.

The vacuum chamber was then evacuated through the accumulator tank to prime the siphon loop. It was extremely important that the evacuation of the vacuum chamber was carried out gradually or otherwise violently unstable flow would result at the entrance to the downcomer.

The final step in the experimental preparation was to establish a cavitation jet. The following procedure was necessary:

1) Apply enough vacuum so that the liquid level in the vacuum chamber was at least 15 cm above the downcomer orifice.
2) Quickly close the vacuum regulation valve and allow the liquid level to drop. This action initiated the cavitation jet.
3) Slowly adjust the vacuum regulation valve to obtain a stable liquid flowrate. The stability of the cavitation jet was dependent on the stability of the flow.

Following an experimental run a strict shut-down procedure was practiced. The pressure in the vacuum chamber was gradually increased, allowing Freon to drain from the siphon loop. The circulation pump was kept running to prevent the Freon in the overflow vessel from entirely draining into the separation tank, which would cause an overflow. Freon was drained slowly from the separation tank through qualitative medium porosity filter paper. This appeared to remove most of the contaminants the Freon would pick up during the experiment. The filtering process would often take over two hours and to minimize evaporation, the Freon was kept as cold as possible by continued circulation of the remaining Freon through the heat exchanger. The overflow vessel and circulation pump had to be disassembled to be completely drained. Used Freon was always stored separately from new Freon. New Freon was easily

distinguishable from used Freon as exposure to air would cause the Freon to become progressively more yellow in colour. The last step was to disassemble the vacuum chamber to relieve the stress on the Nalgene bell jar.

3.3 Bubble Photographic Studies

The two parameters that were independently varied during the bubble photographic studies were the liquid flow rate into the vacuum chamber (0.36 to 0.51 ℓ/s), and the liquid temperature in the vacuum chamber (10.9 to 13.3 °C). Both the liquid flowrate and temperature were limited by the building supply water temperature and the available vacuum. After the initial preparation described previously, the experimental procedure was as follows:

1) The heat exchanger cooling water flowrate was adjusted until the desired Freon temperature was achieved.
2) The vacuum chamber pressure was adjusted to give the desired flowrate and to stabilize the cavitation jet.
3) The pressures and liquid levels in both the vacuum chamber and separation tank were recorded along with the vapour temperature in the separation tank.
4) The data acquisition system was enabled, recording the liquid flowrate, the vacuum chamber liquid temperature, and the separation tank liquid temperature.
5) The lighting was switched on along with the timing light generator and laser.
6) The camera was then switched on.

After the completion of step 2), the apparatus was allowed to run for a minimum of 10 minutes to achieve conditions approaching steady state. Steps 3) through 5) were usually completed in less than two minutes. During runs at higher flowrates, large fluctuations in liquid level and pressure were observed in the separation tank. This was attributable to the high turbulence level in the tank caused by the rapid entrance of liquid and vapour into the tank.

For a single roll of film, the maximum possible number of filming passes along the length of the test section was limited by the velocity of the individual bubbles tracked. At the framing rate used, the 100 ft. roll would last approximately 6 s. Allowing for the time to re-pivot the camera back to the top of the test section, two filming passes could be completed if the tracking velocity was greater than 1 m/s. This was achieved only at the highest liquid flowrate of 0.51 ℓ/s. The tracking strategy involved the selection of the smallest bubble that could easily be tracked. Each of these bubbles would be filmed until they were visually lost among other bubbles. When this occurred, another bubble would immediately be selected and filmed for the remaining test section length.

3.4 Vapour Exhaust Velocity Measurements

The vapour exhaust velocity measurements were conducted using the same procedure as the bubble photographic study. Hot film anemometry was substituted for the photography procedure. The liquid flowrates were varied from 0.42 to 0.57 ℓ/s while liquid temperatures were varied from 9.4 to 14.8 °C. For each vapour velocity measurement, the probe was switched on for a minimum of 5 minutes before the actual measurement. The measurement period extended for 4 s at an oscilloscope sweep rate of 1 sample/ms.

CHAPTER IV

DATA ANALYSIS

4.1 Film Analysis

The analyses of the films taken in the bubble photographic study were performed on a sequenced individual frame basis. Each film was projected onto a wall and viewed repeatedly to select bubbles that were continuously tracked for minimum of 20 cm along the test section. Figure 4.1 contains part of a typical tracking sequence. The quantities obtained from these sequences included bubble instantaneous projected area, instantaneous velocity, and total tracking time. Descriptions of the methods used to obtain these quantities follow.

4.1.1 Determination of the Instantaneous Bubble Surface Area and Volume

The inference of a three-dimensional shape from a two-dimensional projection can be accomplished by revolving the projection about an axis of symmetry. The inference of surface areas and volumes from the projected areas of the bubbles filmed, however, was complicated by the absence of a continuous axis of symmetry. A numerically implemented method of revolving sections of a projected area about their respective axes of symmetry was used to infer both an approximate surface area and volume for individual bubbles.

For an individual frame taken from a selected sequence, the projected area of a bubble of interest was traced onto graph paper. As the magnification factor was relatively high (17.5), it was often difficult to distinguish the exact outline of the bubble silhouette. The author was forced to rely on personal judgement in an attempt to accurately

trace the actual outline. For a poorly focussed silhouette, judgement error could conceivably be as high as 10%. Once a bubble trace was obtained, the outline was digitized and the numerical coordinates transferred to the VAX 11/750. The number of digitized points for a given bubble trace varied from 40 to 120 depending on the number of severity of inflections contained in the trace.

Before the surface area and volume for a given bubble trace was calculated, the principle centroidal axis of the projected area was determined from the digitized coordinates. A coordinate transformation of all data points to the principle centroidal axis was then performed. The purpose of the coordinate transformation was to provide a reference axis that best approximated the probable axis of rotation of the bubble. The new reference axis was taken to be the principle centroidal axis nearest to the original vertical axis.

Following the transformation, the trace was divided into a top and bottom half with each respective half being curve fitted with either a second, third, or fourth degree polynomial. The degree of polynomial fit used was dependent on the number of inflection points present in that half of the trace. Each half was further divided into a minimum of 50 trapezoidal sections and a minimum of 1 spherical cap section as shown in Figure 4.2. The top half was considered first. For each of the trapezoidal sections, an axis of revolution parallel to the vertical principle centroidal axis was defined such that it bisected the base of the section. The cross-section areas generated by revolution about these axes would have the highest likelihood of matching the actual bubble cross-section in the same plane of revolution. This would minimize the error introduced by the method of volume generation through

revolution of the projected area. The typical volume of revolution generated can best be described as a frustum of a skewed cone. Both the volume and side surface area of each frustum was calculated through double numerical integration because of the unusual shape involved. The volume and upper surface area of the spherical cap sections were also calculated. The bottom half of the trace was analyzed identically. The total volume and surface area for the given bubble trace were obtained by the summation of the values calculated for each section.

4.1.2 Determination of the Bubble Trace Interval

The rate of decrease of bubble size provided the basis for estimating the heat transfer from the vapour to the surrounding liquid. To quantify this rate, bubble traces were initially taken every ten frames for each selected sequence. Plots of calculated bubble surface area and volume as a function of time are shown in Figures 4.3 to 4.16. Each data point represents either the surface area or volume obtained from a single trace. The time interval between points was determined by dividing the total tracking time by the number of frames from which bubble traces were taken. The high degree of fluctuation in the data was a consequence of either non-symmetry or bubble shape oscillation. A number of the plots in Figures 4.3 to 4.16 show fairly regular shape oscillations. Ideally, bubble traces should be taken at a frequency equal to a dominant shape oscillation frequency. The bubble would then present approximately the same "face" or projection of itself to the viewer each time a trace would be taken. This would minimize the degree of fluctuation in the bubble surface area and volume data when plotted versus time. In pursuit of this, Fourier frequency analyses of first

order trend removed bubble volume data were done. These analyses, however, did not produce any consistently dominant regular shape oscillation frequencies. The influence of local flow conditions dictated by the average flowrate and the presence of other bubbles caused enough scatter of bubble shape oscillation frequencies that accurate predictions for each bubble was not possible. No attempt was made to take bubble traces at a smaller frame interval.

4.1.3 Determination of Bubble Total Tracking Time and Velocity

The total tracking time for each bubble was obtained by counting the number of timing marks between the initial and final frames of the sequence of interest. Bubble positions were obtained using the 1 cm increment reference scale drawn on the refraction tube. The bubble average velocity was calculated by dividing the total tracked distance by the total tracking time. Bubble "instantaneous" velocity was estimated from the elapsed time taken to travel vertically down 1 cm along the test section. This is in contrast to the actual velocity which would likely be higher since bubbles often travelled downward in a spiral fashion.

4.2 Calculation of the Bubble External Nusselt Number

The calculation of the fluid properties necessary for the estimation of bubble external Nusselt number required a number of assumptions to be made due to the lack of experimental data. The assumptions were:

1) The static pressure at the cavitation jet was equal to the saturation pressure corresponding to the liquid temperature measured in the vacuum chamber. The true pressure at the cavitation jet was

probably lower than the saturation pressure but the difference would not be substantial.

2) The pressure at the exit of the downcomer was calculated from a Bernoulli analysis

$$p_{ex} = p_{st} - \rho_{\ell}\, g\, h_{st} - K_{ex}\,(0.5\,\rho_{\ell}\, u_{ex}^2) \qquad (4.1)$$

3) The pressure gradient from the point of bubble formation to the downcomer exit was linear. This assumption is fairly accurate since the flowrates were low enough such that frictional losses were negligible in comparison to the hydrostatic pressure rise.

4) The bubble wall temperature was equal to the saturation temperature corresponding to the local pressure. This was previously discussed in Section 1.1.

The Nusselt number was used to characterize the heat transfer between the vapour and liquid phases. The heat transferred through condensation was estimated from the first law of thermodynamics. The complete derivation of the equations approximating the heat transferred is contained in Appendix B. The main result, which is valid at any position along the downcomer length, was given by

$$\frac{dQ}{dt} = \left[((\rho_{g2}-\rho_{g1})V_{b1} + \rho_{g2}(V_{b2} - V_{b1}))L_2 + m_{g1}(h_{g2} - h_{g1}) + m_{\ell 1}(h_{\ell 2} - h_{\ell 1})\right]/(t_2 - t_1) \qquad (4.2)$$

The mass condensed and can be rewritten as

$$m_c = (\rho_{g2} - \rho_{g1})V_{b1} + \rho_{g2}(V_{b2} - V_{b1}) \tag{4.3}$$

The second and third terms in Equation (4.2) are much smaller than the first term and can be neglected. The heat transferred from the bubble can now be approximated by

$$\frac{dQ}{dt} = m_c L_2/(t_2 - t_1) \tag{4.4}$$

The total heat transferred into the liquid can be described by

$$\dot{q}_\ell = U_\ell A_{b1}(T_s - T_\ell) \ . \tag{4.5}$$

Equating Equations (4.4) and (4.5) gives

$$m_c L_2/(t_2 - t_1) = U_\ell A_{b1}(T_s - T_\ell) \ . \tag{4.6}$$

Equation (4.8) was solved for the liquid side overall heat transfer coefficient

$$U_\ell = m_c L_2/[(t_2 - t_1)A_{b1}(T_s - T_\ell)] \ . \tag{4.7}$$

In dimensionless form, U_ℓ can be redefined as a bubble external Nusselt number

$$Nu = U_{\ell} D_{se} / k_f . \tag{4.8}$$

The characteristic length used in the Nusselt number was a spherical equivalent diameter defined as

$$D_{se} = 6\ V_b / A_b . \tag{4.9}$$

This followed normal practice in literature. It may have been more appropriate, however, to use a characteristic length based on a ellipsoid rather than a sphere since the typical bubble shape was ellipsoidal. This would have added unnecessary complexity to the Nusselt number definition since ellipsoids have a minimum of two characteristic lengths.

The local or instantaneous external Nusselt number was calculated for each bubble at one centimeter increments along their respective tracked lengths along the test section. The position averaged external Nusselt number was calculated using

$$\overline{Nu} = (1/N) \sum_{j=1}^{N} Nu , \tag{4.10}$$

where N is the number of one centimeter increments along the tracking distance.

An alternative volumetric overall heat transfer coefficient was calculated for comparison purposes as Sideman and Moalem [27] have presented their results using a volume based overall heat transfer coefficient. The definition of the volumetric overall heat transfer coefficient was

$$U'_{\ell} = m_c L_2 / [(t_2 - t_1) V_{bl} (T_s - T_{\ell})] \qquad (4.11)$$

Typical volumetric heat transfer coefficients have been calculated and are cited in the discussion.

4.3 Calculation of the Bubble Peclet Number

The bubble Peclet number was the dimensionless parameter used to characterize the bubble relative velocity. The bubble Peclet Number can be written as the product of the bubble Reynolds number and the liquid Prandtl number. The bubble Reynolds number was defined based on the bubble relative velocity

$$u_r = u_{\ell} - u_g \ . \qquad (4.12)$$

The bubble velocity u_g was determined from a linear least squares approximation to the bubble "instantaneous" velocity measured across 1 cm intervals along the downcomer (Section 4.1.3). The bubble Reynolds number was defined as

$$Re = \rho_{\ell} u_r D_{se} / \mu_{\ell} \ . \qquad (4.13)$$

The liquid Prandtl number was defined as

$$Pr = \mu_{\ell} c_p / k_f \ . \qquad (4.14)$$

The bubble local Peclet number was determined by

$$Pe = Re\ Pr\ . \tag{4.15}$$

The bubble position averaged Peclet number was calculated in the same fashion as the bubble position averged Nusselt number

$$\overline{Pe} = (1/N) \sum_{j=1}^{N} Pe\ . \tag{4.16}$$

4.4 Calculation of the Vapour Mass Flowrate

The calculation of the vapour mass flowrate was complicated by the presence of air in the separation tank. This was made apparent when the separation tank "vapour" temperature measurement was found to be lower than the saturation temperature corresponding to the static pressure measured. This indicated that a significant amount of air was present in the tank. To estimate the mass ratio of Freon vapour to air, Dalton's law of partial pressures was used. Assuming that the vapour and air were ideal gases and well mixed, the ratio of the partial pressure of the vapour to the measured static pressure was taken to be equal to the mass ratio of vapour to the entire vapour/air mixture. The mass fraction was calculated as

$$F_g = P_s/P_{st}\ . \tag{4.17}$$

The mass fraction was required to calculate the properties of the vapour/air mixture using the law of mixtures written as

$$x_m = F_g x_g + (1 - F_g)x_a\ . \tag{4.18}$$

The mixture properties were used in the calculation of the Nusselt and Reynolds numbers, which in turn, were used to determine the exhaust velocity of the mixture. Since exhaust velocity was measured at the center of the exhaust tube, it was necessary to infer an average velocity from the measurement. An iterative calculation was used to determine the exhaust tube Reynolds number which was found to be less than 2000 in all cases. The mixture average velocity was then taken to be

$$\bar{u}_m = 0.5\, u_m \tag{4.19}$$

The mass flowrate of the vapour/air mixture was obtained from the mixture average velocity

$$\dot{m}_m = (\rho_m)\bar{u}_m A_{ex} \tag{4.20}$$

The vapour mass flowrate was finally given by

$$\dot{m}_g = F_g \dot{m}_m \ . \tag{4.21}$$

CHAPTER V

RESULTS AND DISCUSSION

5.1 Qualifying Remarks

As with all investigations of a preliminary nature, some simplifications of the processes and events involved are necessary to gain a sufficient overview of the subject matter in a limited time and budget frame. The intent is usually to gain a basic understanding of the problems involved and to seek general trends to at least partially quantify the parameters of interest. The present study was conducted in this spirit and consequently detailed information concerning the local velocity, pressure, and temperature fields adjacent to each bubble were not obtained. Rather, estimates of the gross velocities, pressures and temperatures across the downcomer length were used to calculate quantities such as the condensation rates, and the Nusselt and Peclet numbers.

5.2 Experimental Error

The three types of experimental errors present in this study included instrumentation errors, time lapse errors, and judgement errors. Instrumentation errors were determined by the accuracy and precision of the individual measurement devices. Estimated errors for the measurements taken are given in Appendix C. Included are the assumption of linearity made during the calibration procedure for both the temperature probes and flowrate measurement device.

Time lapse errors resulted from the short delays in taking measurements of the time varying parameters. Included were liquid depth and pressure measurements in both the vacuum chamber and separation tank.

The delays were caused by the manually performed reading of each manometer and depth scale prior to the filming of the bubbles in the test section. The magnitude of the time lapse error was dependent on the operating conditions. Under higher liquid flowrates and temperatures, the liquid depth and pressure in both the vacuum chamber and separation tank varied more rapidly. This type of error, although difficult to quantify, is believed to be small since the filming intervals were extremely short in duration, usually less than a minute in length.

Judgement errors were the result of unavoidable reading errors during fluctuations in liquid depth, pressure, and temperature. They were reduced by averaging the maximum and minimum values of the parameter during fluctuation. This type of error was also dependent on the operating conditions. Larger fluctuations were observed at higher liquid flowrates and temperatures. The magnitude of judgement errors are thought to be considerably less than that of the time delay errors.

5.3 Rate of Decrease of Bubble Size

As determined by film analyses and data reduction procedures previously described, the variation of bubble volume and surface area for each of the bubbles tracked is presented as functions of time in Figures 4.3 to 4.16. The three digit designation for each bubble is used to relate each bubble to the experimental conditions during its filming. By example, bubble 613 refers to experiment No. 6, film roll number 1, and film sequence number 3. The experimental conditions for each run are listed in Tables 1 and 2.

To enable the calculation of bubble mass loss and heat transfer coefficients, the rates of decrease of bubble volume and surface area

were required. It was necessary to curve fit the data contained in Figures 4.3 to 4.16. The high degree of fluctuation in the data a discussed previously in Section 4.1.2, however, presented some difficulties. Attempts at using the correlations for bubble collapse rates in the literature reviewed were unsuccessful since the time scales were up to three orders of magnitude lower than observed in this investigation. It was decided a linear least squares fit of the data would be adequate in giving a preliminary unbiased estimate of the rate of decrease of bubble size. The slopes and intercepts of the least squares fits for each bubble are contained in Table 4.

For ease of comparison and to provide further physical insight into the rates of decrease of bubble size, the least squares fits of bubble volume and surface area have been replotted in dimensionless form as functions of bubble position along the downcomer. The bubble position has been normalized with respect to the total length of the downcomer. Figures 5.1 and 5.2 contain the variation of bubble volume and surface area along the downcomer for all the bubbles tracked. It is emphasized that the discussion at this point concerns only the rates of bubble size decrease. Discussion of the amount of vapour condensed follows in Section 5.4.

Figure 5.3 contains the variation of dimensionless bubble spherical equivalent diameter with normalized downcomer position. The spherical equivalent diameter was calculated to provide a characteristic length to determine the bubble Nusselt and Peclet numbers. It, however, may also be viewed to be a representative function of the relationship between the bubble volume and surface area. A low volume to surface area ratio indicates a large departure from sphericity since it is well known that

with spherical shapes, volume per unit surface area is maximized. As an estimate of the sphericity of each bubble, a volume based aspect ratio was calculated by dividing the initial spherical equivalent diameters $(D_{se})_i$, as based on the ratio of volume to surface area, by an alternative form of a spherical equivalent diameter $(D_{sev})_i$, based solely on the initial volume as defined by

$$D_{sev} = (6\ V_b/\pi)^{1/3} \tag{5.1}$$

The aspect ratios for each bubble are listed in Table 3.

To estimate the flow field around each bubble, a nominal relative or slip velocity was calculated from the bubble instantaneous velocity. Due to the method with which the bubble instantaneous velocities were obtained (Section 4.1.3), a significant amount of scatter was generated in the data. Following the treatment of the bubble volume and surface area, it was decided a linear least squares fit of the instantaneous velocity data would be adequate. The nominal relative velocity was obtained by subtracting the instantaneous velocity from the downcomer inlet liquid velocity. The inlet liquid velocity was used as a reference since the local velocity field about each bubble was not known. The values were non-dimensionalized with the inlet liquid velocity and plotted as a function of the bubble normalized position along the downcomer. The nominal relative velocities for all the bubbles tracked are shown in Figure 5.4. It is apparent that the relative velocities may increase or decrease. This is due in part to the influence of the wakes of larger bubbles which create turbulent eddies, which in turn, may accelerate, deccelerate, or change the trajectory of similarly sized or

smaller bubbles. Bubble shape oscillations may also increase or decrease the drag coefficient thus changing the bubble velocity. To supplement the plot of the instantaneous relative velocities, average relative velocities were calculated. These were based on the average bubble velocities as determined from the procedure outlined in Section 4.1.3. The average relative velocities are listed in Table 4.

In Figures 5.1 to 5.3, it is interesting to note some parallelism of the curves even though the tracking intervals were widely distributed along the length of the downcomer. This was not unexpected since the rate of increase of hydraulic pressure does not vary with position along the downcomer. The non-dimensionalization of the volume and surface area with respect to the initial values shows the apparent insensitivity of the collapse rates to initial bubble size. This observation, however, should be tempered with regard to the fact that the majority of the bubbles were fairly similar in size.

Each of the four plots (Figures 5.1 to 5.4) has been subdivided and the curves grouped according to the experimental parameter of downcomer inlet liquid temperature. Figures 5.5 to 5.7, Figures 5.8 to 5.10, and Figures 5.11 to 5.13 repeat Figures 5.1 to 5.3, respectively at inlet liquid temperatures of 11, 12, and 13 °C. The clearest example of the parallelism between the curves are shown in Figures 5.7, 5.10, and 5.13. The experimental conditions for each of these bubbles were identical and all of these bubbles were similarly sized. Bubble 822 had an unusually low rate of surface area decrease which appears to have been moderated by the rate of volume decrease when the spherical equivalent diameter was calculated. The low collapse rate of bubble 822 may be partially attributable to its near sphericity. Having an aspect ratio of 0.917,

bubble 822 had a proportionally lower surface area available for heat and mass transfer in comparison to the other bubbles in this group. Any convective effects which would aid the heat and mass transfer of the other bubbles in the group appear to be negligible since bubble 822 had one of the higher average slip velocities of all the bubbles in the group.

In Figures 5.5, 5.8 and 5.11 less parallelism is shown between the curves. Bubbles 311, 621, and 622 have similar rates of size decrease in comparison to the bubbles grouped at the inlet liquid temperature of 13 °C. Bubbles 613 and 624, however, have lower rates of size decrease. The possible reasons behind this are not clear. The two bubbles have the lowest aspect ratios in the group suggesting that perhaps the slip velocities of the other bubbles were high enough to effect a higher heat and mass transfer thus compensating for their relatively smaller surface areas. The relative magnitudes of the slip velocities indicate otherwise.

Referring to Figures 5.6, 5.9 and 5.12, bubbles 721 and 731 show size decrease rates comparable to the majority of the other bubbles. Bubble 722, however, has the lowest rate of surface area decrease among all the bubbles. Aside, with regard to bubble 722 in Figure 5.12, because of the extremely low rate of surface area decrease in proportion to the rate of decrease of volume, its spherical equivalent diameter drops off at a higher rate than for bubble 721. Bubble 721 is by far the largest bubble tracked whereas bubble 722 is one of the smallest bubbles tracked. Bubble 731 is of similar size to bubble 722. This emphasizes the near sphericity of small bubbles in comparison to large bubbles when the aspect ratios of these bubbles are examined.

Continuing, bubble 722, though being one of the smallest bubbles tracked, had the highest nominal average slip velocity. Both its near sphericity and high slip velocity contradict its low collapse rate. More detailed information concerning the pressure and flow fields surrounding the bubble is required to provide possible reasons for the discrepancies.

Comparisons to previous bubble collapse studies are difficult to justify as the conditions under which collapses proceed in this study occur under a varying pressure environment instead of a step pressure application as discussed previously. It is sufficient to state that bubble collapse rates are significantly slower under a varying pressure environment. The impulse experienced by bubbles in collapses initiated by a step pressure application appears to lead to more rapid collapses.

5.4 Bubble Condensation Rate

Estimates of the condensation rate for each bubble was determined in conjunction with the Nusselt number calculation as described previously in Section 4.2. It was necessary to extrapolate the least squares fits of the decrease of bubble volume with position back to the downcomer entrance to obtain approximate initial volumes for each bubble. This assumes identical collapse rates outside the tracking length. This may not be justifiable, but the extrapolated portions of the condensation rates for each bubble do give a probable collapse rate based on available data. Beginning with the initial mass calculated from the extrapolated initial volume, the mass loss across 1 cm increments was calculated and subtracted from the retained mass to obtain the condensation rate for individual bubbles.

Figure 5.14 shows the dimensionless condensation curves for all the bubbles tracked as functions of normalized position along the downcomer. The extrapolated parts of each curve lie outside the portion bounded by two dots. The downward concavity of the curves is a result of the linear approximation of the decrease of bubble volume. Since the rate of decrease of bubble volume was taken to be constant, the mass condensed per centimeter increment of downcomer length becomes progressively larger as vapour density increases with hydraulic pressure. Subtraction of the calculated mass condensed from the retained vapour mass yields a nonlinear reduction in vapour mass. The extrapolated condensation curves indicate that two bubbles would survive the length of the downcomer. Bubbles 622 and 624 would retain approximately 6% and 32% of their original masses respectively. The remainder of the bubbles tracked however, would collapse at various points along the downcomer. Complete collapses of bubbles were not however, visually confirmed during experimentation. The linear approximation of the rate of decrease of bubble volume coupled with the hydraulic pressure induced increase of vapour density may have resulted in the overestimation of the condensation rates. The condensation rates presented are conservative in the sense that they may be viewed as upper bound rates. Figures 5.15 to 5.17 repeat Figure 5.14 to aid in distinguishing between the curves. As previously, the curves are grouped according to the inlet liquid temperature. It is apparent that the curves reflect the variation in slopes of the least squares fits of the volume data in each of the three plots.

5.5 Heat Transfer Rate

To quantify the heat lost through condensation, bubble external overall heat transfer coefficients were calculated. The values of the heat transfer coefficients based on bubble surface area ranged from 6 to 775 W/m^2 °C. These were considerably lower than those obtained by Levenspiel [11] (50 kW/m^2 °C), and Brucker and Sparrow [19] (10 kW/m^2 °C). A more favourable comparison with existing data was obtained when the volumetric heat transfer coefficients were considered. The volumetric heat transfer coefficients estimated in this study ranged from 24 to 957 kW/m^3 °C. These values agreed well with those of Sideman and Moalem [26] (12 to 232 kW/m^3 °C) obtained for a pentane co-current flow system. Sideman and Moalem did not give a general range of sizes of their bubbles. The discrepancy between the data obtained for the surface area based heat transfer coefficients may be partially attributable to the extremely large surface area to volume ratios of the ellipsoidal bubbles in this study.

To broaden the applicability of the heat transfer coefficients to other fluids and operating conditions, the results were non- dimensionalized in Nusselt number form. The calculation procedure for Nusselt number is contained in Section 4.2. Only the surface area based heat transfer coefficients were non-dimensionalized to adhere to normal practice pursued in the literature.

Figure 5.18 shows the local external Nusselt number for each bubble tracked plotted versus their repsective normalized positions along the downcomer. The general trend is one of rapid decrease near the downcomer entrance with gradual stabilization towards the exit of the downcomer. The high Nusselt numbers near the downcomer entrance are a

direct result of the extremely low driving temperature difference near the site of bubble formation. This is necessarily the case since the vapour mass condensed is calculated based on a constant rate of decrease of bubble volume. The steep inclination of the driving temperature difference near the downcomer entrance is illustrated in dimensionless form in Figure 5.19 for all the bubbles tracked. The highest local Nusselt number obtained was 16.05, the lowest was 0.10.

Figures 5.20 to 5.22 repeat Figure 5.18 in the previous fashion. An interesting event occurs as shown in Figure 5.20. Bubbles 311, 621, and 622 collapse neatly onto a single composite curve forming in effect a track of a composite bubble taken over 80% of the downcomer length. The Nusselt number variation of bubble 613 appears to parallel the composite curve.

To investigate the effects of relative velocity on the heat transferred from vapour to liquid, local Nusselt numbers were plotted as functions of local Peclet numbers. The local Peclet numbers were calculated as described in Section 4.3. Figure 5.23 shows the relationship between the local Nusselt and Peclet numbers for all the bubbles tracked. In general as expected, higher Nusselt numbers corresponded to higher Peclet numbers. Bubbles 311 and 813, however, contradict this trend. Bubble 311 has an extremely low slip velocity in comparison to the other bubbles. At this magnitude, the increase in condensation caused by convection due to the slip velocity may well be negligible. The slight decrease of Nusselt number with Peclet number for bubble 813 is well within the error brought about by the coarseness of the linear least squares fits of the bubble velocity and size decrease raw data.

The position averaged values of the Nusselt and Peclet numbers were calculated and plotted in Figure 5.24 for individual bubbles. In general, the Nusselt number appears to be a weak function of the Peclet number. The convective effects over this relative velocity range did not significantly affect the heat transfer. As a reference, the relationship between Nusselt and Peclet number for a fluid sphere in potential flow is also plotted. The Nusselt numbers obtained in this investigation are considerably lower than those predicted by the potential flow model. This is understandable in view of the assumption of perfect heat transfer used in the potential flow model. The position averaged Nusselt number ranged from 0.10 to 6.68. The position averaged Peclet numbers ranged from 5516 to 22699. The considerable scatter is primarily a result of the turbulence encountered by each bubble. The wide variations in the slip velocity are reflected in the Peclet number.

An estimate of the possible uncertainty in the Nusselt number is given in Appendix C. Within the limits of the assumptions made in the analysis, the uncertainty in the bubble local external Nusselt number is approximately 37%.

5.6 Vapour Mass Flowrate

The primary reason for the measurement of vapour mass flowrate was to obtain qualitative data on the relationships between HVC operating parameters and the vapour mass flowrate. The HVC parameters that were independently varied included inlet liquid flowrate and temperature. The inlet liquid flowrate was a direct function of the applied pressure ratio across the length of the downcomer. Figure 5.25 contains plots of vapour mass flowrate versus liquid mass flowrate. Each curve represents

quantities obtained at varying vapour temperatures as measured in the separation tank. The increase in overall magnitude of vapour mass flowrate with vapour temperature can be directly attributed to the larger cavitation jets formed at higher inlet liquid temperatures. The larger cavitation jets introduced correspondingly larger amounts of vapour into the flow. The relationship between the liquid and vapour temperatures is shown in Figure 5.26. Referring to an individual curve in Figure 5.25, the vapour mass flowrate can be seen to increase with liquid mass flowrate. The increase is more pronounced at higher vapour temperatures. This could be attributed to a non-linearity in flashing rate at the downcomer inlet as the inlet liquid temperature approaches saturation.

In comparison to HAC, it appears that at least on a laboratory scale, HVC produces a slightly lower output for a given liquid flowrate. Rice [5] achieved a maximum air/water mass flowrate ratio of 1.91E-4 (at a mass flowrate of air of 4.02E-5 kg/s) in a 1.905 cm diameter downcomer. The maximum vapour/liquid mass flowrate ratio obtained in this study was 1.27E-4 (at a mass flowrate of vapour of 1.01E-4 kg/s) in a 2.54 cm diameter downcomer. In consideration of the mass loss through condensation along the downcomer, the quantity of vapour entrained into the downcomer may well be similar to that achievable in a hydraulic air compressor.

CHAPTER VI

CONCLUSIONS AND RECOMMENDATIONS

6.1 Condensation and Heat Transfer Rate

During HVC, the mass condensation rates have been found to increase along the length of the downcomer. The lowest calculated mass transfer rates occurred near the downcomer entrance with the highest calculated rates occurring at the exit. This finding is significant because it suggests that vapour mass losses may be minimized by using a multiplicity of cascading compression stages to achieve a desired delivery pressure.

The condensation rates presented in Figure 5.14 may be viewed as an upper bound for estimating the vapour mass losses in the HVC process. Extrapolation of the inferred condensation rates predict that the majority of the vapour bubbles induced into the downflow would condense entirely before arrival at the exit of the test section. This was not visually confirmed during experimentation. The linear least squares method of approximating the rate of change of bubble volume used to calculate the mass transferred may have resulted in the overestimation of the condensation rates.

The local external Nusselt numbers used to characterize the magnitude of the heat transferred through vapour condensation ranged from 0.1 to 16. The highest local Nusselt numbers were calculated to occur near the entrance of the downcomer. This was primarily due to the existence of extremely low driving temperature differences near the downcomer entrance. As the variation of the heat transfer rate from the vapour to the liquid was based on a linear least squares approximation

of the decrease in bubble volume, the average values of the local Nusselt numbers presented may be more indicative of the actual heat transfer rates occurring during the HVC process.

"The bubble external Nusselt numbers were found not to be a strong function of bubble Peclet numbers." Within the range of relative velocities considered here, the heat transfer off the bubble surface did not appear to strongly depend on convection.

6.2 Technical Feasibility of Hydraulic Vapour Compression

The technical feasibility of HVC is dependent on the minimization of the vapour condensation rates which result from the compression process. The output gas mass flowrate of the laboratory scale hydraulic vapour compressor studied here compared favourably with a similarly sized hydraulic air compressor. The comparison was based entirely on output gas mass flowrates without regard to the inlet or initial gas mass flowrates. The favourable comparison indicated that **the condensation rates occurring in the hydraulic vapour compressor were not sufficiently severe that the output gas mass flowrate was reduced substantially** below that of the hydraulic air compressor. Since only output gas mass flowrate was considered, **the possibility exists that the HVC process is able to induce or generate a greater initial gas mass flowrate than the HAC process.** Further study is required to determine possible output vapour temperatures for different compression ratios. The feasibility of the HVC process will be dependent on the ouptut vapour temperature.

6.3 Further Work

6.3.1 Modifications to the Apparatus and Instrumentation

Listed below are suggestions concerning possible improvements to the existing apparatus and instrumentation.

(a) The Nalgene bell jar should be replaced preferably with a glass bell jar to minimize slow leaks which developed due to the crazing of the Nalgene at the jar mouth.

(b) Multiple pressure taps placed along the length of the test section would allow a more accurate measurement of the pressure rise.

(c) Pressure and displacement transducers (for the measurement of liquid depth in both the vacuum chamber and separation tank) tied into the data acquisition system should be purchased to obtain more accurate and precise data. This would also allow the data collection during the actual filming intervals.

(d) The separation tank should either be insulated or replaced with one which has a much smaller free surface. This would minimize Freon evaporation which may result in the overestimation of the output vapour mass flowrate.

(e) For the filming of bubbles, a synchronized two-camera arrangement should be used. The cameras should be placed at ninety degrees to each other. This arrangement would result in an additional dimension upon which to base the calculation of bubble volumes. The refraction tube will have to be replaced with a square cross-section glass tube to allow the filming.

6.3.2 Suggestions Concerning the Film Analyses

Due to the discrete and nonrepeatable nature of this type of study, a statistical approach to the measurement of bubble collapse would be

highly desirable in the interests of accuracy. Such an approach, however, would be extremely time intensive and labourious without the proper analytical equipment. Machines are available which can distinguish varying shades of darkness of a given area in a photographic image (Hyzer [31]). This would provide the experimenter with a means for obtaining an unbiased measurement of the projected area of a bubble image. More sophisticated machines are able to digitize the bubble image directly allowing extremely fast processing of film data from the frame and bubble selection stage to the estimation of the bubble volumes. The speed of processing would certainly allow a statistical approach to be used in the measurement of bubble collapse.

6.3.3 Further Areas of Study

The process of HVC is very much in the early stages of development. The process can be divided into three distinct areas of investigation: the downcomer inlet vapour generation or induction scheme; the vapour condensation rate in the downcomer; the downcomer exit vapour/liquid separation scheme. Each of these areas requires further study and optimization. This work provides estimates of the vapour condensation rates as well as the achievable vapour mass output of a laboratory scale compressor. The discussion of further work is restricted to these two sets of results.

Further work on both the vapour condensation rate and the achievable vapour mass output should initially concern the verification of the results presented here. Ideally, such verification would involve the use of water as the working fluid in a compressor of a significantly larger scale. The use of water in the verification will be advantageous

since it is the intended working fluid in the open cycle heat pump for which the HVC process is slated. A larger scale experimental unit has the advantage of a higher volume flowrate capability. Higher volume flowrates would lessen the measurement error of each operating parameter.

Optimization logically follows verification. To minimize the vapour condensation rate, the two most important dimensionless parameters to consider would be the downcomer length to diameter ratio and the void fraction. For a given downcomer length, variation of the void fraction will dictate the achievable pressure ratio. The pressure ratio would control the volume flowrate through the downcomer. The effects of varying each dimensionless parameter, downcomer length to diameter ratio and void fraction, should be investigated to maximize the mass of vapour delivered.

Optimization logically follows verification. To minimize the vapour condensation rate, the three most important dimensionless parameters to consider would be the downcomer length to diameter ratio, the void fraction, and the bubble diameter to downcomer diameter ratio. For a given downcomer length, variation of the void fraction will dictate the achievable pressure ratio. The pressure ratio would control the volume flowrate through the downcomer. To minimize bubble condensation, the compression process must occur as quickly as possible. Extremely high flowrates are therefore desirable. Bubble size is an important parameter since smaller bubbles would maintain bubble sphericity. The volume per unit surface area would then be maximized and the available heat transfer area would be minimized. The effects of varying each dimensionless parameter should be investigated to maximize the mass of vapour delivered.

BIBLIOGRAPHY

1. Ryan, J.A., "Cycle Analysis for a Sea Water Heat Pump," University of British Columbia, Internal Report, 1983.

2. Langborne, P.L., "Hydraulic Air Compression, Old Invention - New Energy Source?", CME, Nov. 1979, pp. 76-80.

3. Isenberg, J., Moalem, D., Sideman, S., "Direct Contact Heat Transfer with Change of Phase: Bubble Collapse with Translatory Motion in Single and Two Component Systems," Proceedings of 4th Intl. Heat Transfer Conf., Vol. V, Paper B2.5, 1970.

4. Wallis, G.B., One-Dimensional Two-Phase Flow, McGraw-Hill, New York, 1969, pp. 243.

5. Rice, W., "Performance of Hydraulic Gas Compressors," ASME J. of Fluids Engng., Vol. 98, Dec. 1976, pp. 645-653.

6. Rice, W. and Chen, Li-Ting, "Effects of Incomplete Separation and of Air Solubility on the Performance of a Hydraulic Air Compressor (HAC)," Proceedings, Intl. Conf. on Hydropower. (Water Power '81), Washington, D.C., June 22-24, 1981.

7. Chen, Li-Ting and Rice, W., "Some Psychrometric Aspects of a Hydraulic Air Compressor (HAC)," ASME Journal of Energy Resources, Vol. 104, Sept. 1982, pp. 274-276.

8. Chen, Li-Ting and Rice, W., "Properties of Air Leaving a Hydraulic Air Compressor (HAC)," ASME J. of Energy Resources, Vol. 105, Mar. 1983, pp. 54-57.

9. Berghmans, J.A. and Ahrens, F.W., "Performance of a Hydraulic Air Compressor for Use in Compressed Air Energy Storage Power Systems."

10. Cliff, R., Grace, J.R. and Weber, M.E., Bubbles, Drops and Particles, Academic Press, New York, 1978.

11. Levenspiel, O., "Collapse of Steam Bubbles in Water," Industrial and Engineering Chemistry, Vol. 51, No. 6, June 1959, pp. 787-790.

12. Bankoff, S.G. and Mason, J.P., "Heat Transfer from the Surface of a Steam Bubble in Turbulent Subcooled Liquid Stream," A.I. Ch. E. Journal, Vol. 8, No. 1, Mar. 1962, pp. 30-33.

13. Florschuetz, L.W. and Chao, B.T., "On the Mechanics of Vapour Bubble Collapse," ASME J. of Heat Transfer, Series C, Vol. 87, No. 2, May 1965, pp. 209-220.

14. Wittke, D.D., Ph.D. Thesis, University of Illinois, Urbana, 1966.

15. Wittke, D.D. and Chao, B.T., "Collapse of Vapour Bubbles With Translatory Motion," ASME J. of Heat Transfer, Series C, Vol. 89, No. 1, February 1969, pp. 157-159.

16. Hewitt, H.C. and Parker, J.D., "Bubble Growth and Collapse in Liquid Nitrogen," ASME J. of Heat Transfer, February 1968, pp. 22-25.

17. Board, S.J. and Klimpton, A.D., "Spherical Vapour Bubble collapse," Chemical Engineering Science, Vol. 29, 1974, pp. 363-371.

18. Delmas, H. and Angelino, H., 'Contraction de bulles de vapeur non-spheriques," Canadian J. of Chemical Engineering, Vol. 55, Dec. 1977, pp. 644-650.

19. Brucker, G.G. and Sparrow, E.M., "Direct Contact Condensation of Steam Bubbles in Water at High Pressure," Intl. J. Heat Mass Transfer, Vol. 20, 1977, pp. 371-381.

20. Moalem, D., Sideman, S., Orell, A., and Hetsroni, G., "Direct Contact Heat Transfer with Change of Phase: Condensation of a Bubble Train," Intl. J. Heat Mass Transfer, Vol. 16, 1973, pp. 2305-2319.

21. Sekoguchi, K., Fukui, H., and Sato, Y., "Flow Characteristics and Heat Transfer in Vertical Bubble Flow," Two-Phase Flow Dynamics, Hemisphere Publishing Corp., Washington, 1979, pp. 59-74.

22. Ruckenstein, E., "On Heat Transfer Between Vapour Bubbles in Motion and the Boiling Liquid From Which They are Generated," Chemical Engineering Science, No. 10, 1959, pp. 22-30.

23. Moalem, D. and Sideman, S., "The Effect of Motion on Bubble Collapse," Intl. J. Heat Mass Transfer, Vol. 16, 1973, pp. 2321-2329.

24. Dimic, M., "Collapse of One-Component Vapour Bubble With Translatory Motion," Intl. J. Heat Mass Transfer, Vol. 20, 1977, pp. 1325-1332.

25. Prisnyakov, V.F., "Condensation of Vapour Bubbles in Liquid," Intl. J. Heat Mass Transfer, Vol. 14, 1971, pp. 353-356.

26. Moalem, D., Sideman, S., Orell, A., Hestroni, G., "Condensation of Bubble Trains: An Approximate Solution," Prog. Heat Mass Transfer, 6, 1972, pp. 155-157.

27. Sideman, S. and Moalem, P., "Direct Contact Heat Exchangers: Comparison of Counter and Co-Current Condensers," Intl. J. Multiphase Flow, Vol. 1, 1974, pp. 555-572.

28. Ryan, J.A., M.A.Sc. Thesis, University of British Columbia, 1983.

29. Knapp, R.T., Daily, J.W. and Hammitt, F.G., Cavitation, McGraw-Hill, New York, 1970, pp. 1-19.

30. Mayinger, F., "Scaling and Modelling Laws in Two-Phase Flow and Boiling Heat Transfer," Two-Phase Flows and Heat Transfer, Vol. 1, Hemisphere Publishing Corp., Washington, 1977, pp. 129-161.

31. Hyzer, W.G., Engineering and Scientific High Speed Photography, Macmillan, New York, 1962.

32. Kline, S.J., and McClintock, F.A., "The Description of Uncertainties in Single Sample Experiments," Mechanical Engineering, Jan., 1953, pp. 3.

APPENDIX A

HOT FILM ANEMOMETRY DETAILS AND CALIBRATION PROCEDURE

The geometric and operation details of the Thermosystem Inc. (TSI) model 1235W parabolic hot film wedge probe are given in Table A.1. The probe was calibrated against a pitot tube in an open wind tunnel. The tunnel air velocity was calculated from the dynamic pressure p_d

$$u_a = (2.0\ p_d/\rho_a)^{0.5} \ . \qquad (A.1)$$

The probe Reynolds number based on the film length was given by

$$Re_p = \rho_a u_a L_f/\mu_a \ . \qquad (A.2)$$

The probe Nusselt number based on the film length was determined by equating the heat transferred through convection and the electrical power dissipated

$$Nu_p = [(E^2\ R_p)L_f]/[(R_p + R_3)^2\ L_f W_f\ (T_p - T_e)k_a] \ , \qquad (A.3)$$

where the air thermal conductivity k_a was evaluated at the film temperature

$$T_f = 0.5\ (T_p + T_e) \ . \qquad (A.4)$$

The form of the cooling law used was based on King's law

$$Nu_p = A + B\ Re_p^n \ . \qquad (A.5)$$

Figure A.1 shows the parabolic hot film wedge probe calibration curve. The calibration constants obtained were

$$A = 233.2 \ ,$$

$$B = 195.7 \ ,$$

$$n = 0.23 \ .$$

The vapour/air mixture velocities exiting the separation tank were determined by calculating the probe Reynolds number as a function of the probe Nusselt number. The probe Nusselt number was calculated from

$$Nu_p = [E^2(T'_e/T_e)R_pL_f]/[(R_p + R_3)^2\ L_fW_f\ (T_p - T'_e)k_m] \ . \qquad (A.6)$$

where the mixture thermal conductivity k_m was calculated from the law of mixtures by

$$k_m = F_g k_g + (1 - F_g)k_a \ , \qquad (A.7)$$

with the conductivities of both the air and vapour evaluated at the film temperature

$$T_f = 0.5\ (T_p + T'_e) \ . \qquad (A.8)$$

The probe Reynolds number Re_p determined from Equation (A.5) was used to calculate the vapour/air mixture velocity

$$u_m = (\mu_m \, Re_p)/(\rho_m L_f) \; . \qquad (A.9)$$

The mixture density ρ_m and dynamic viscosity μ_m were calculated from the law of mixtures

$$\rho_m = E_g \, \rho_g + (1 - F_g)\rho_a \qquad (A.10)$$

and

$$\mu_m = F_g \, \mu_g + (1 - F_g)\mu_a \; . \qquad (A.11)$$

APPENDIX B

RATE OF HEAT TRANSFER BETWEEN THE VAPOUR AND LIQUID PHASES

The heat transferred away from the bubble may be determined directly from the first law of thermodynamics for a closed system. Consider a vapour bubble enclosed by a thin liquid film moving through an increasing hydrostatic pressure field from position 1 to position 2 as shown in Figure B.1. As the bubble moves to position 2, compression of the vapour creates a temperature driving force for heat transfer at the system boundary. The compression process in the central portion of the vapour bubble is essentially isentropic whereas the remainder of the vapour external to the central portion is compressed isothermally.

The first law written in differential form is

$$dQ = dE - dW \; . \tag{B.1}$$

The change in internal energy is

$$dE = (m_{g2}e_{g2} - m_{g1}e_{g1}) + (m_{\ell 2}e_{\ell 2} - m_{\ell 1}e_{\ell 1}) + (m_{g2}gz_2 - m_{g1}gz_2) + (m_{\ell 2}gz_2 - m_{\ell 1}gz_1) \; . \tag{B.2}$$

The work done at the liquid film interface is

$$dW = -p\,[(m_{g2}v_{g2} - m_{g1}v_{g1}) + (m_{\ell 2}v_{\ell 2} - m_{\ell 1}v_{\ell 1})] \; . \tag{B.3}$$

Substituting Equations (B.2) and (B.3) into Equation (B.1), the heat transferred becomes

$$dQ = (m_{g2}e_{g2} + m_{g2}pv_{g2}) - (m_{g1}e_{g1} + m_{g1}pv_{g1})$$
$$+ (m_{\ell 2}e_{\ell 2} + m_{\ell 2}pv_{\ell 2}) - (m_{\ell 1}e_{\ell 1} + m_{\ell 1}pv_{\ell 1}) \qquad (B.4)$$
$$+ (m_{g2}gz_2 - m_{g1}gz_1) - (m_{\ell 2}gz_2 - m_{\ell 1}gz_1) ,$$

or

$$dQ = (m_{g2}h_{g2} - m_{g1}h_{g1}) + (m_{\ell 2}h_{\ell 2} - m_{\ell 1}h_{\ell 1})$$
$$+ (m_{g2}gz_2 - m_{g1}gz_1) - (m_{\ell 2}gz_2 - m_{\ell 1}gz_1) . \qquad (B.5)$$

For small increments in position, the potential energy terms may be neglected thus the heat transferred from the bubble is

$$dQ = (m_{g2}h_{g2} - m_{g1}h_{g1}) + (m_{\ell 2}h_{\ell 2} - m_{\ell 1}h_{\ell 1}) . \qquad (B.6)$$

Manipulation of Equation (B.6) leads to

$$dQ = (m_{g2} - m_{g1})h_{g2} - m_{g1}(h_{g2} - h_{g1})$$
$$+ (m_{\ell 2} - m_{\ell 1})h_{\ell 2} + m_{\ell 1}(h_{\ell 2} - h_{\ell 1}) . \qquad (B.7)$$

From continuity, the mass equality is

$$m_{\ell 2} - m_{\ell 1} = -(m_{g2} - m_{g1}) . \qquad (B.8)$$

Substituting Equation (B.8) into Equation (B.7), the heat transferred becomes

$$dQ = (m_{g2} - m_{g1})(h_{g2} - h_{\ell 2}) + m_{g1}(h_{g2} - h_{g1}) + m_{\ell 1}(h_{\ell 2} - h_{\ell 1}). \quad (B.9)$$

The difference in the vapour mass flowrate between positions 1 and 2 is the mass condensed. This was calculated using the linear least fit slope obtained for the measured decrease in bubble volume as

$$m_{g2} - m_{g1} = (\rho_{g2} - \rho_{g1})V_{b_1} + \rho_{g2}(V_{b2} - V_{b1}) . \quad (B.10)$$

The vapour densities in Equation (B.10) were taken to be the saturation values corresponding to the local pressure. These are approximations to the actual vapour densities which lie above saturation. The difficulty in determining the actual vapour densities stems from the fact that the compression process lies between an isentropic process and an isothermal process. Since small differences in vapour densities have been considered, the error of the approximation in negligible in comparison to the error incurred in the estimation of the rate of decrease of bubble volume.

The difference in the vapour and liquid enthalpies at position 2 is the heat released through condensation

$$h_{g2} - h_{\ell 2} = L_2 . \quad (B.11)$$

Substituting Equations (B.10) and (B.11) into Equation (B.9) and dividing by the time increment, the rate of heat transferred may be written as

$$\frac{dQ}{dt} = [((\rho_{g2} - \rho_{g1})V_{b1} + \rho_{g2}(V_{b2} - V_{b1}))L_2 + m_{g1}(h_{g2} - h_{g1}) + m_{\ell 1}(h_{\ell 2} - h_{\ell 1})]/(t_2 - t_1) . \quad (B.12)$$

APPENDIX C

ERROR ANALYSIS

The list of estimated errors for pressure, temperature and flowrate measurements are contained in Table C.1. Often, fluctuations of the measurements determined the reading accuracy.

An attempt at quantifying the possible error in the calculated bubble local external Nusselt number was made through the analysis given [32]. If Y is the dependent variable and $Y = Y(x_1, x_2, \ldots, x_n)$, then the percentage uncertainty of the result is $\pm y/Y$ with

$$y/Y = \{[(e_1 \partial Y/\partial x_1)/Y]^2 + [(e_2 \partial Y/\partial x_2)/Y]^2 + \ldots [(e_n \partial Y/\partial x_n)/Y]^2\}^{0.5} \qquad (C.1)$$

where e_1 to e_n are the uncertainties or probable errors of the variables x_1 to x_n respectively.

The local external Nusselt number is given by

$$Nu = [6(\rho_{g2} - \rho_{g1})(dV_b/dt)V_b]/[A_b^2 (T_s - T_\ell)k_f] \qquad (C.2)$$

Partial differentiation of the Nusselt number with respect to each of the variables in Equation (C.2) followed by division with the Nusselt number yields

$$[\partial Nu/\partial(\rho_{g2} - \rho_{g1})]/Nu = 1/(\rho_{g2} - \rho_{g1}), \qquad (C.3)$$

$$[\partial Nu/\partial(dV_b/dt)]/Nu = 1/(dV_b/dt), \qquad (C.4)$$

$$[\partial Nu/\partial V_b]/Nu = 1/V_b , \qquad (C.5)$$

$$[\partial Nu/\partial A_b]/Nu = -2/A_b , \qquad (C.6)$$

$$[\partial Nu/\partial(T_s - T_\ell)]/Nu = -1/(T_s - T_\ell) , \qquad (C.7)$$

$$[\partial Nu/\partial k_f]/Nu = -1/k_f . \qquad (C.8)$$

Having defined the partial derivatives, the related uncertainties are now considered. The uncertainties of the vapour density and the saturation temperature are dependent on the uncertainty in the pressure measurements taken at the vacuum and separation vessels, and the assumption of a linear pressure gradient between the two measurements. Both the vapour density and the saturation temperature are obtained from the Freon-11 saturation table given the pressure at any point along the downcomer. The percentage uncertainty in the pressure measurements is estimated to be 1%. The uncertainty introduced by the assumption of linearity between the pressures in the two vessels is likely to be much smaller than the uncertainty in the actual measurements due to the low flow velocities and short length of downcomer used. The determination of the values of vapour density and the saturation temperature from the Freon-11 saturation table introduces an additional error. This error, however, is negligible because of the limited operational pressure range used in this experiment (75 kPa < pressure < 104 kPa). Both the vapour density and the saturation temperature are approximately linearly

related to the pressure and thus their uncertainties may also be taken as 1%. The uncertainty in the measurement of the liquid temperature is 2% as given by the probe manufacturer.

The uncertainty of the film conductivity is dependent on both the pressure measurements and the liquid temperature measurements. It is sufficient that the uncertainty of the film conductivity be taken to be equal to the uncertainty of the liquid temperature measurement.

The largest uncertainty belongs to the measurements of bubble surface area and volume. Based on a probable bubble trace error of 10%, the error introduced by assuming a volume of revolution would likely be significantly smaller. The total error for a given estimate of the bubble surface area or volume is taken to be 15%. The uncertainty introduced by the linear least squares approximation of the variation of bubble volume with time was difficult to quantify. The standard deviation varied tremendously and was often greater than one. In view of this, the standard deviation would not be useful as an estimate of he uncertainty introduced by the curve fitting. It is reasonable to assume that the uncertainty is at least the same magnitude as the bubble surface area and volume uncertainty.

When the uncertainties are given in percentages, Equation (C.1) reduces to the square root of the sum of squares of the uncertainties. Thus the uncertainty of the bubble local external Nusselt number is calculated to be approximately 37%.

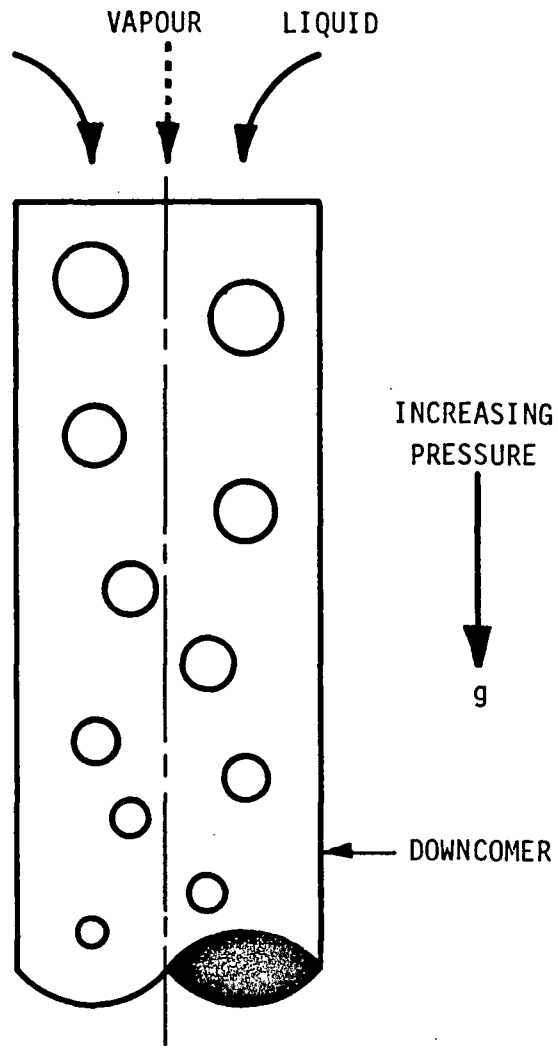

Fig. 1.1 Schematic of the Hydraulic Compression Process

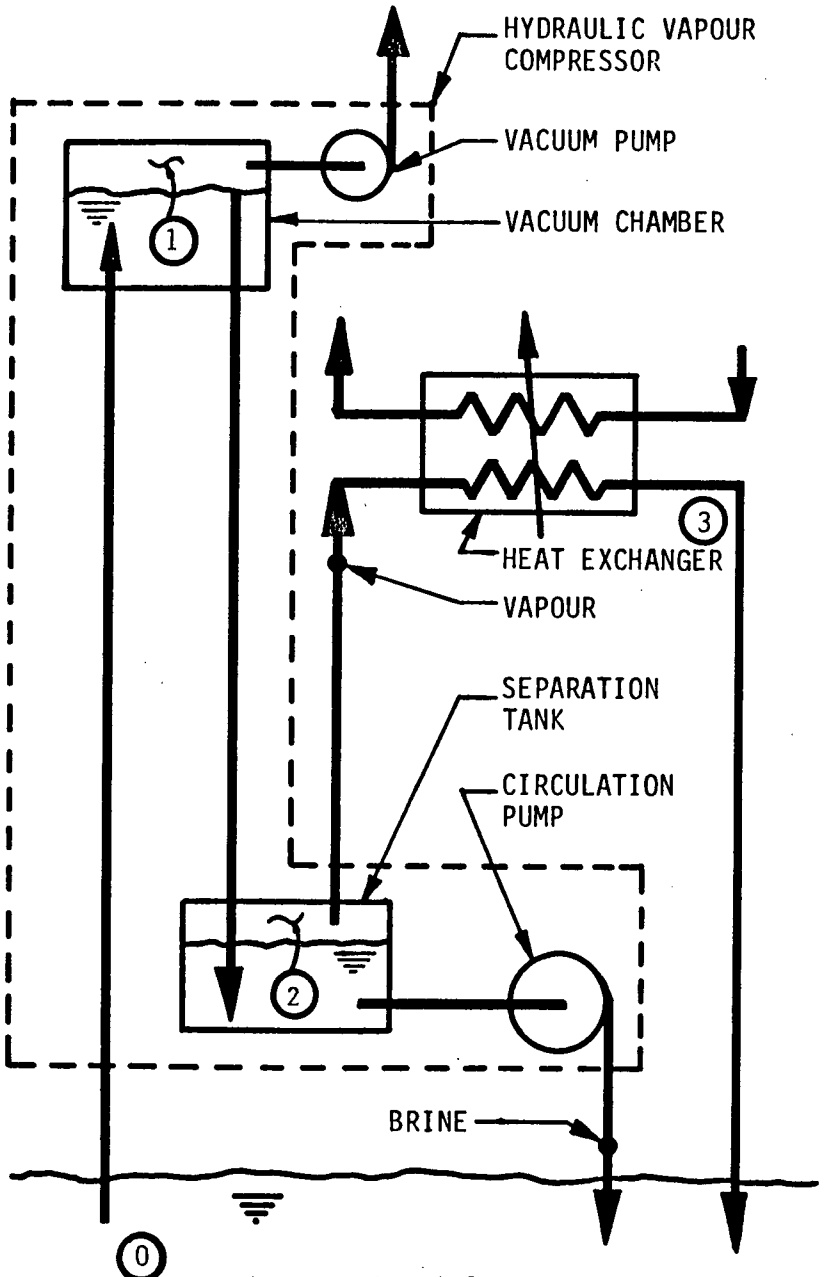

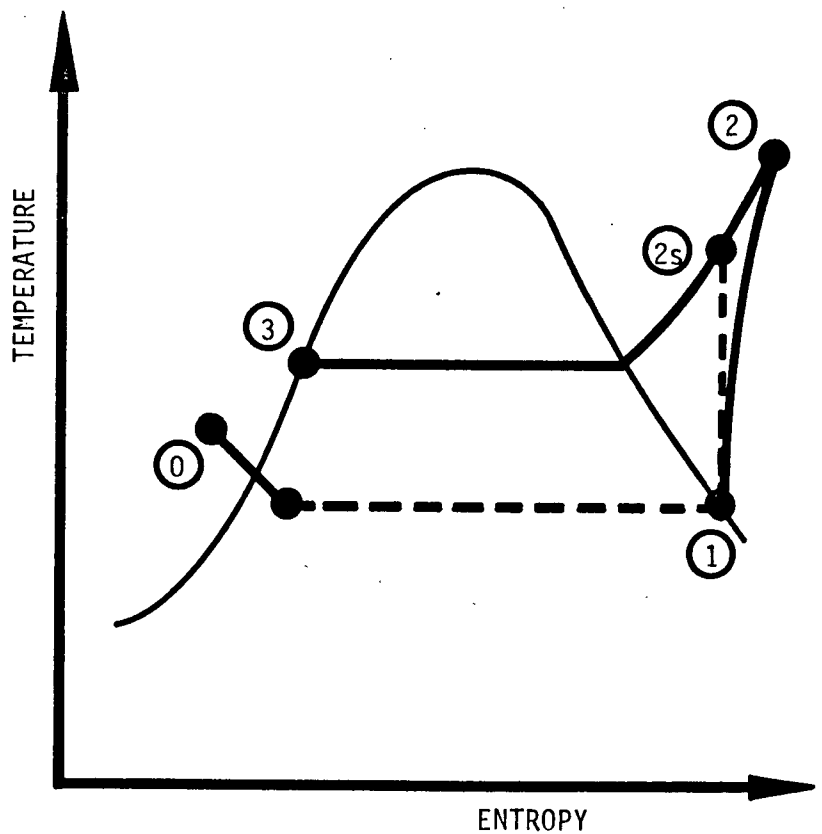

Fig. 1.2 Schematic of the Single Compression Stage Open Cycle Heat Pump

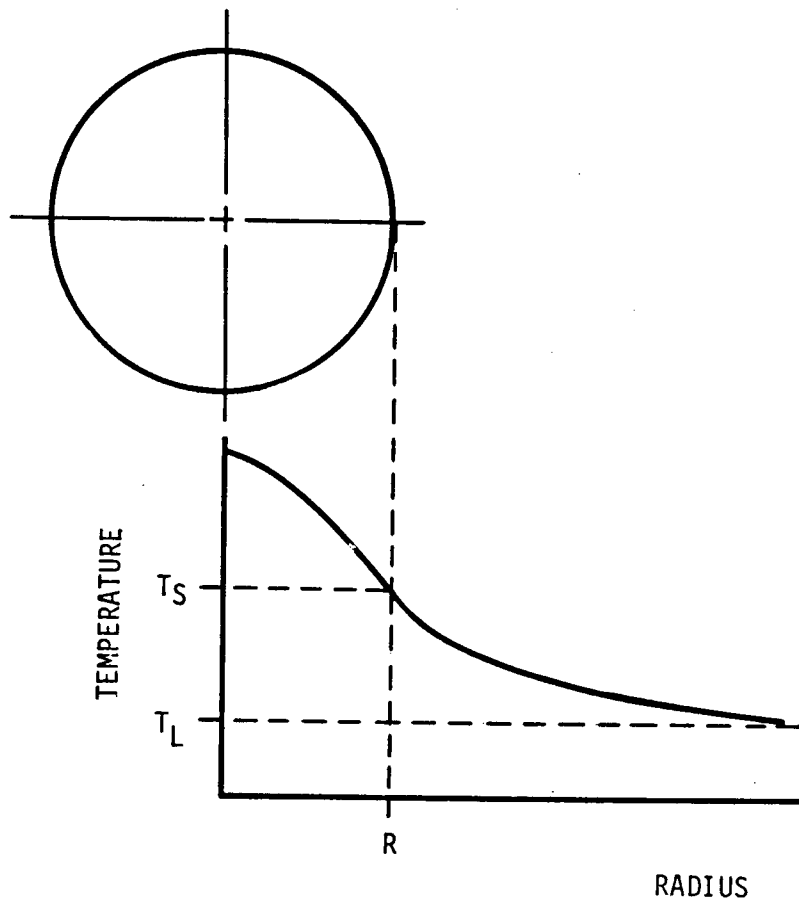

Fig. 1.3 Schematic of the Hypothetical Radial Temperature Profile of a Vapour Bubble During Compression

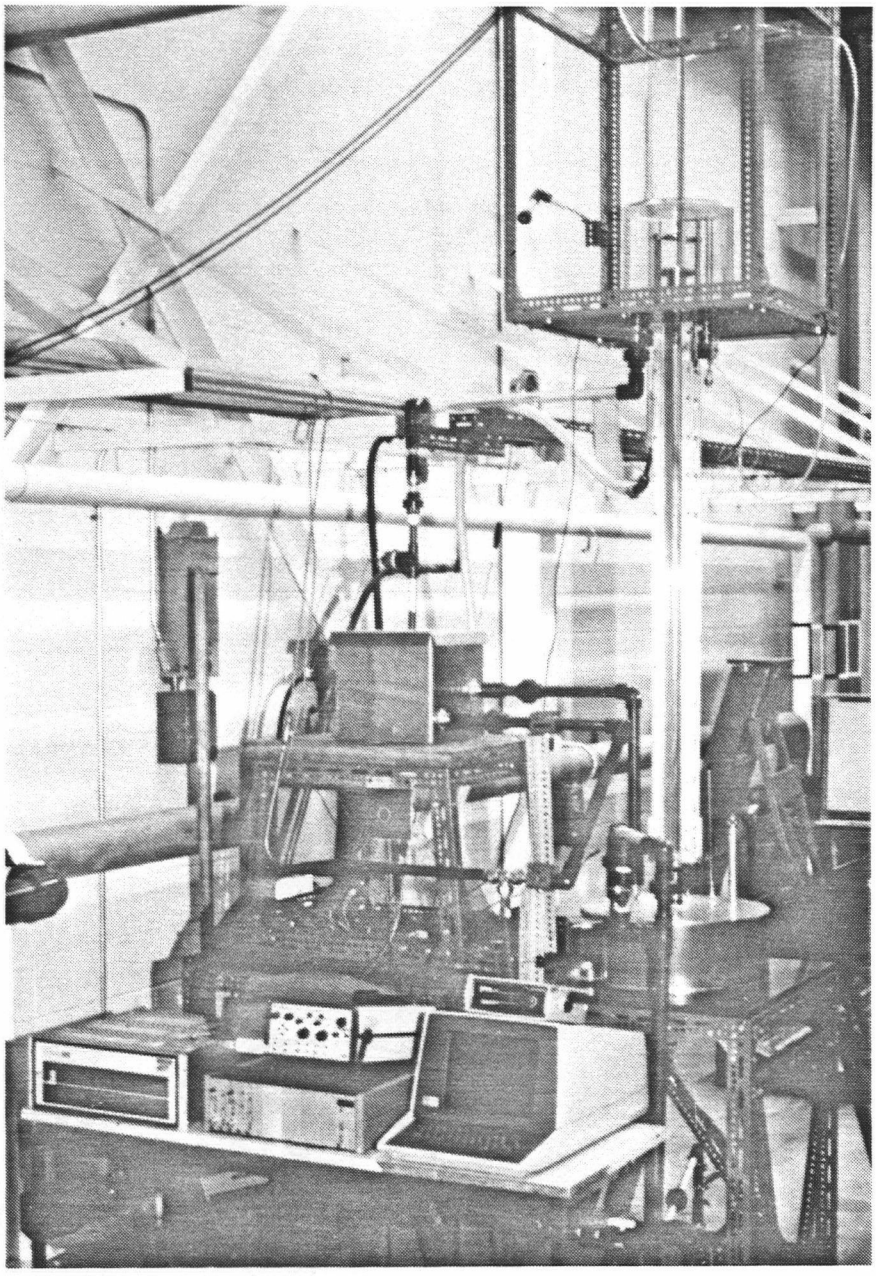

Fig. 2.1 Photograph of the Experimental Apparatus

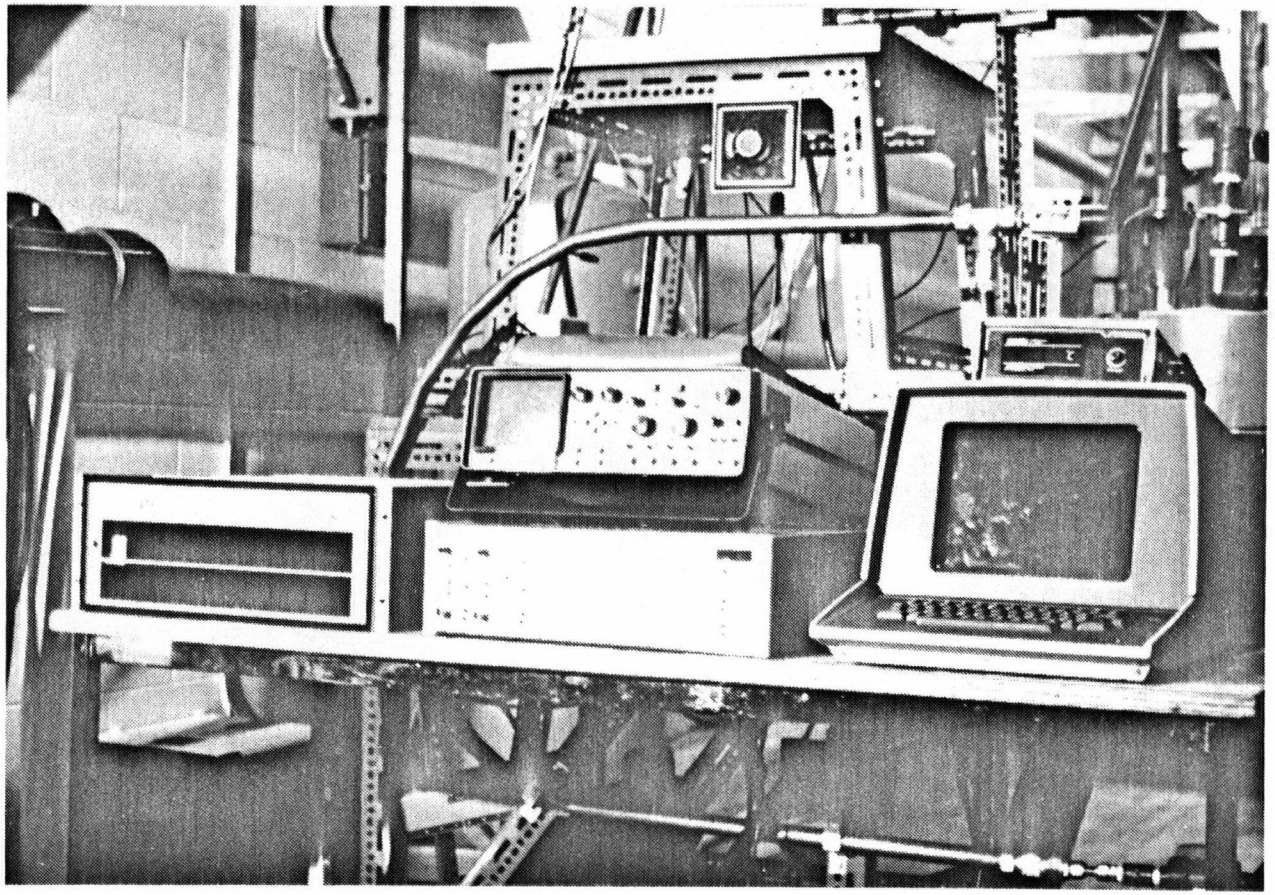

Fig. 2.2 Photograph of the Instrumentation

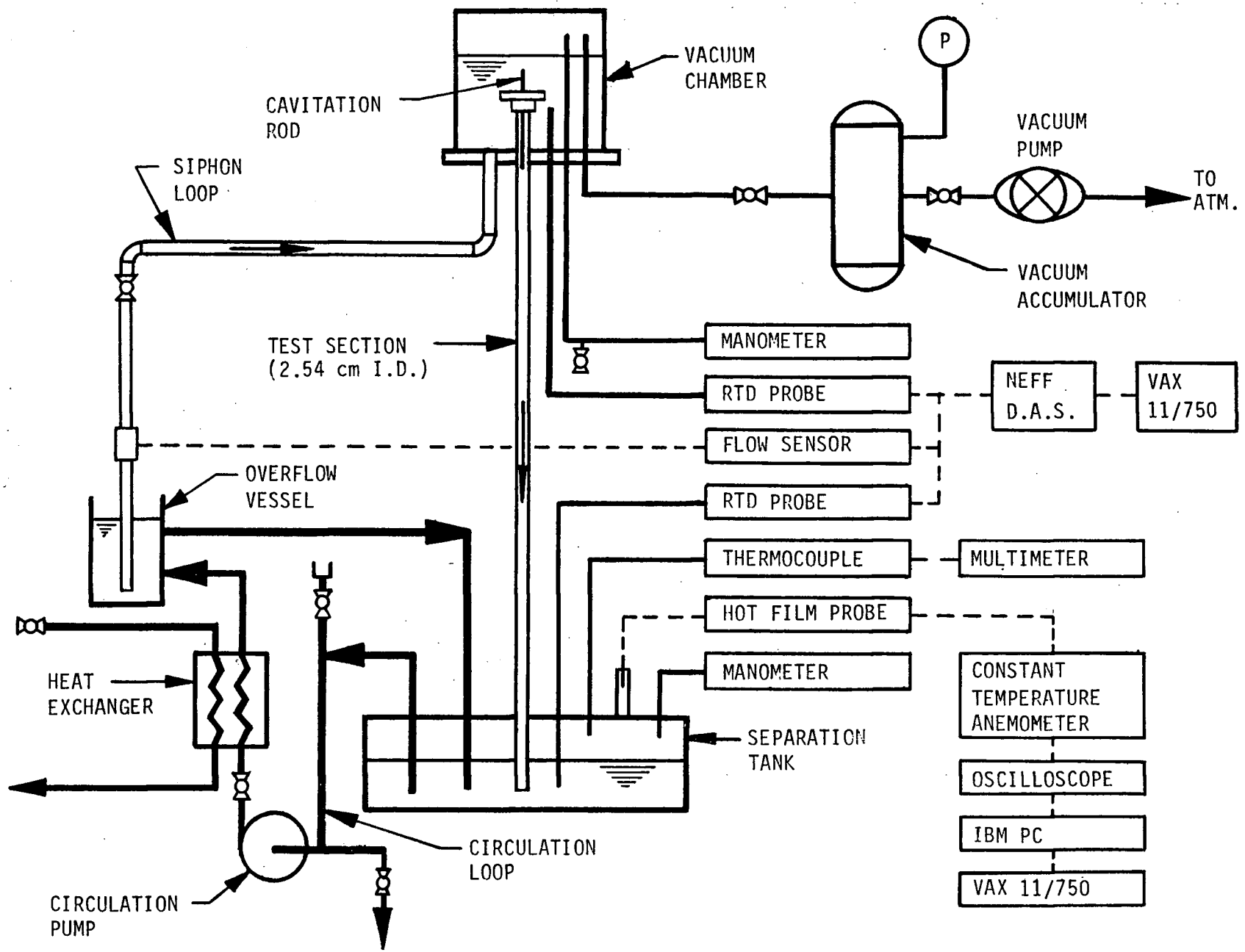

Fig. 2.3 Schematic of the Experimental Apparatus

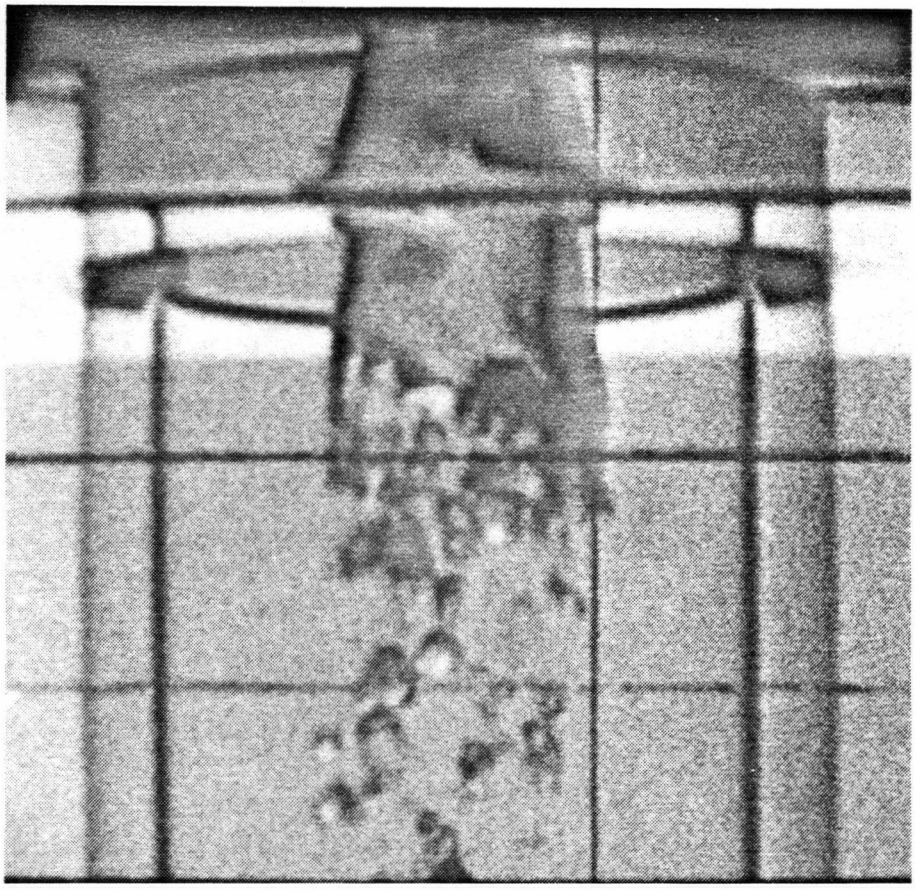

Fig. 2.4 Photograph of a Supercavitation Jet Formed at the Test Section Entrance

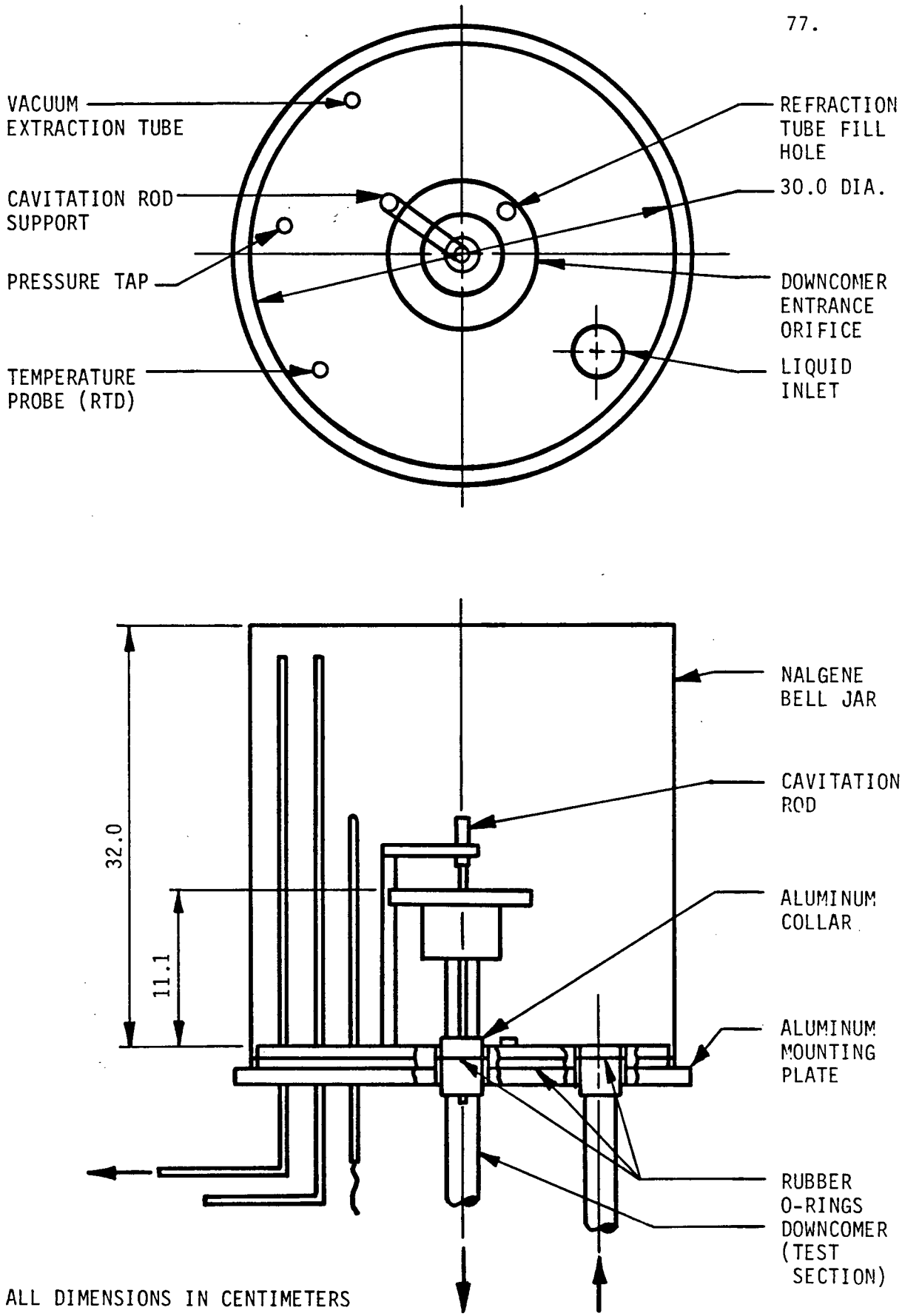

Fig. 2.5 Details of the Vacuum Chamber

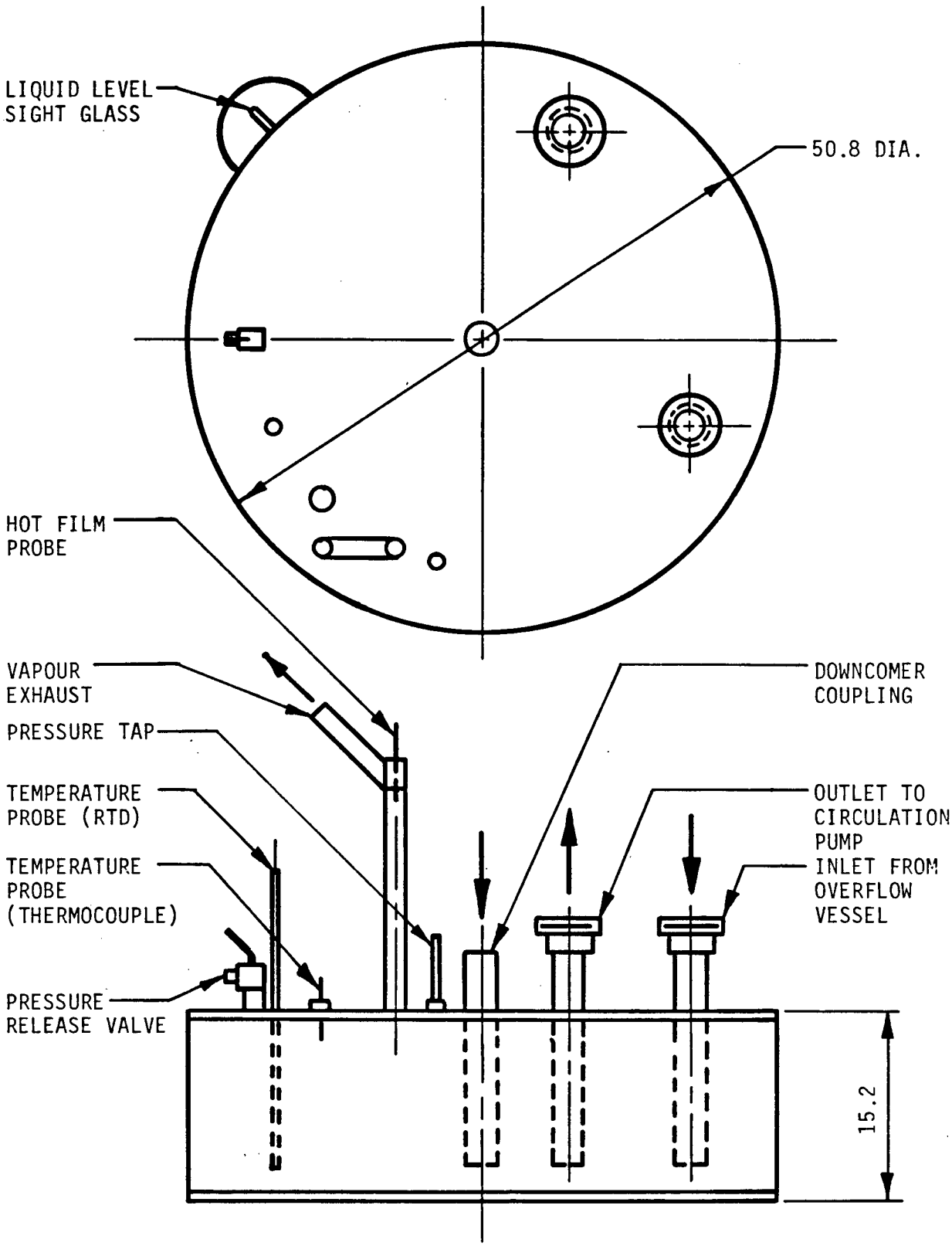

Fig. 2.6 Details of the Separation Tank

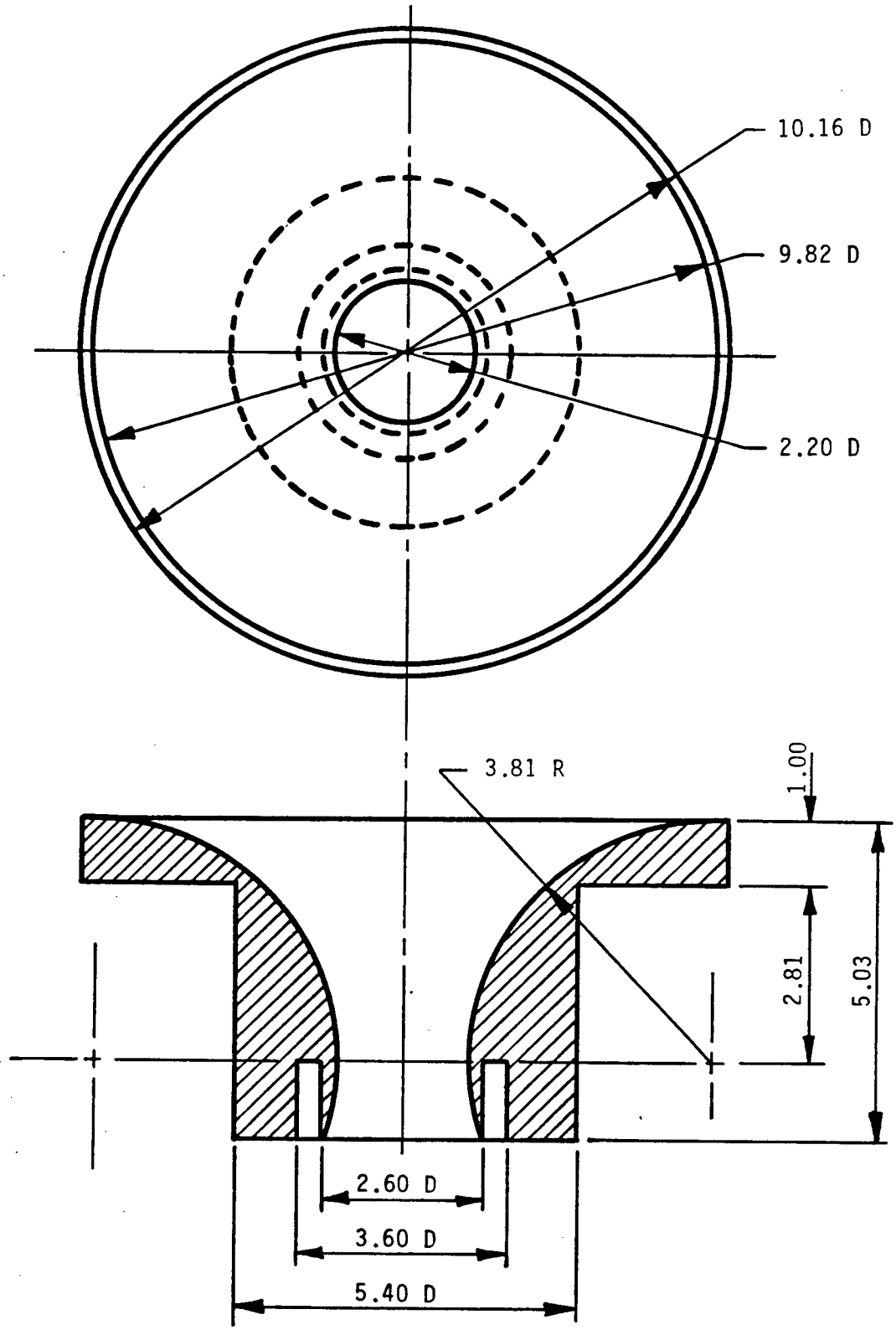

ALL DIMENSIONS IN CENTIMETERS
MATERIAL : ALUMINUM

Fig. 2.7 Details of the Test Section Inlet Orifice

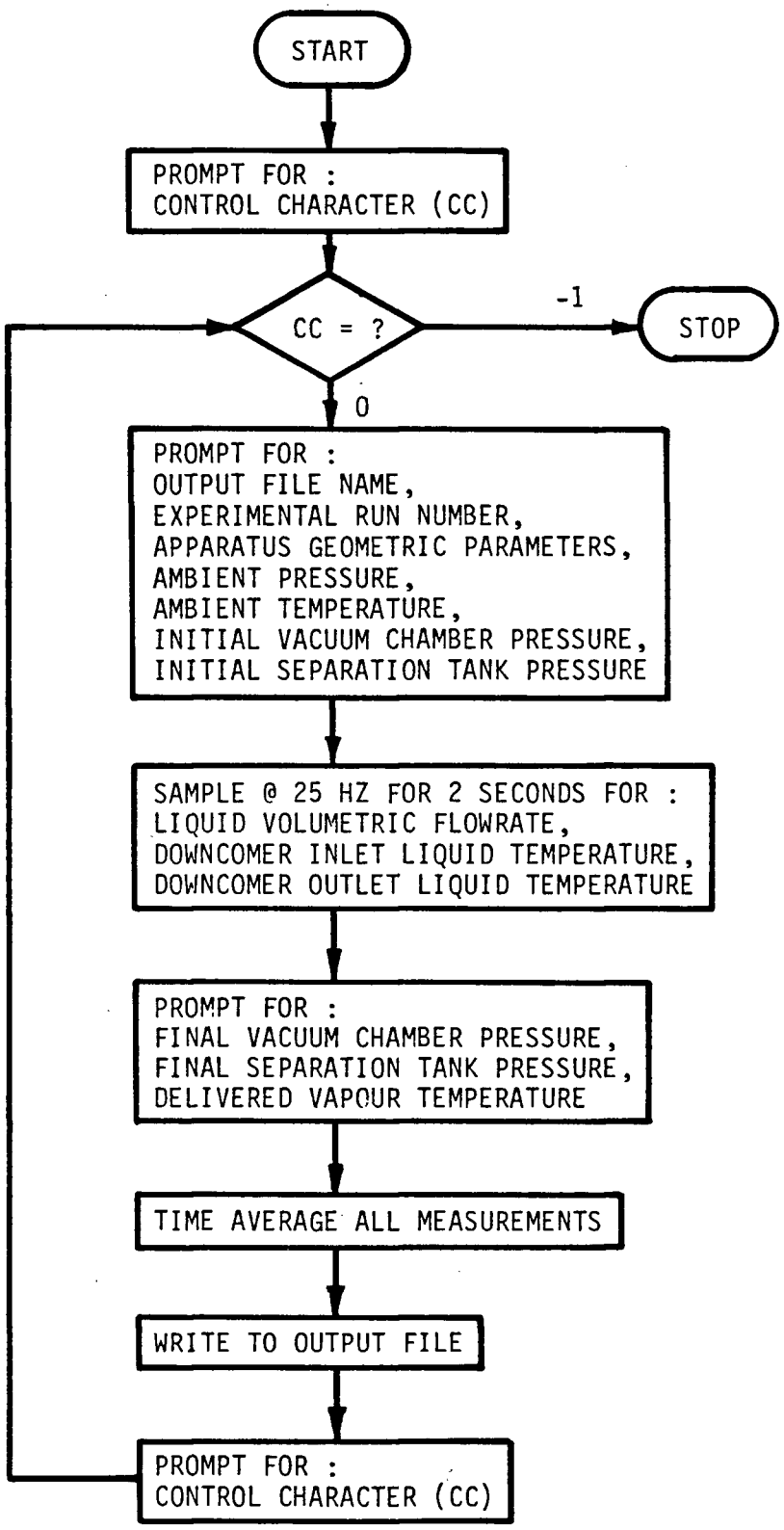

Fig. 2.8 Flowchart of the Data Acquisition Program

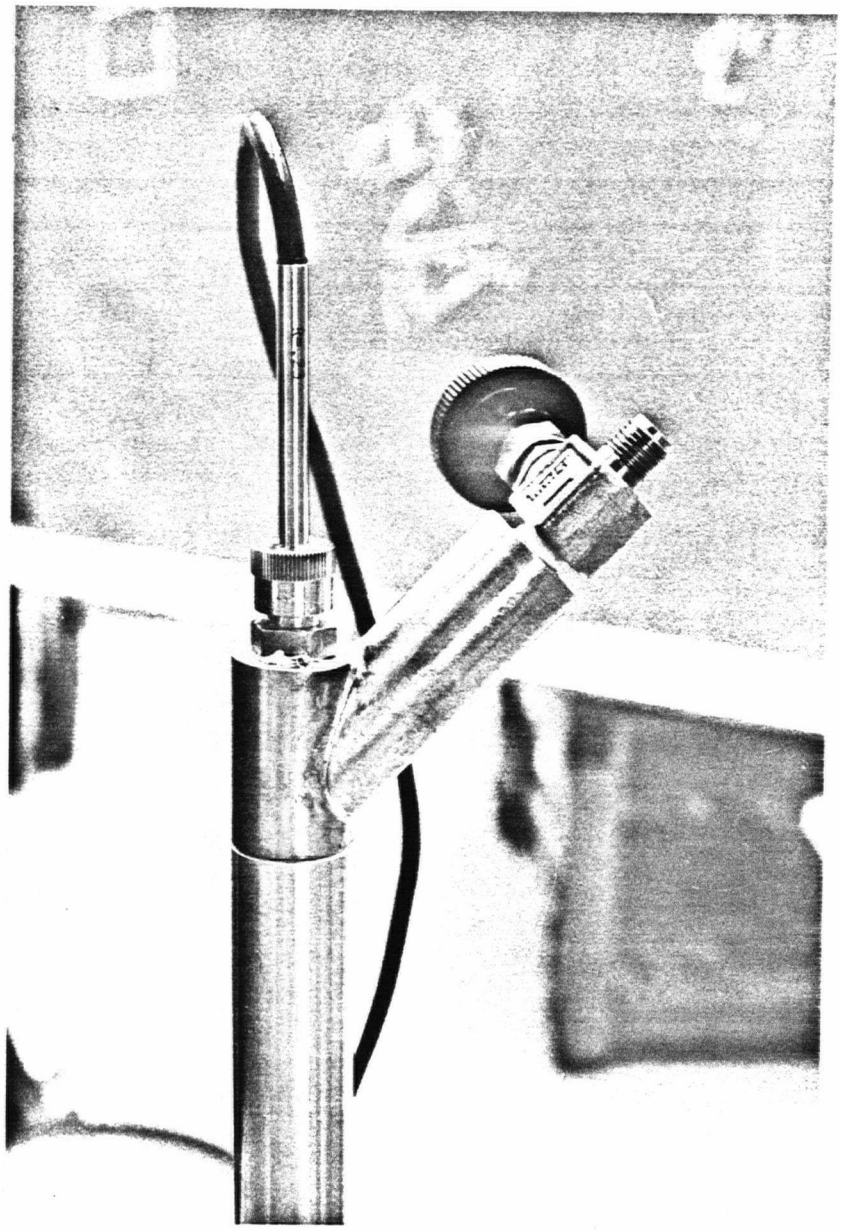

Fig. 2.9 Photograph of the Hot Film Probe Position in the Vapour Exhaust Tube

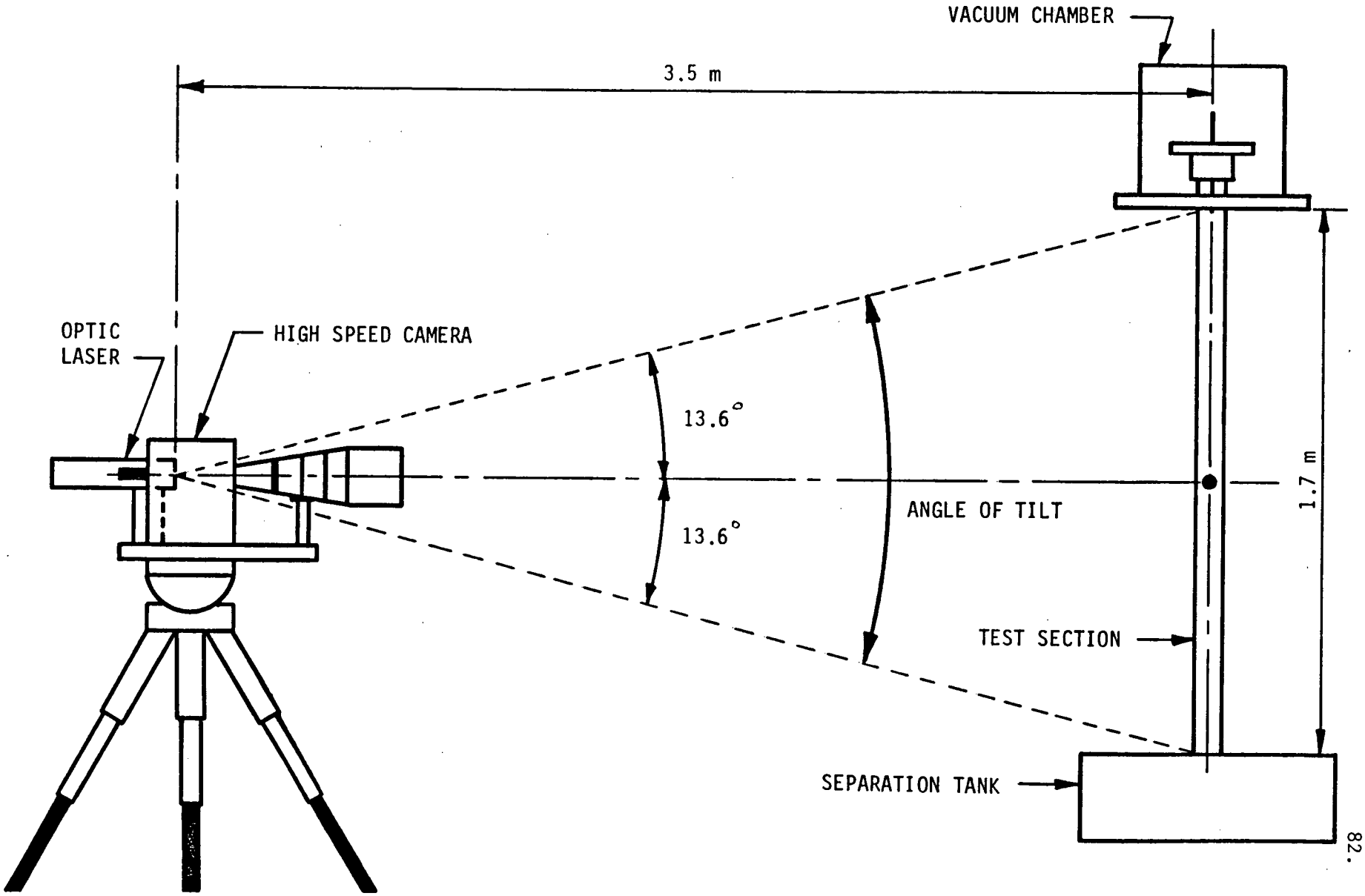

Fig. 2.10 Schematic of the Bubble Photography Equipment Arrangement

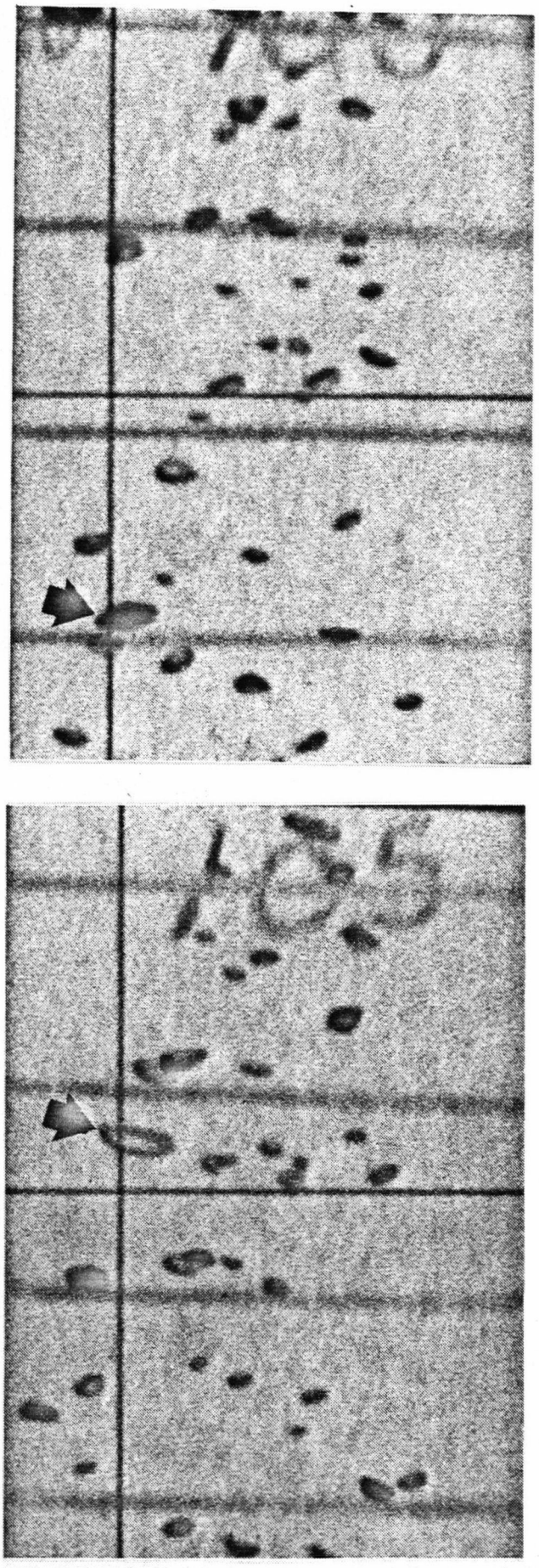

Fig. 4.1 Partial Film Sequence of a Vapour Bubble During Hydraulic Compression

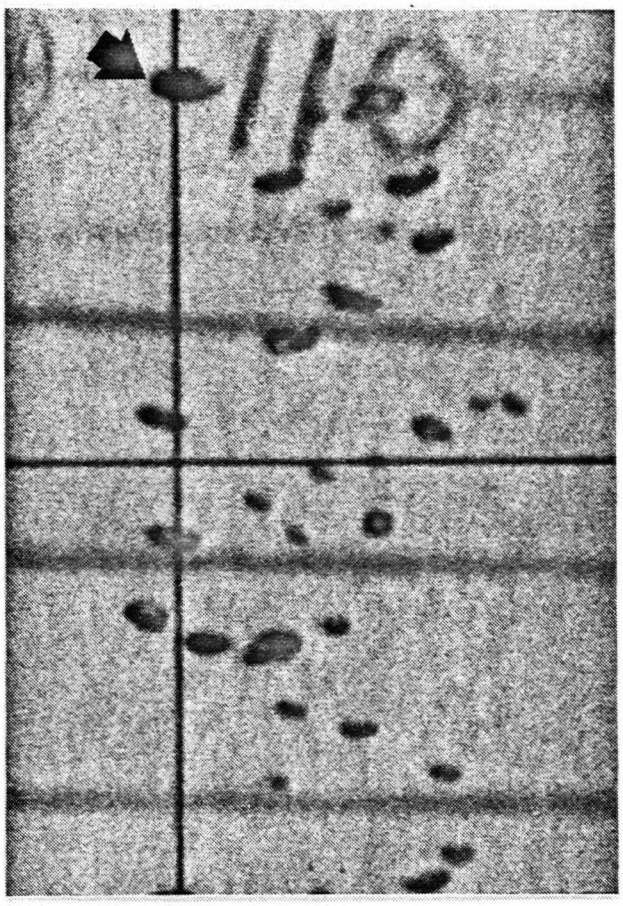

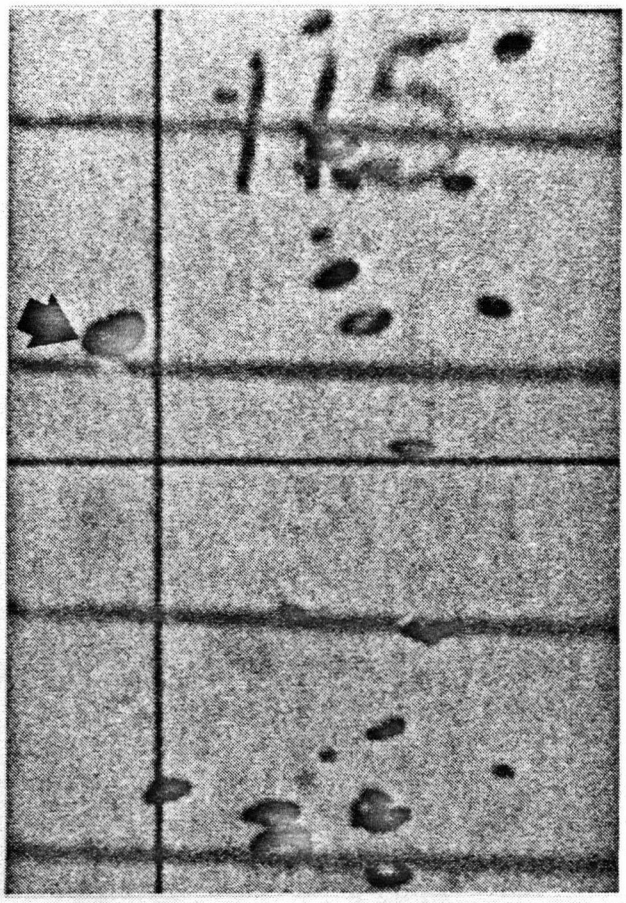

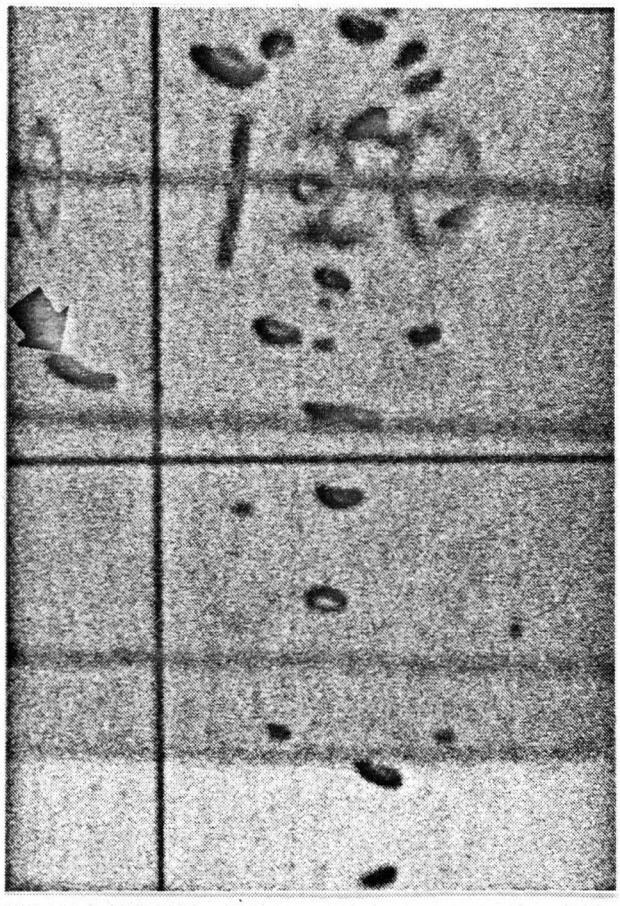

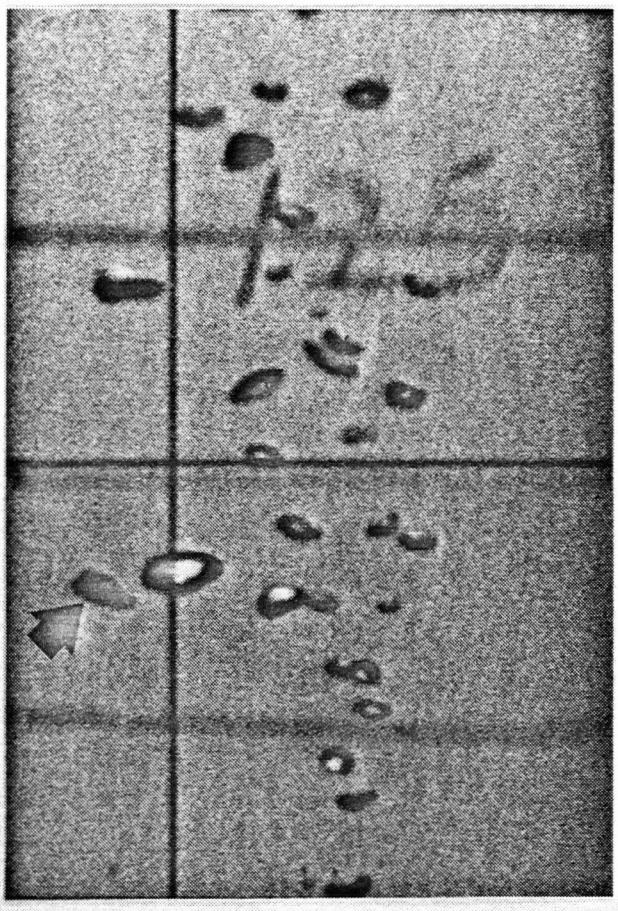

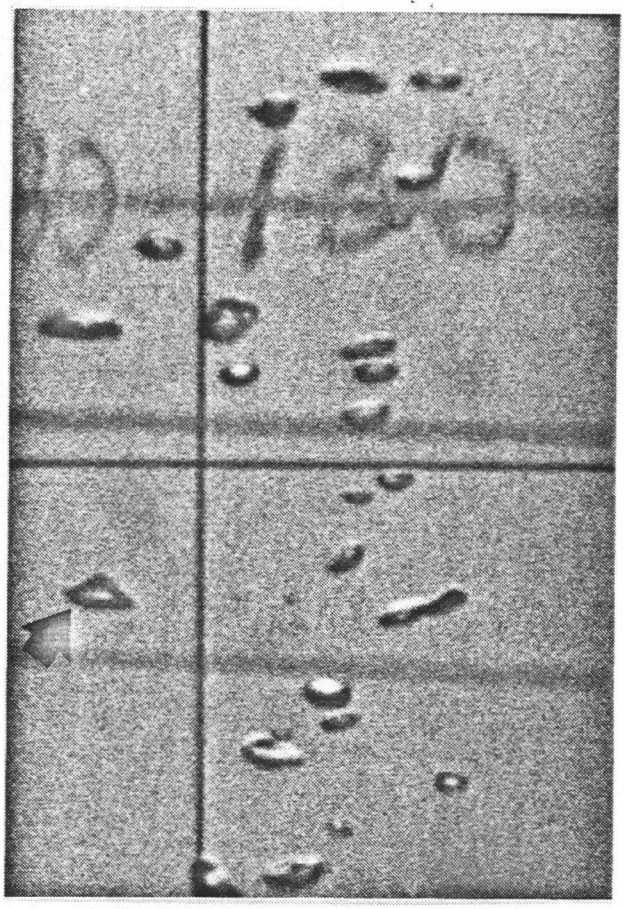

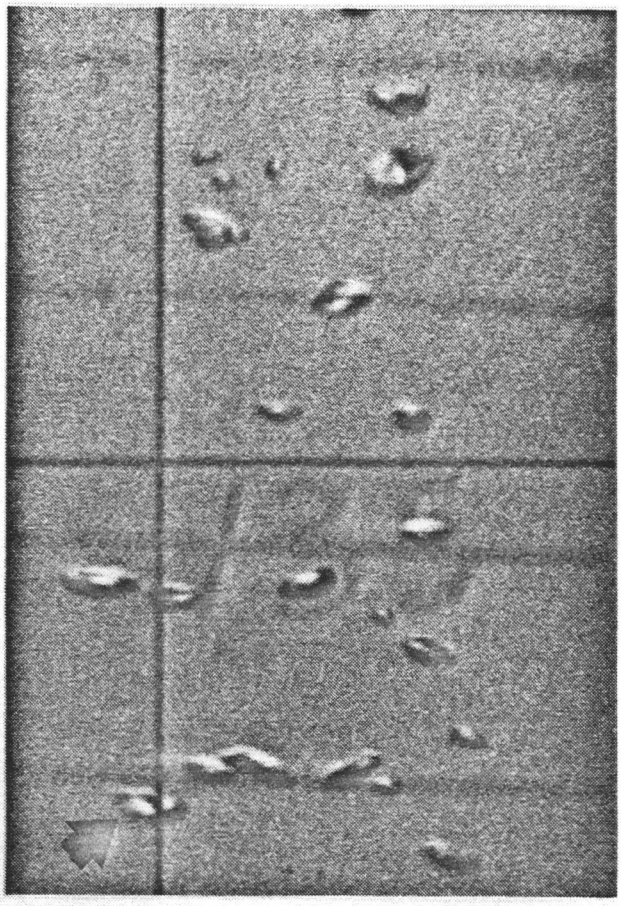

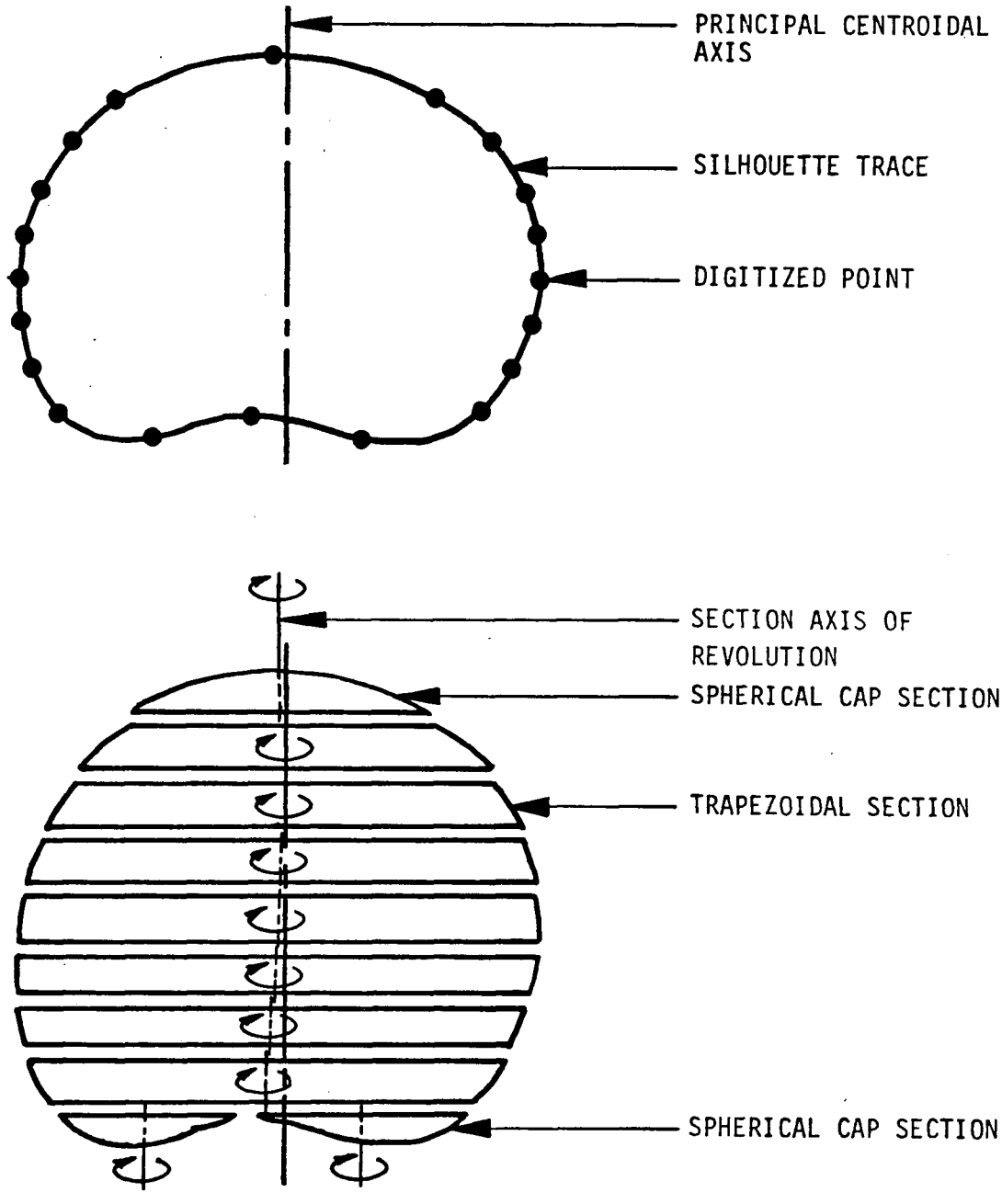

Fig. 4.2 Schematic of the Numerical Procedure for Estimating Bubble Surface Area and Volume

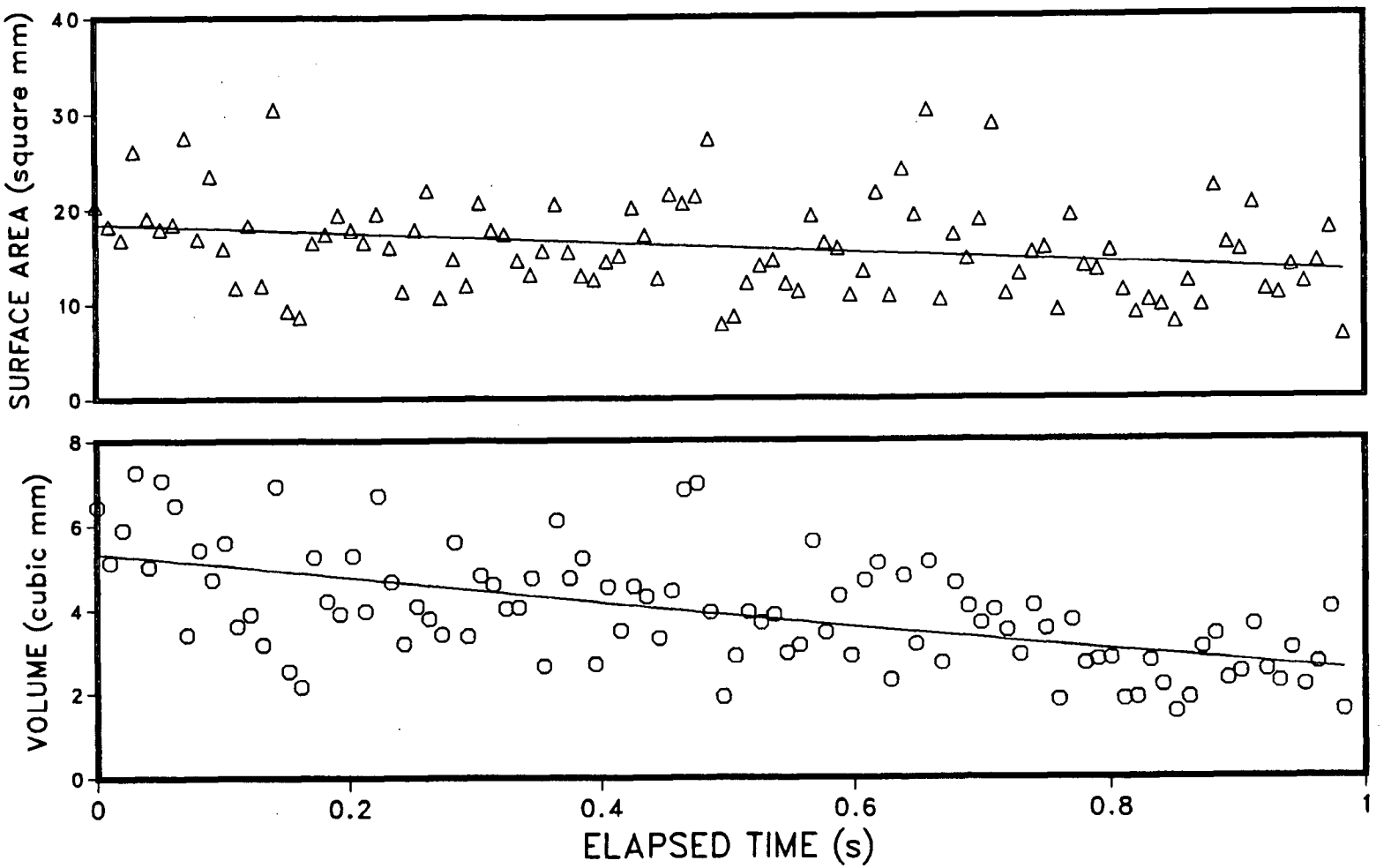

Fig. 4.3 Variation of the Surface Area and Volume with Time: Bubble 311

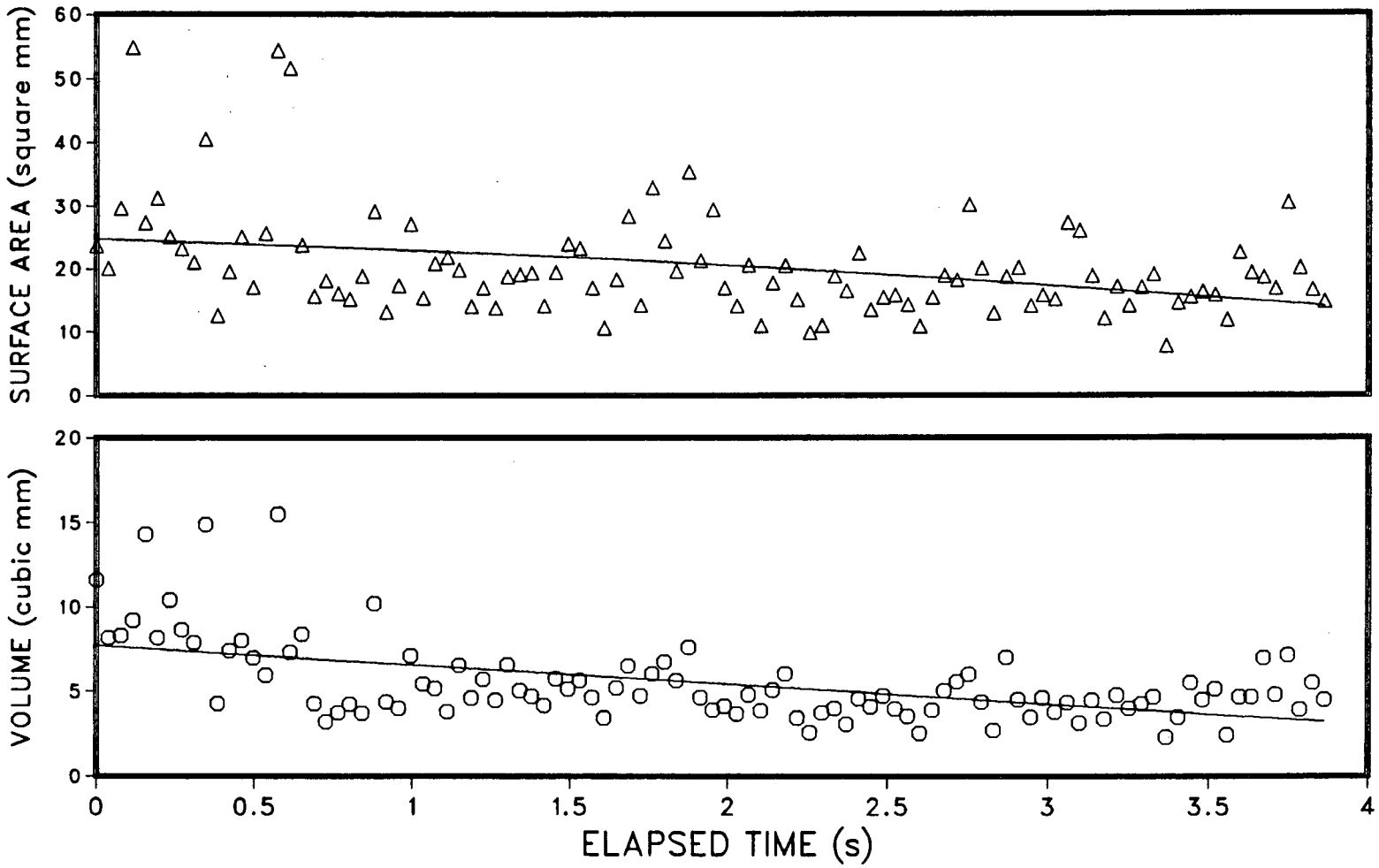

Fig. 4.4 Variation of the Surface Area and Volume with Time: Bubble 613

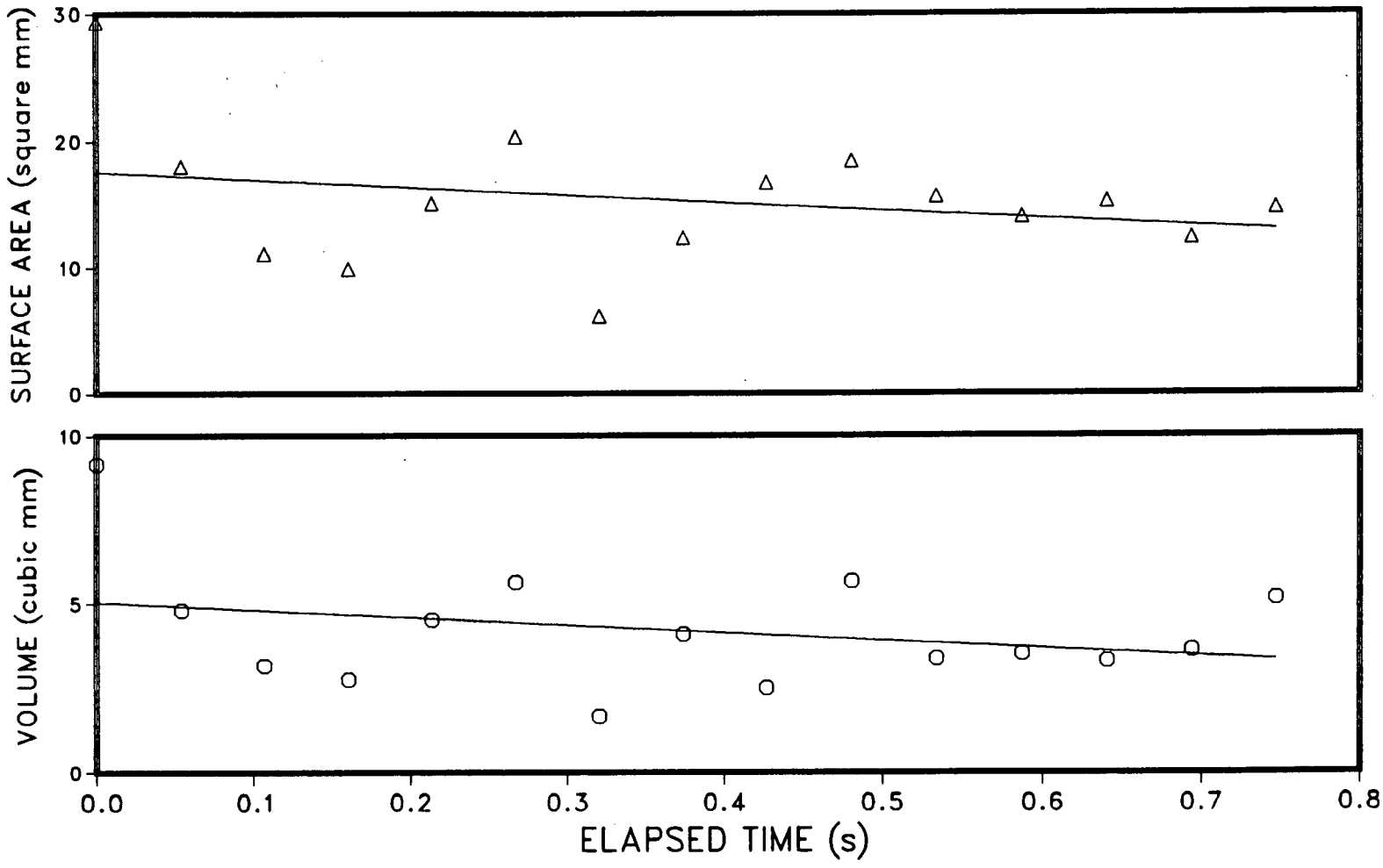

Fig. 4.5 Variation of the Surface Area and Volume with Time: Bubble 621

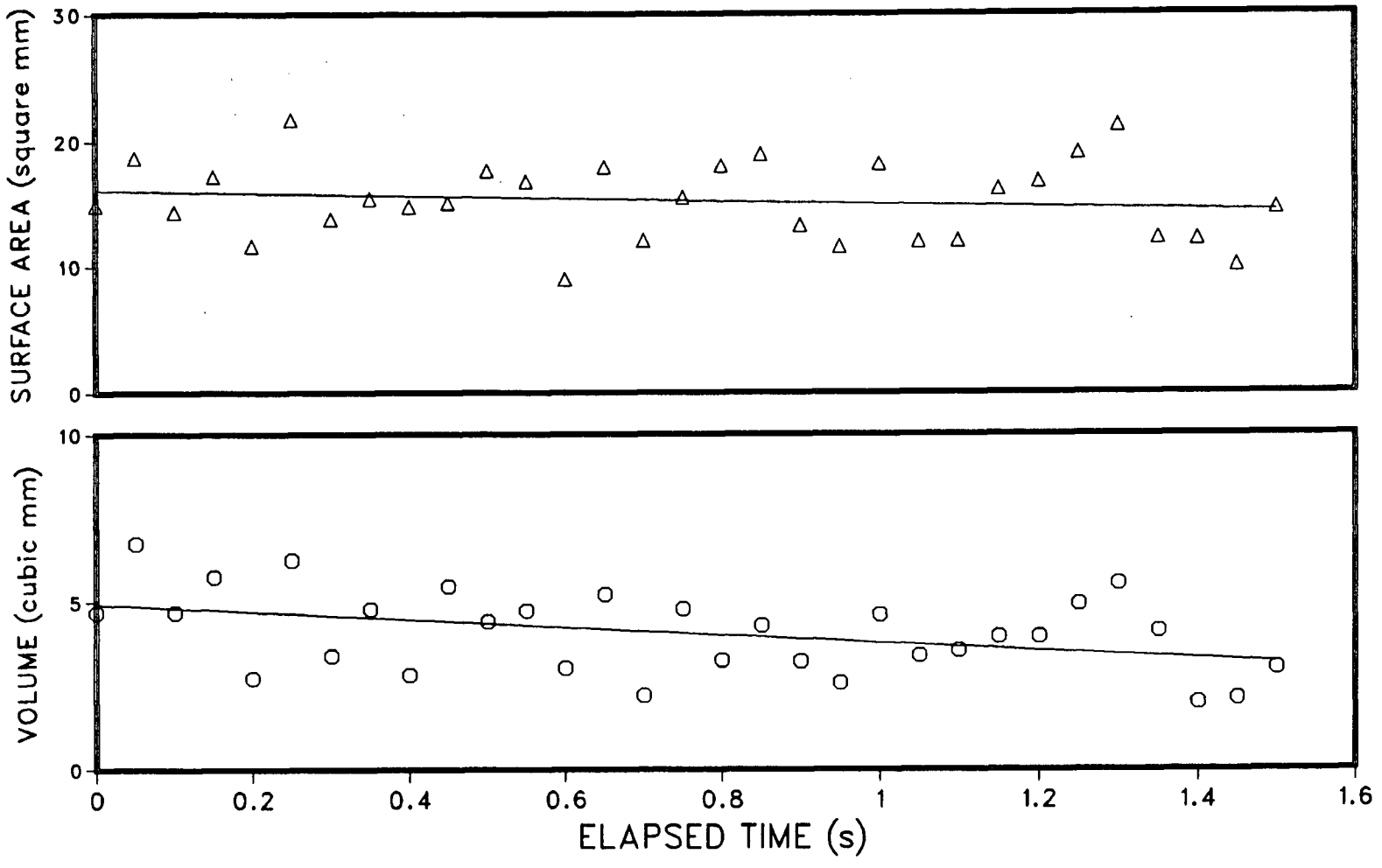

Fig. 4.6 Variation of the Surface Area and Volume with Time: Bubble 622

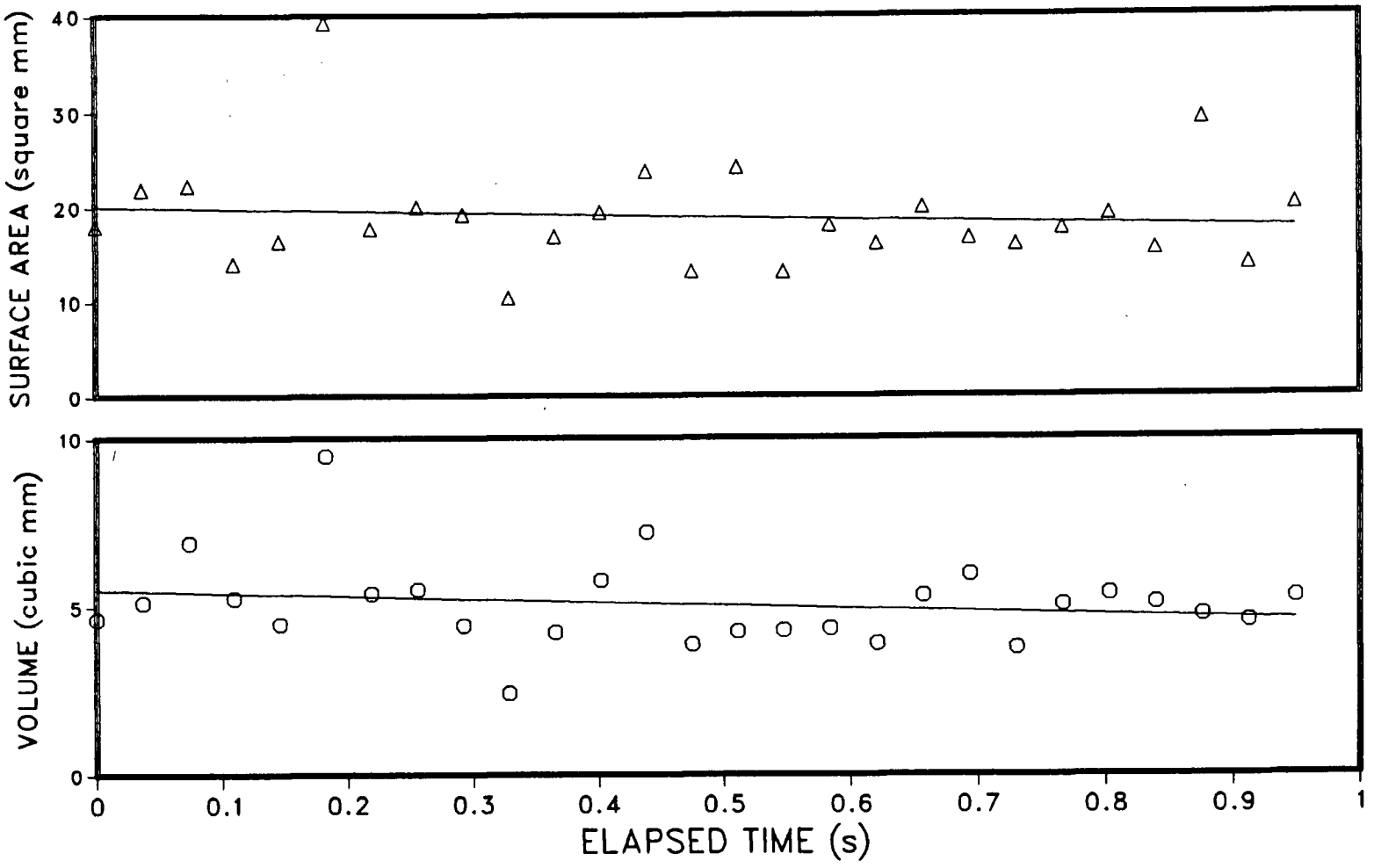

Fig. 4.7 Variation of the Surface Area and Volume with Time: Bubble 624

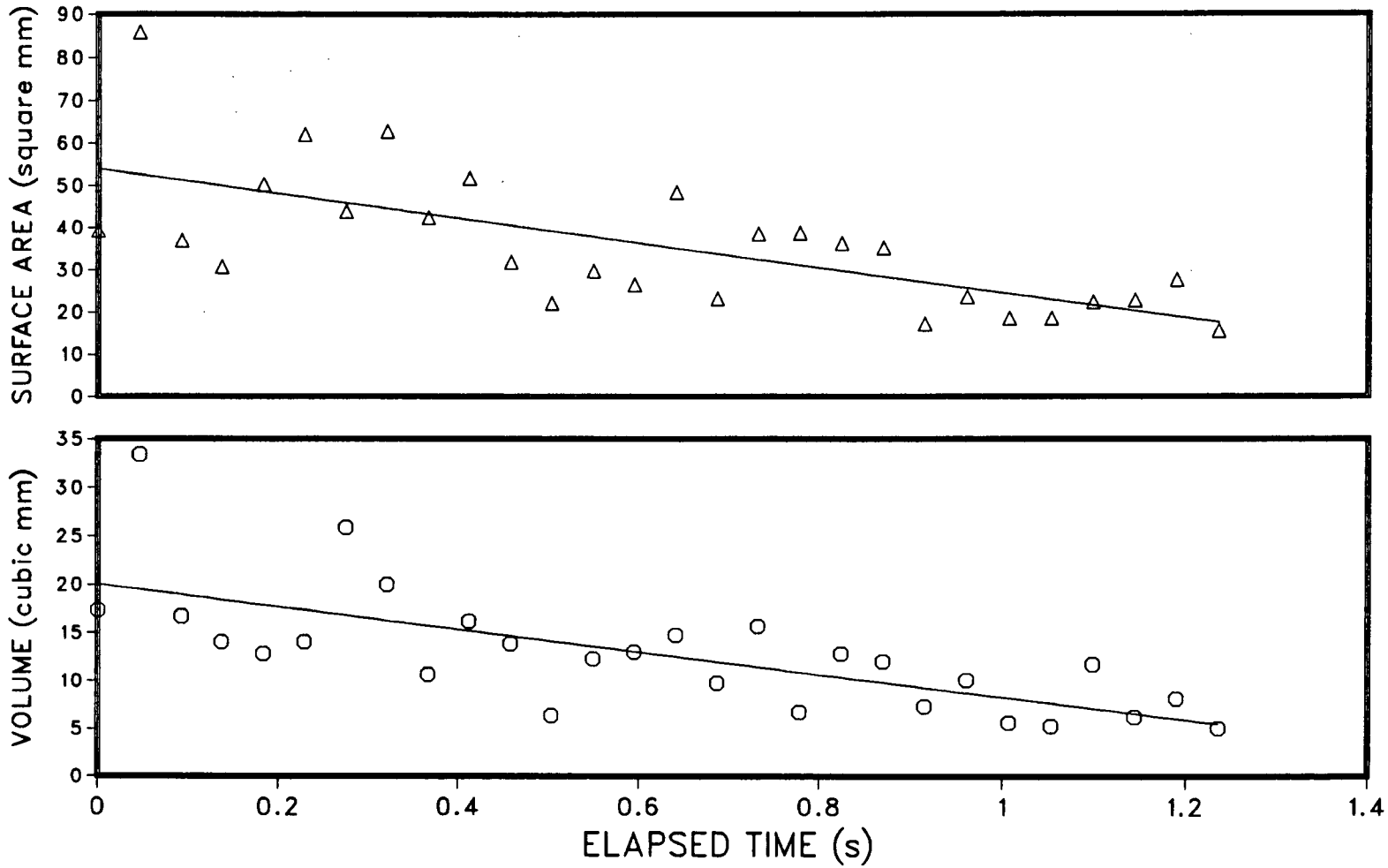

Fig. 4.8 Variation of the Surface Area and Volume with Time: Bubble 721

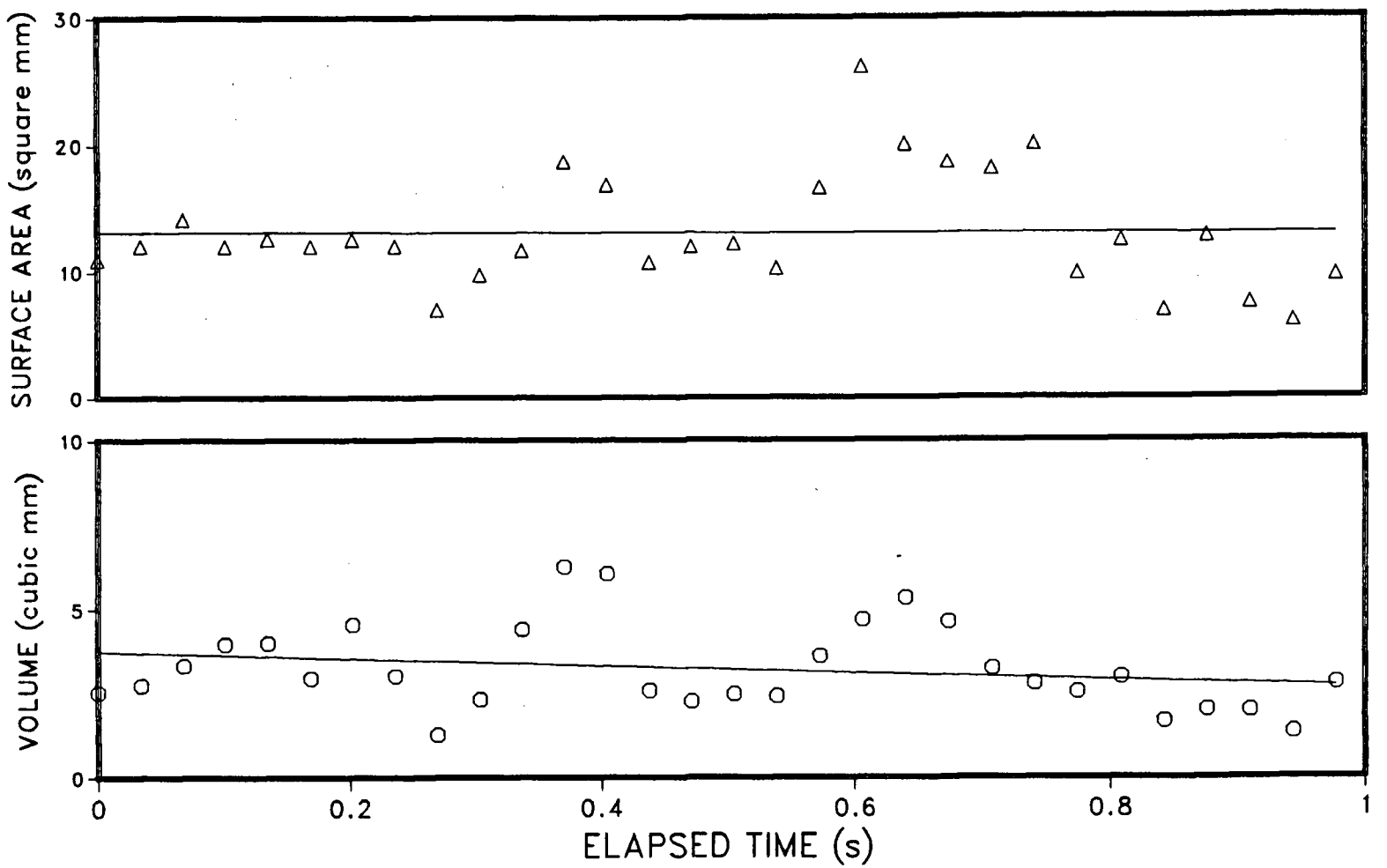

Fig. 4.9 Variation of the Surface Area and Volume with Time: Bubble 722

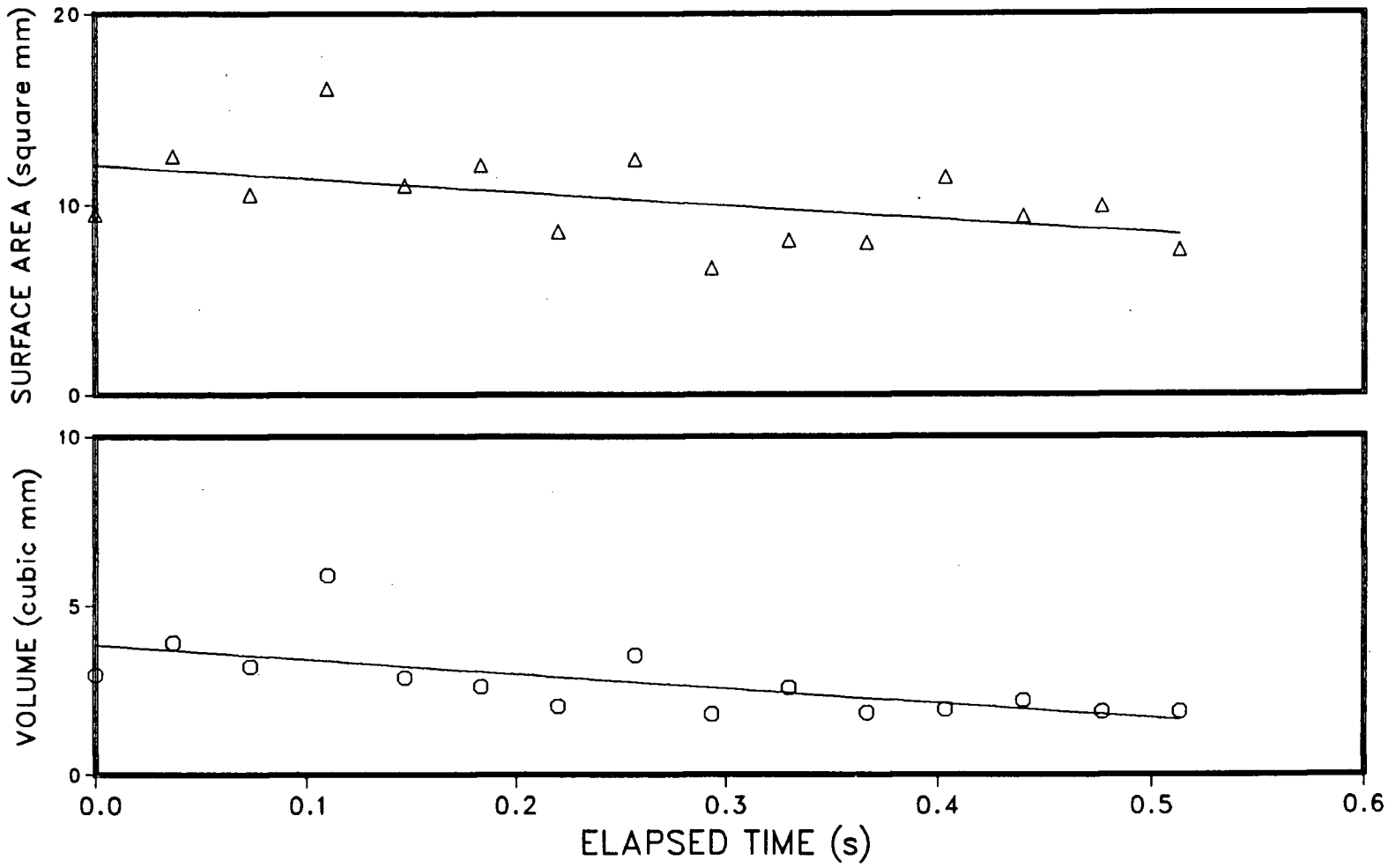

Fig. 4.10 Variation of the Surface Area and Volume with Time: Bubble 731

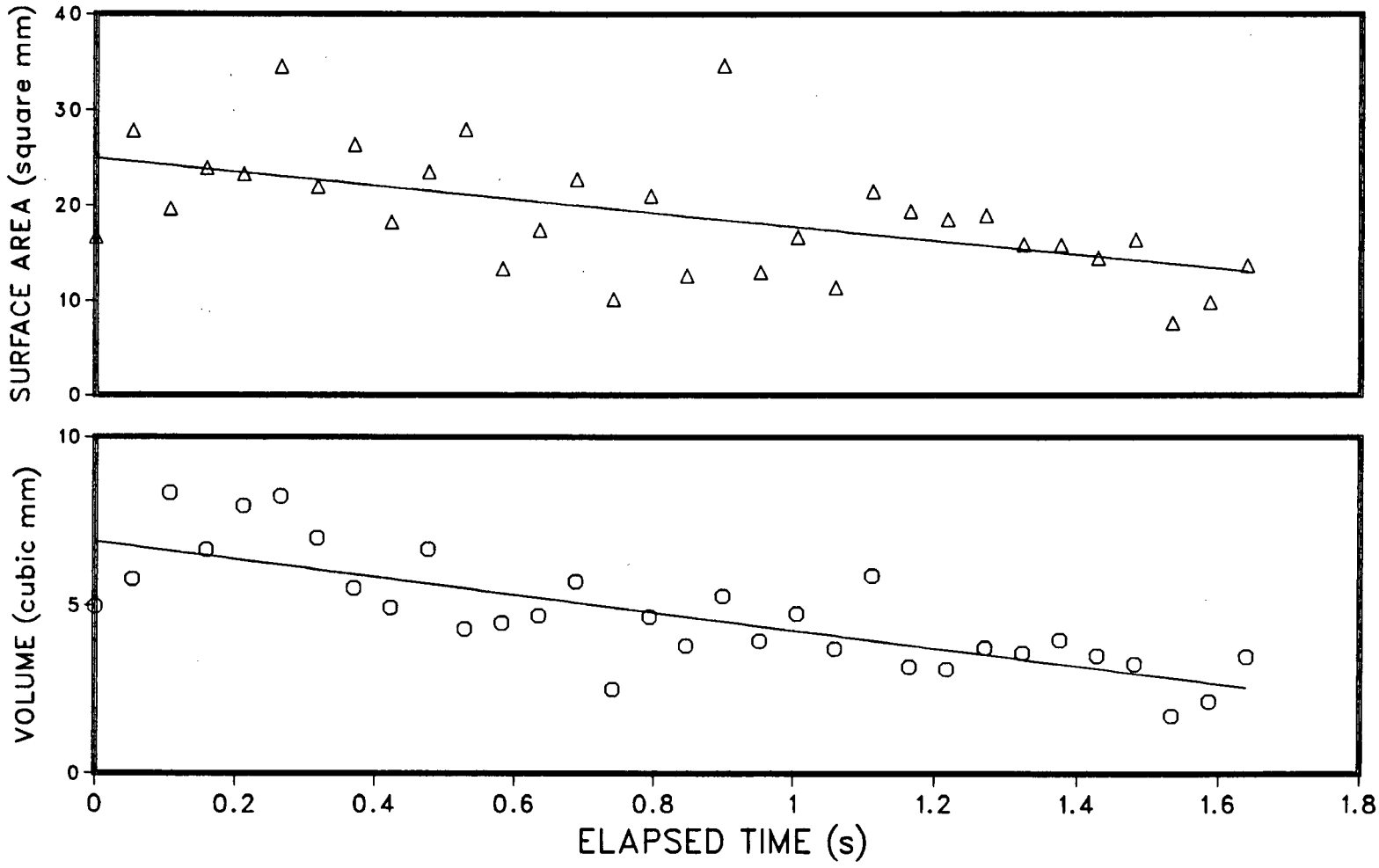

Fig. 4.11 Variation of the Surface Area and Volume with Time: Bubble 811

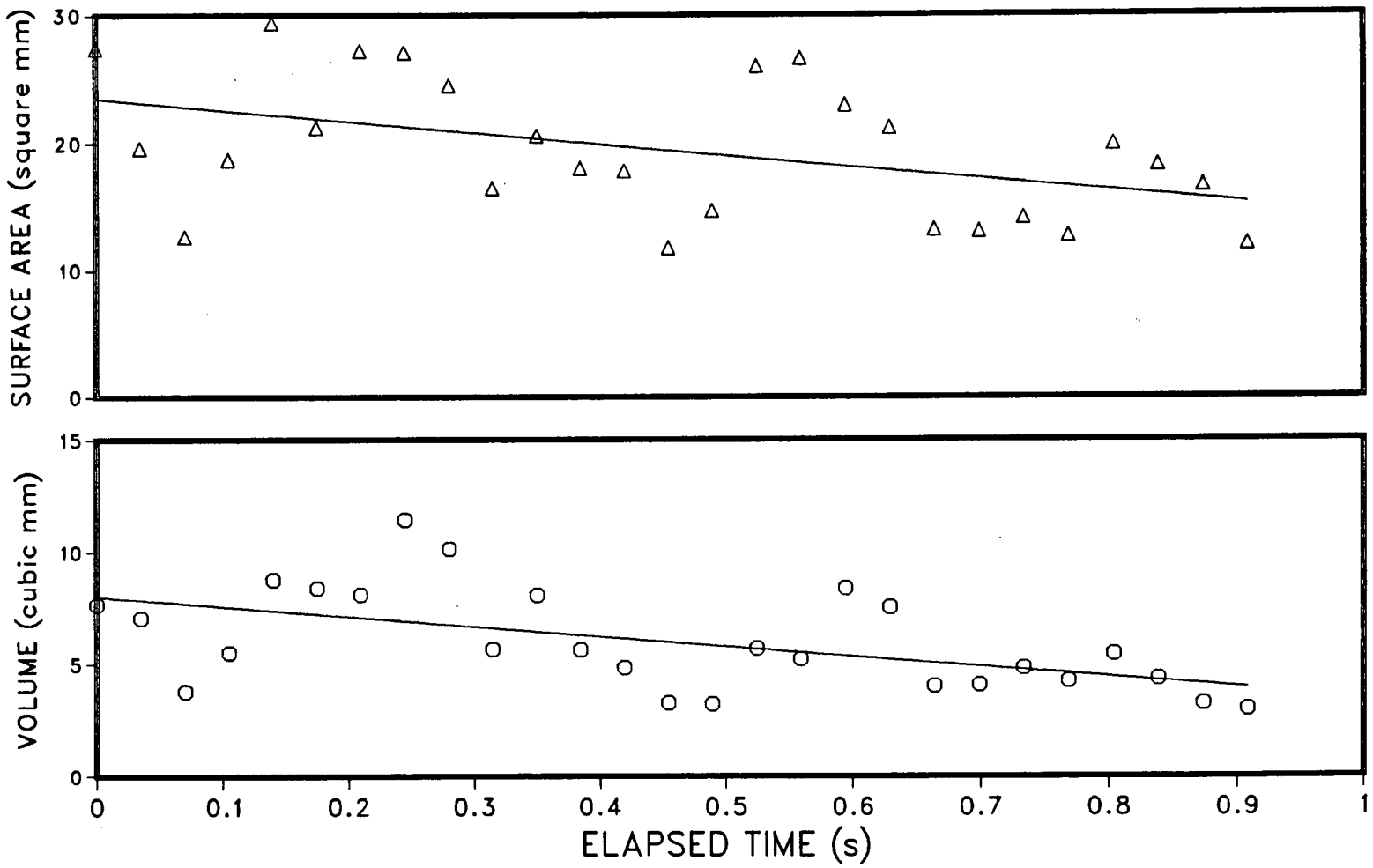

Fig. 4.12 Variation of the Surface Area and Volume with Time: Bubble 812

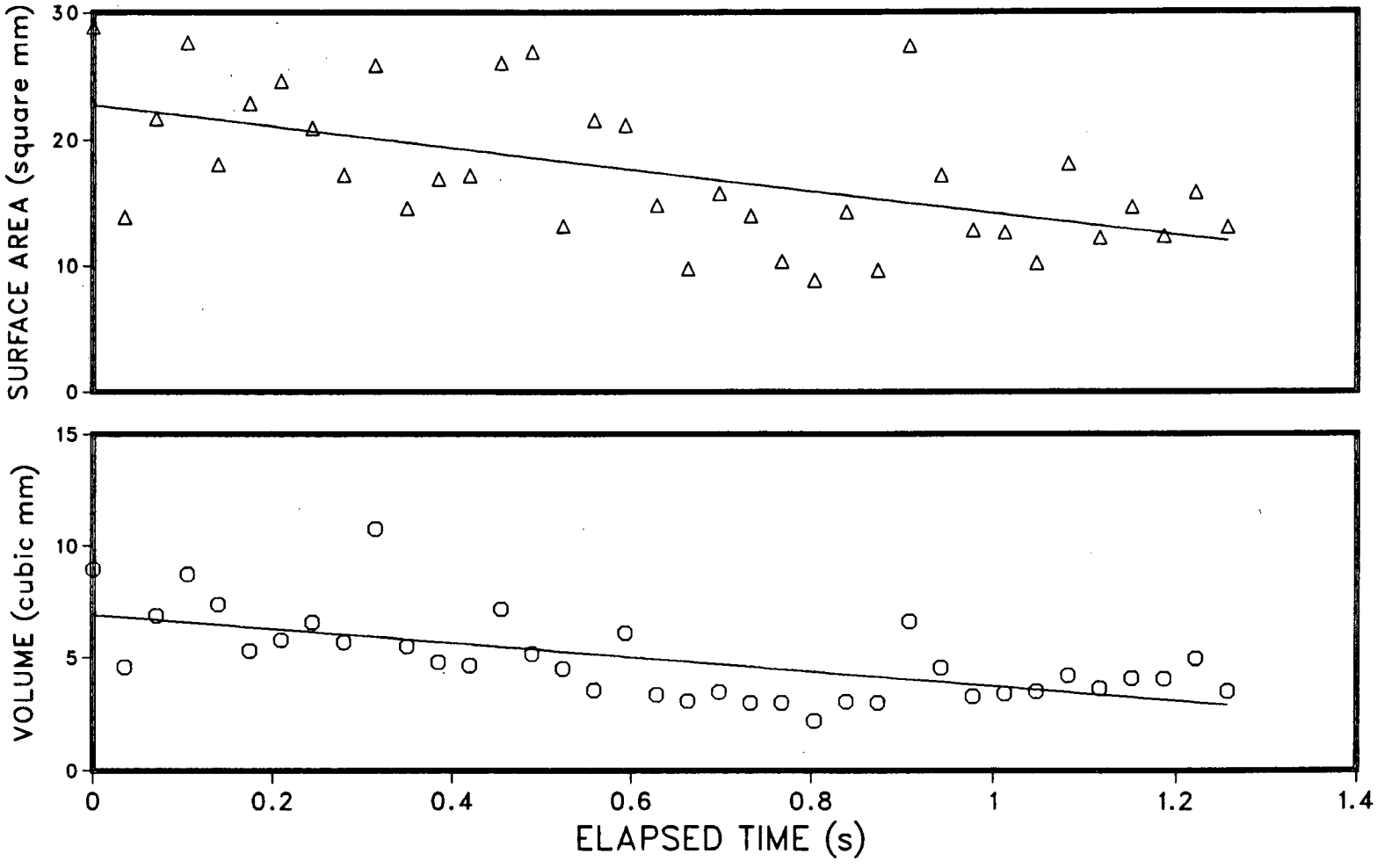

Fig. 4.13 Variation of the Surface Area and Volume with Time: Bubble 813

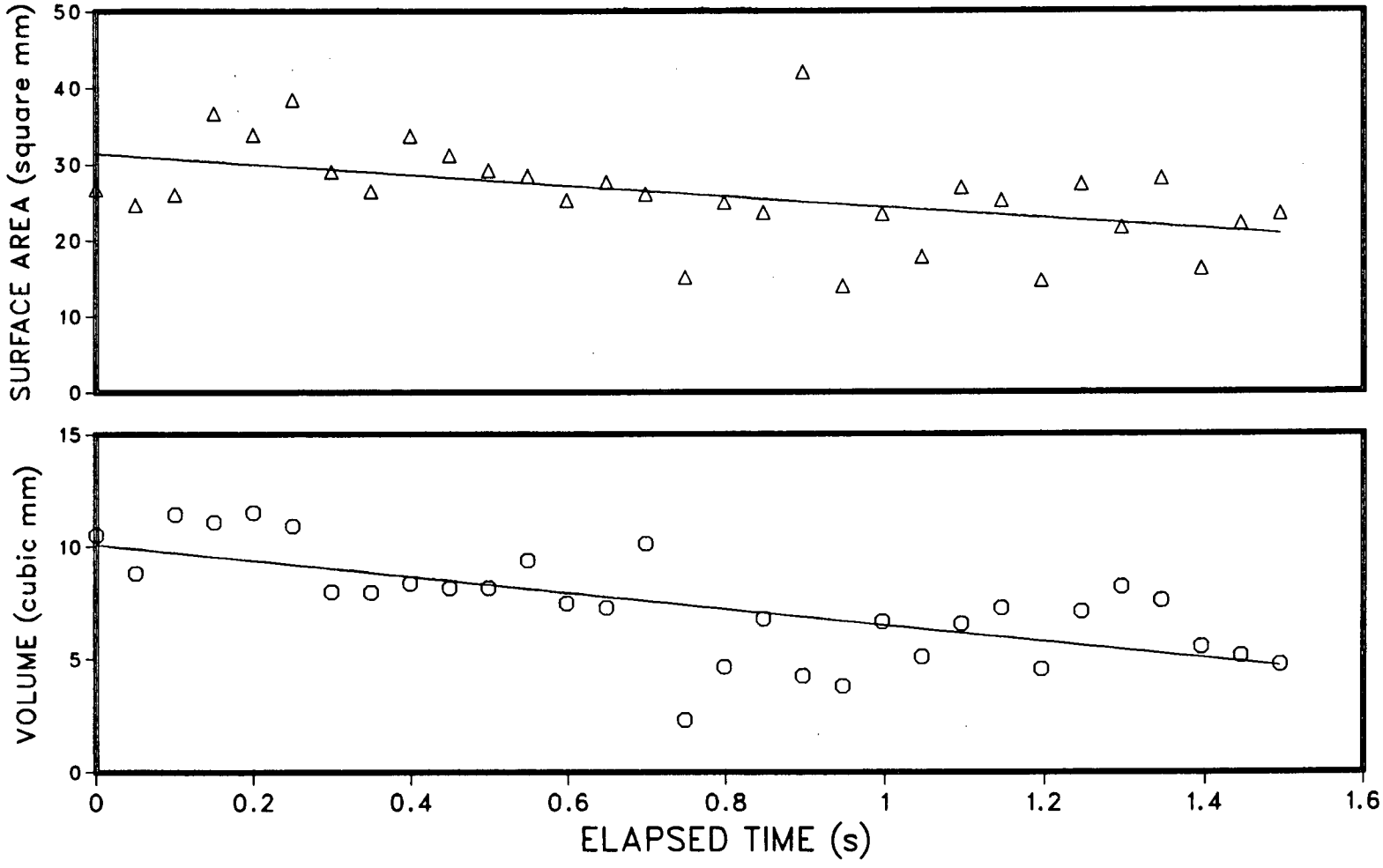

Fig. 4.14 Variation of the Surface Area and Volume with Time: Bubble 821

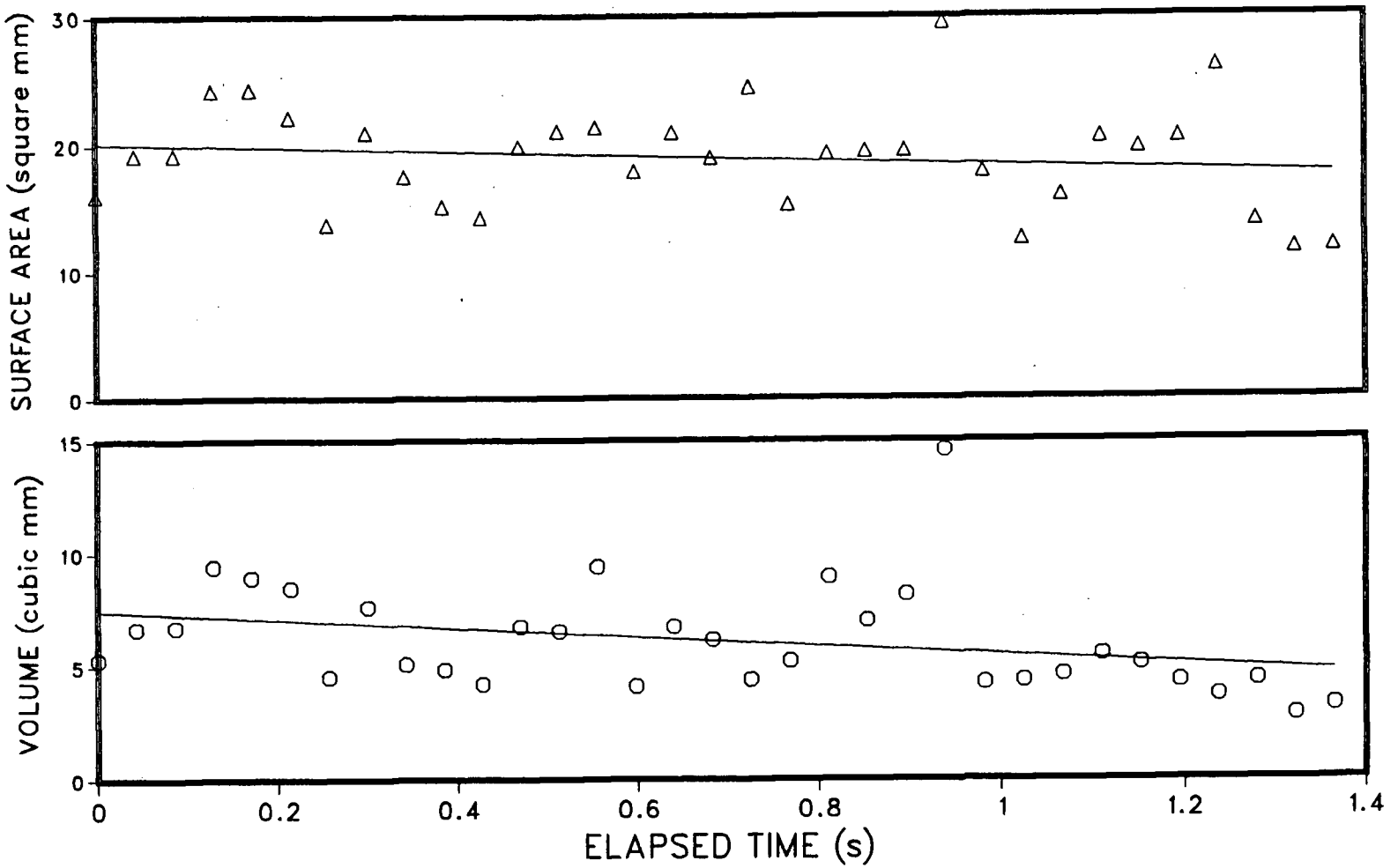

Fig. 4.15 Variation of the Surface Area and Volume with Time: Bubble 822

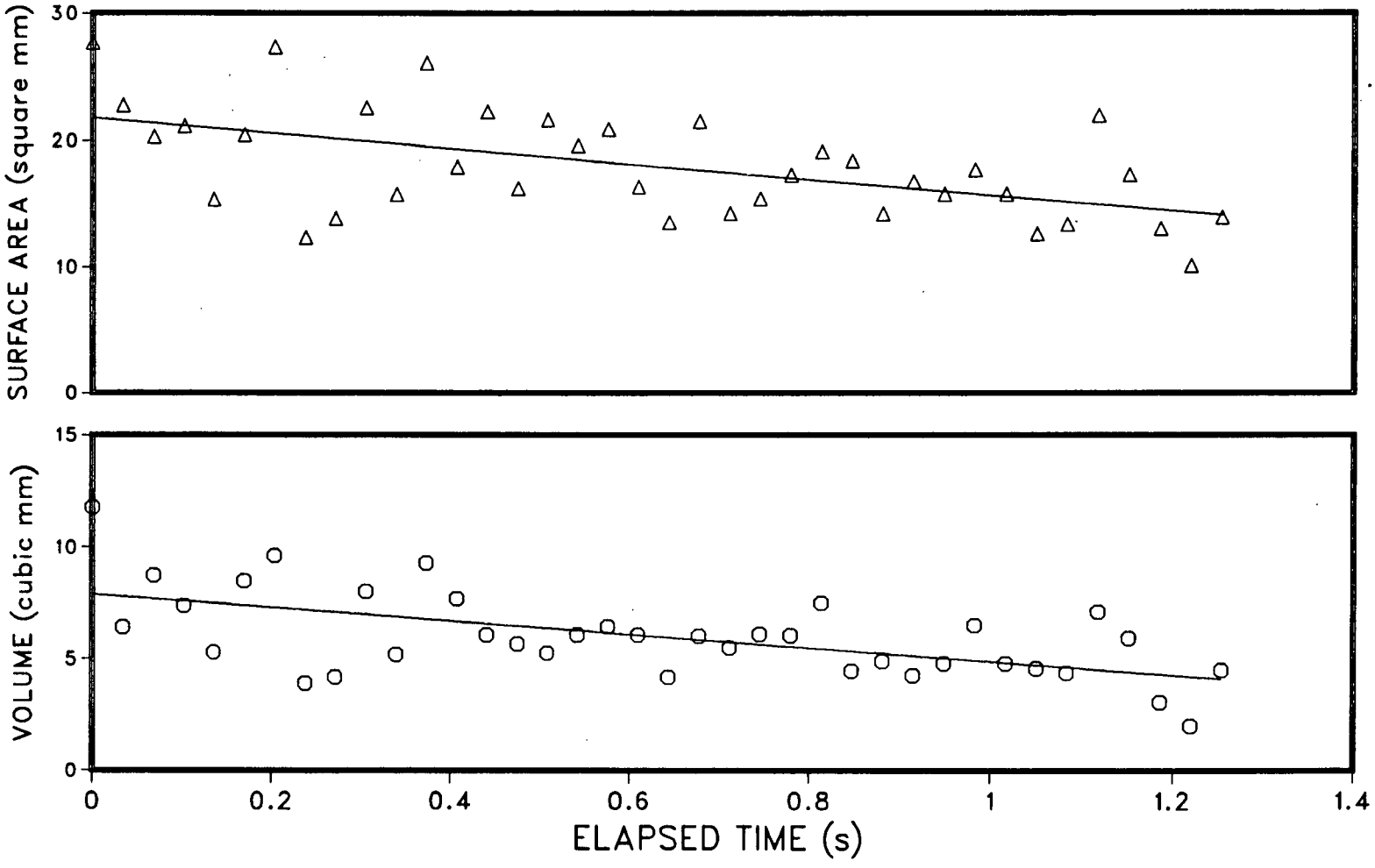

Fig. 4.16 Variation of the Surface Area and Volume with Time: Bubble 823

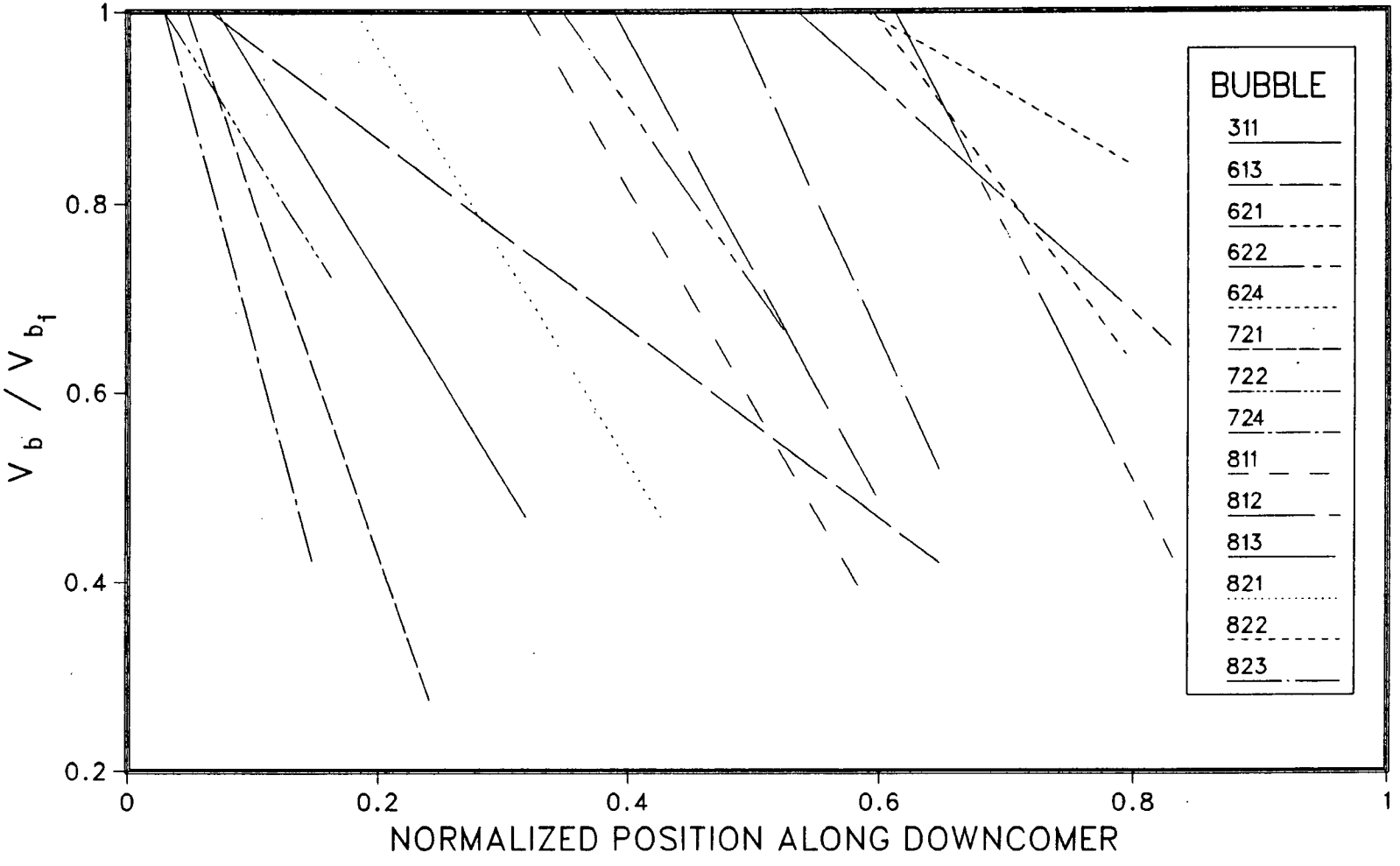

Fig. 5.1 Variation of the Volume with Normalized Position: All Bubbles

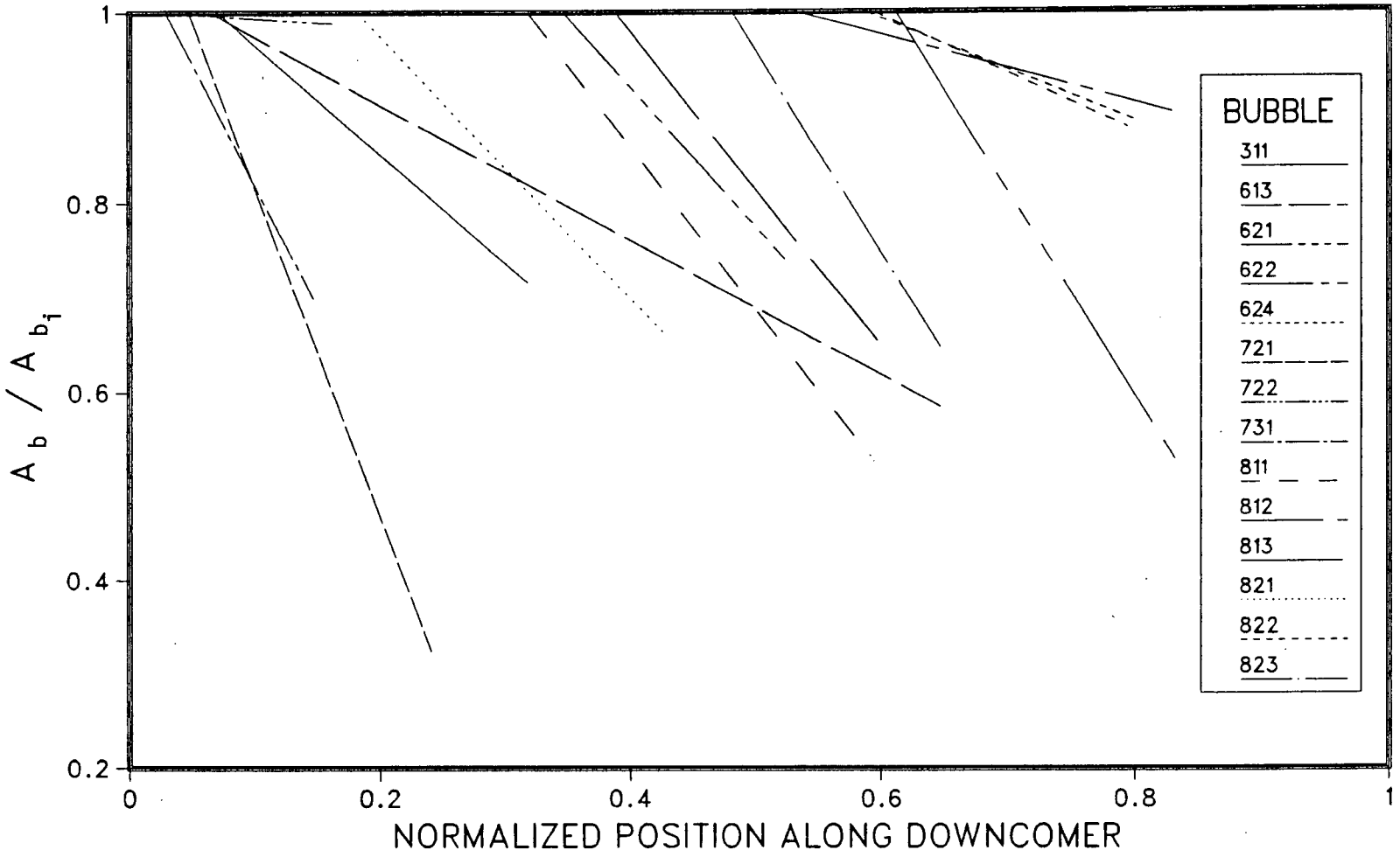

Fig. 5.2 Variation of the Surface Area with Normalized Position: All Bubbles

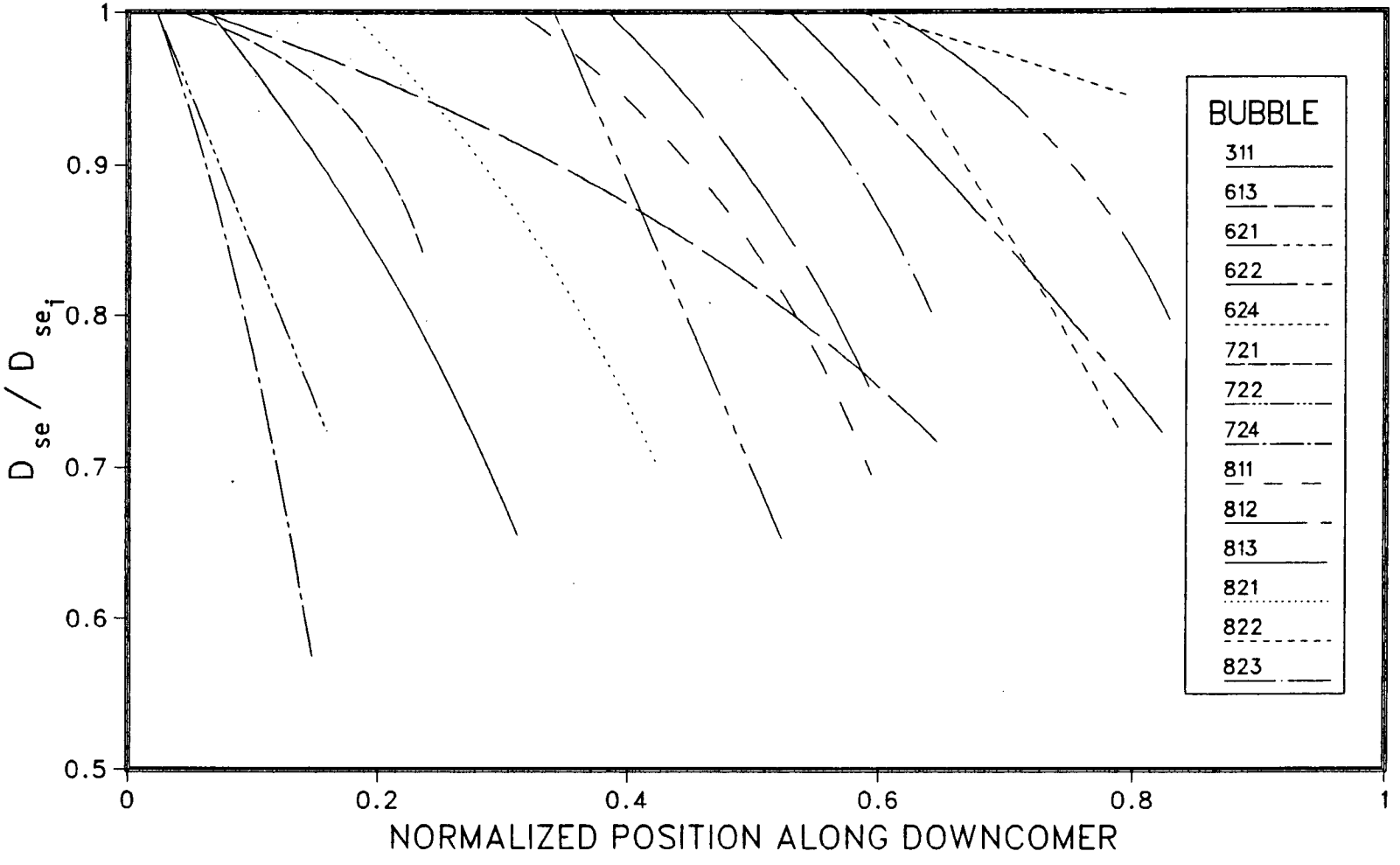

Fig. 5.3 Variation of the Equivalent Diameter with Normalized Position: All Bubbles

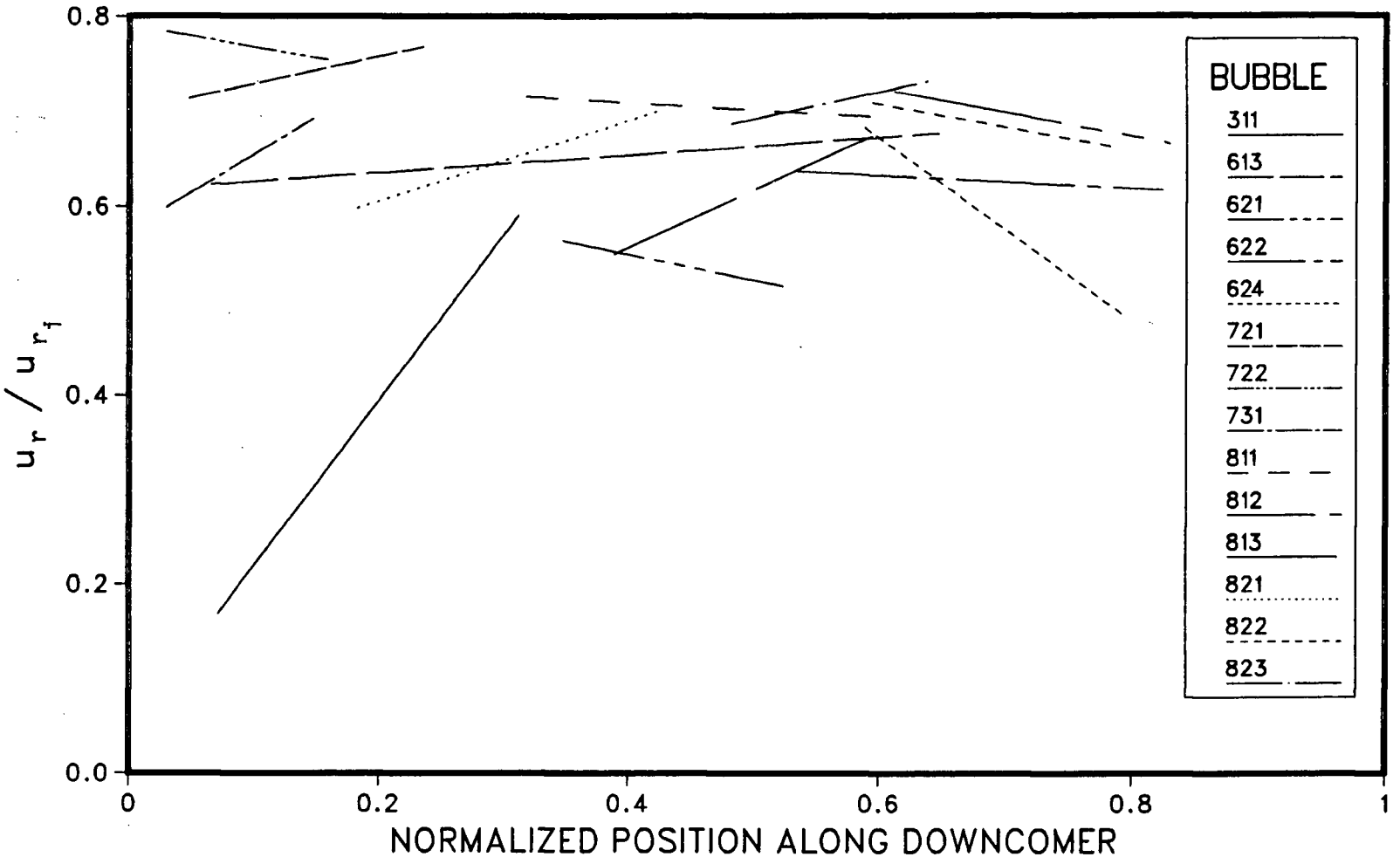

Fig. 5.4 Variation of the Nominal Relative Velocity with Normalized Position: All Bubbles

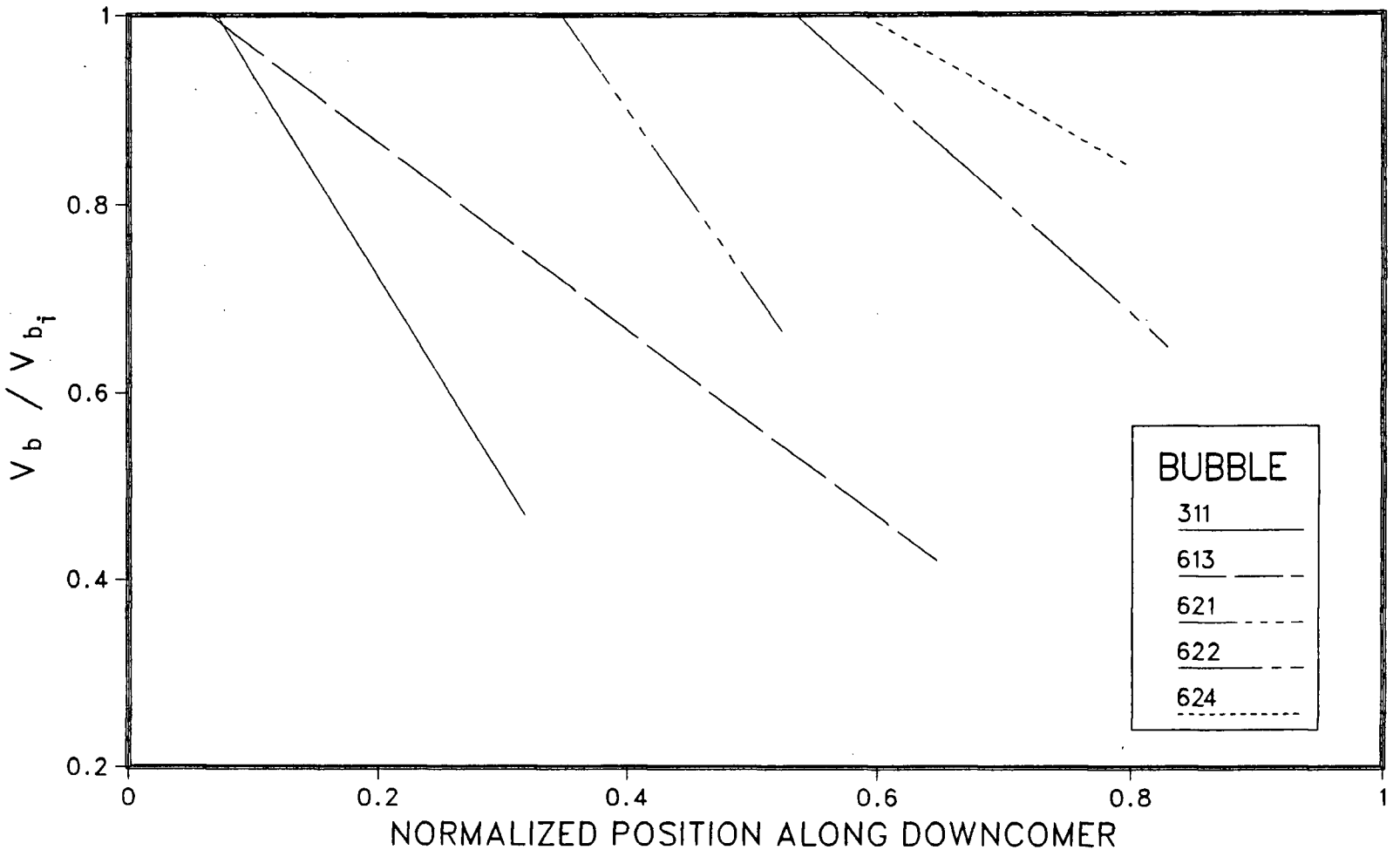

Fig. 5.5 Variation of the Bubble Volume with Normalized Position: T_ℓ = 11 °C

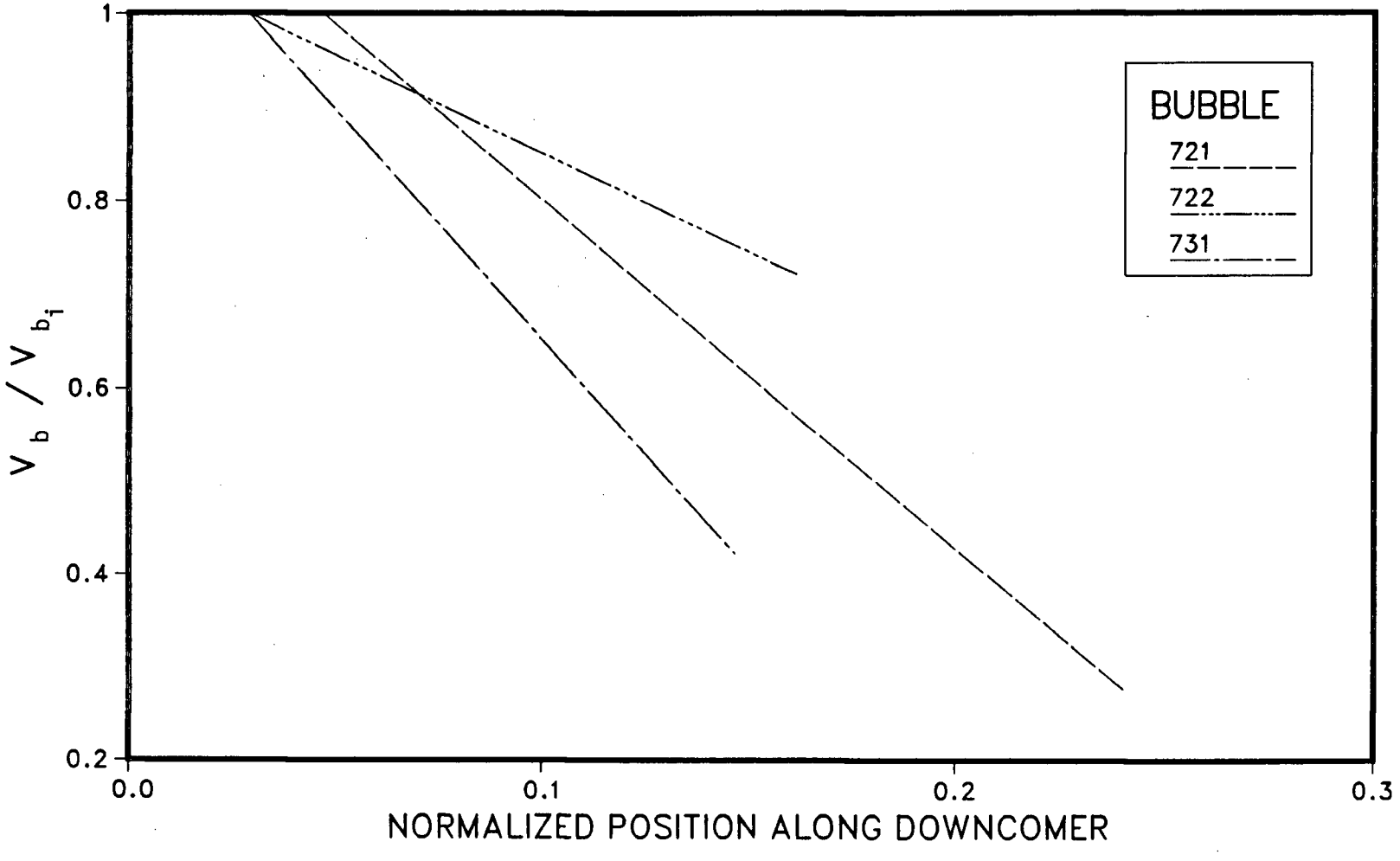

Fig. 5.6 Variation of the Bubble Volume with Normalized Position: T_ℓ = 12 °C

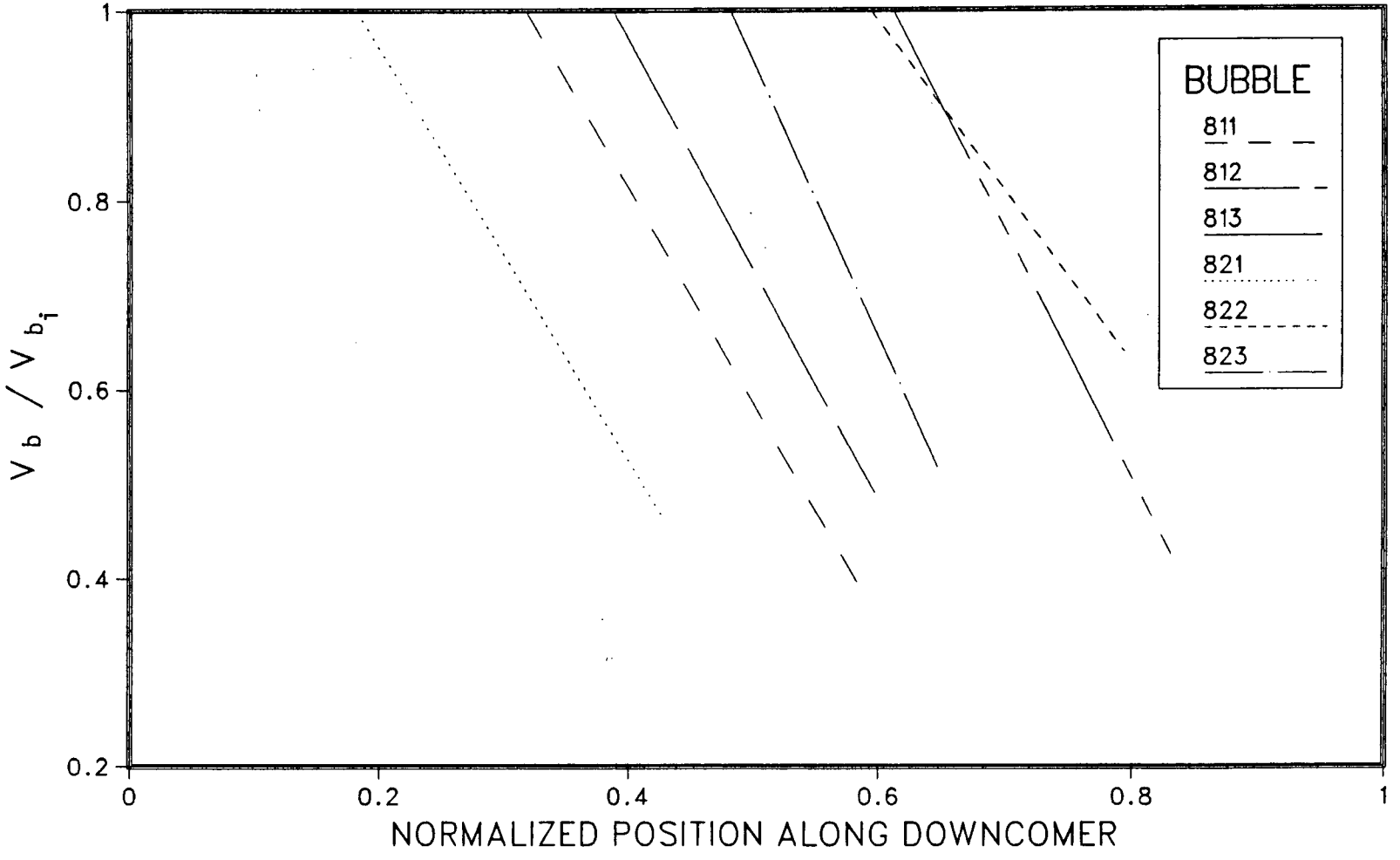

Fig. 5.7 Variation of the Bubble Volume with Normalized Position: T_ℓ = 13 °C

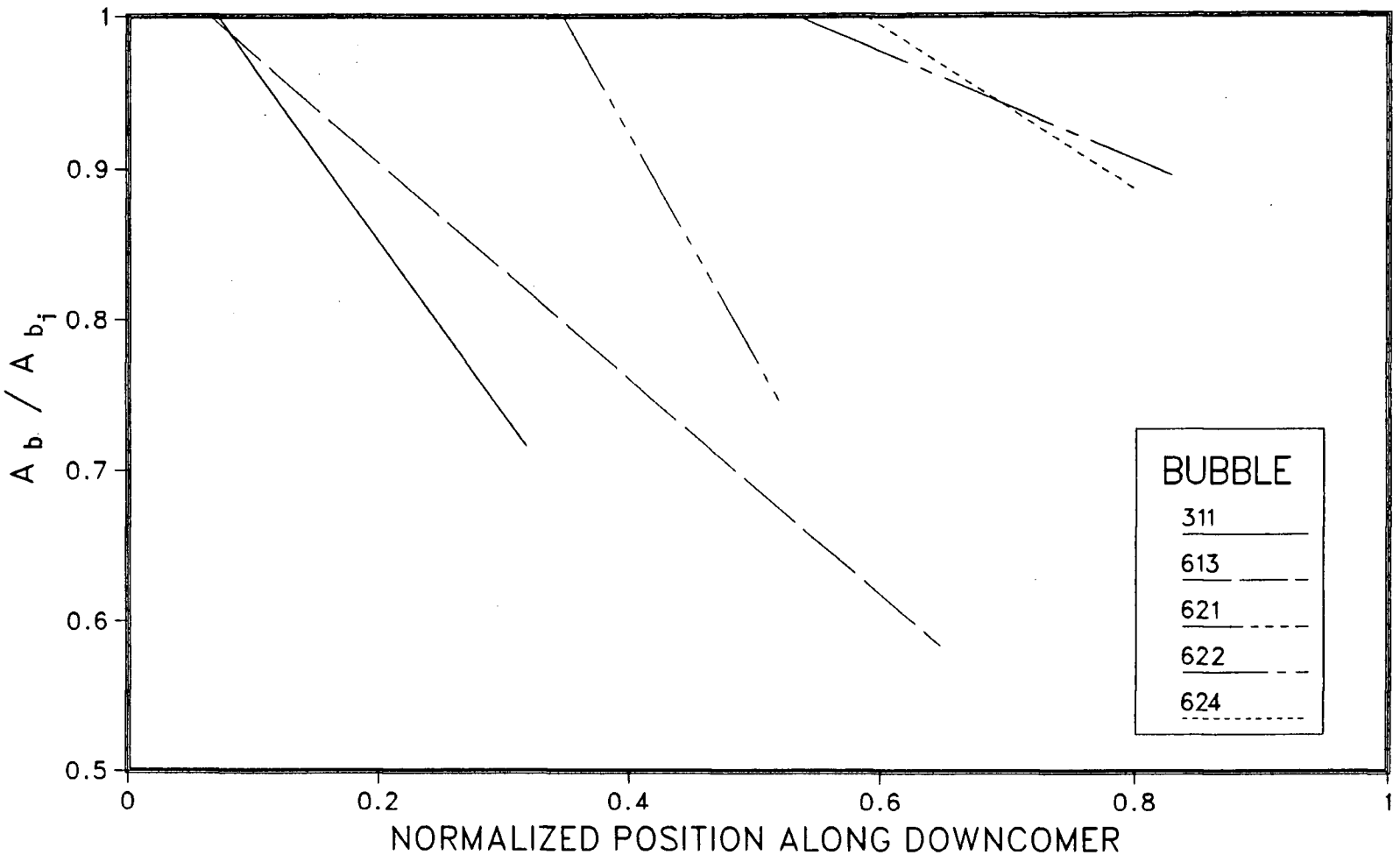

Fig. 5.8 Variation of the Bubble Surface Area with Normalized Position: T_ℓ = 11 °C

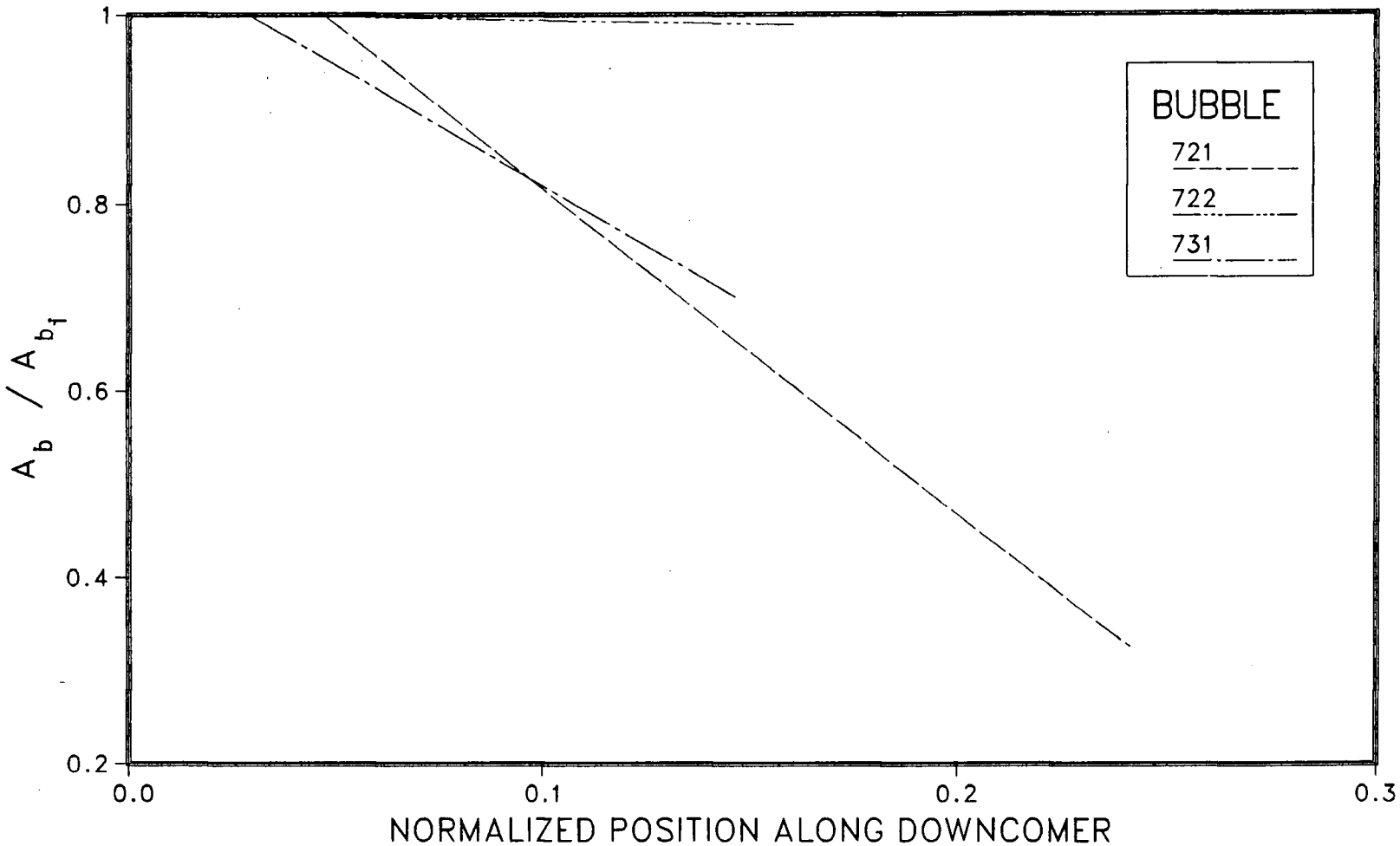

Fig. 5.9 Variation of the Bubble Surface Area with Normalized Position: T_ℓ = 12 °C

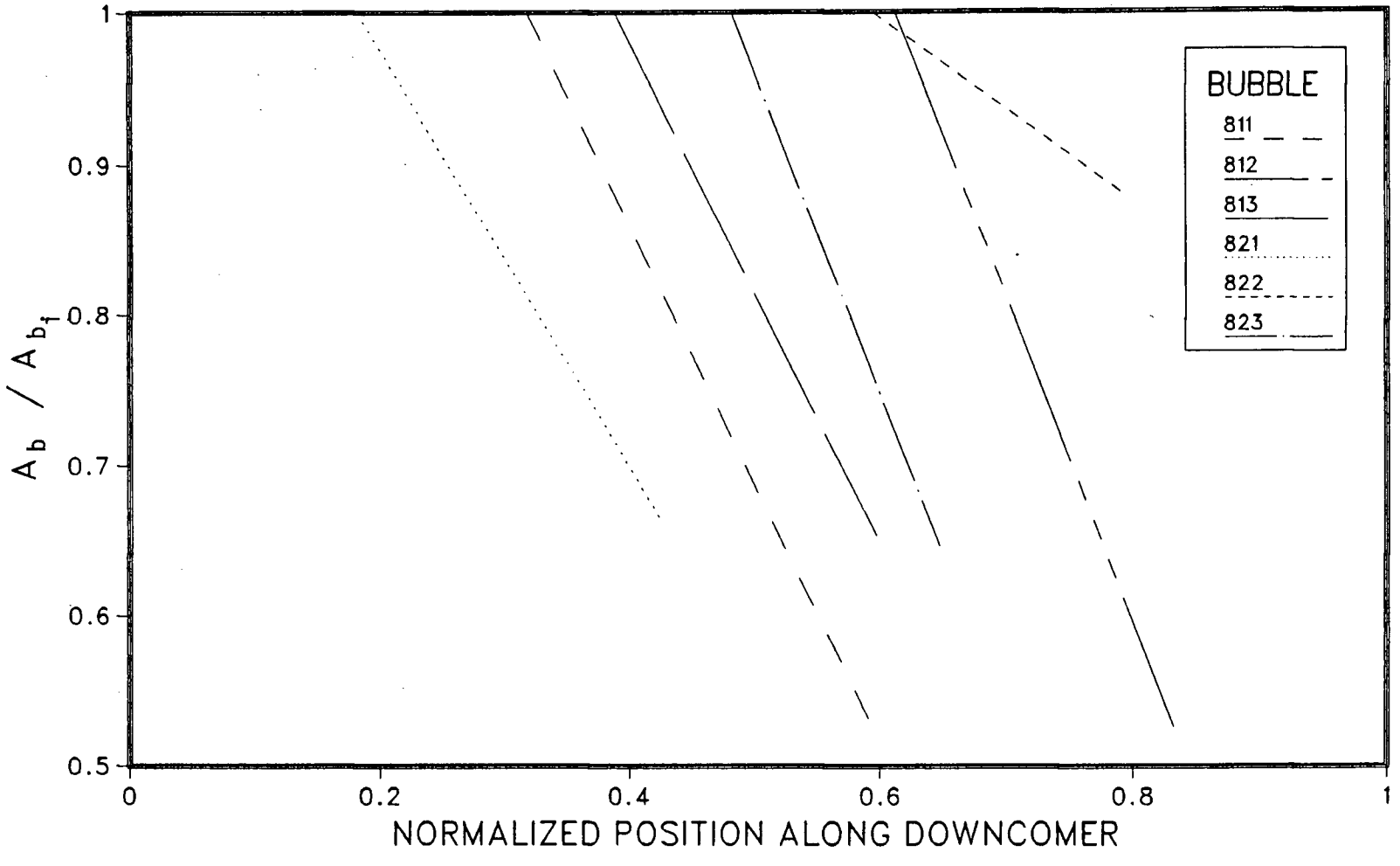

Fig. 5.10 Variation of the Bubble Surface Area with Normalized Position: T_ℓ = 13 °C

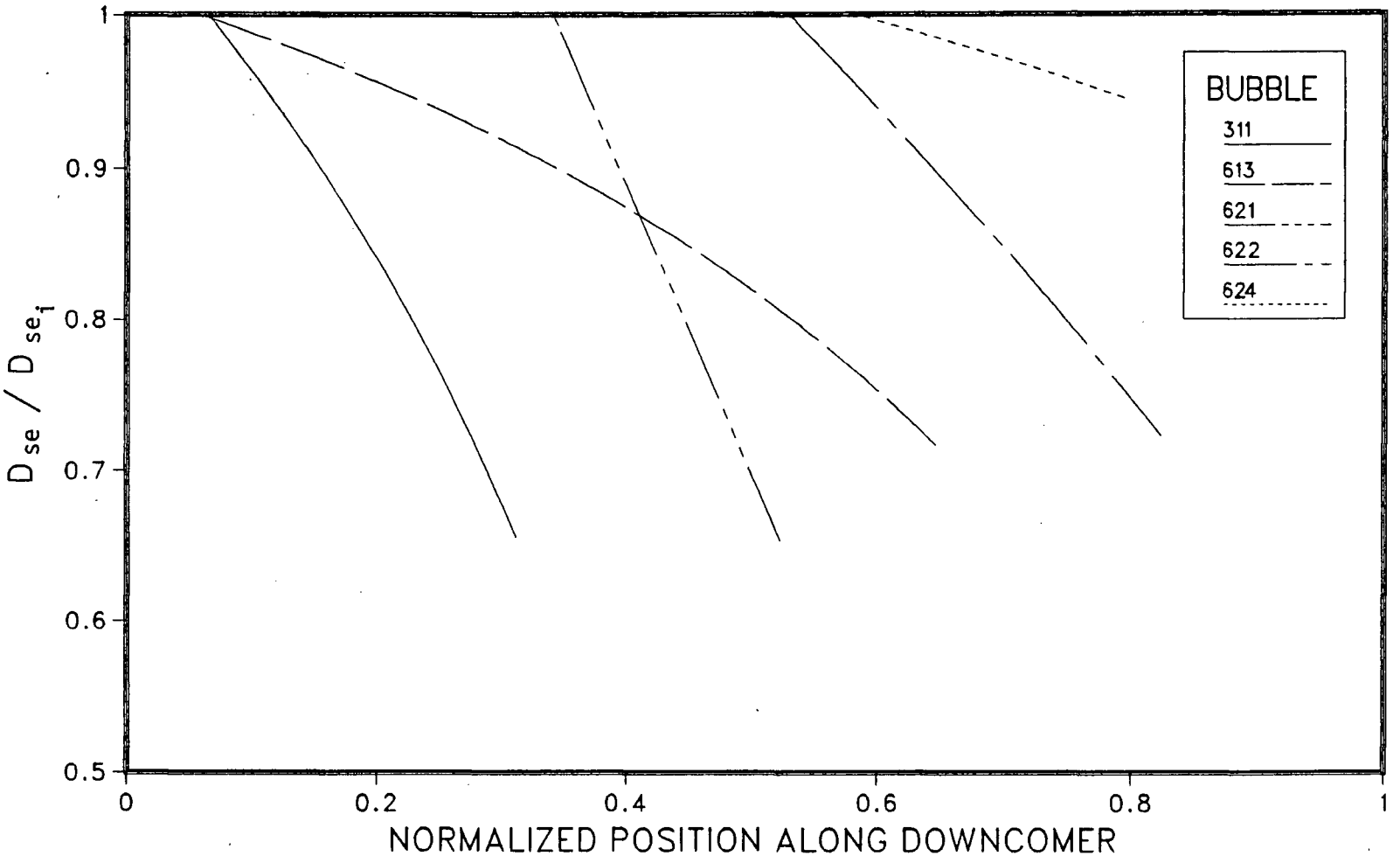

Fig. 5.11 Variation of the Bubble Spherical Equivalent Diameter with Normalized Position: T_ℓ = 11 °C

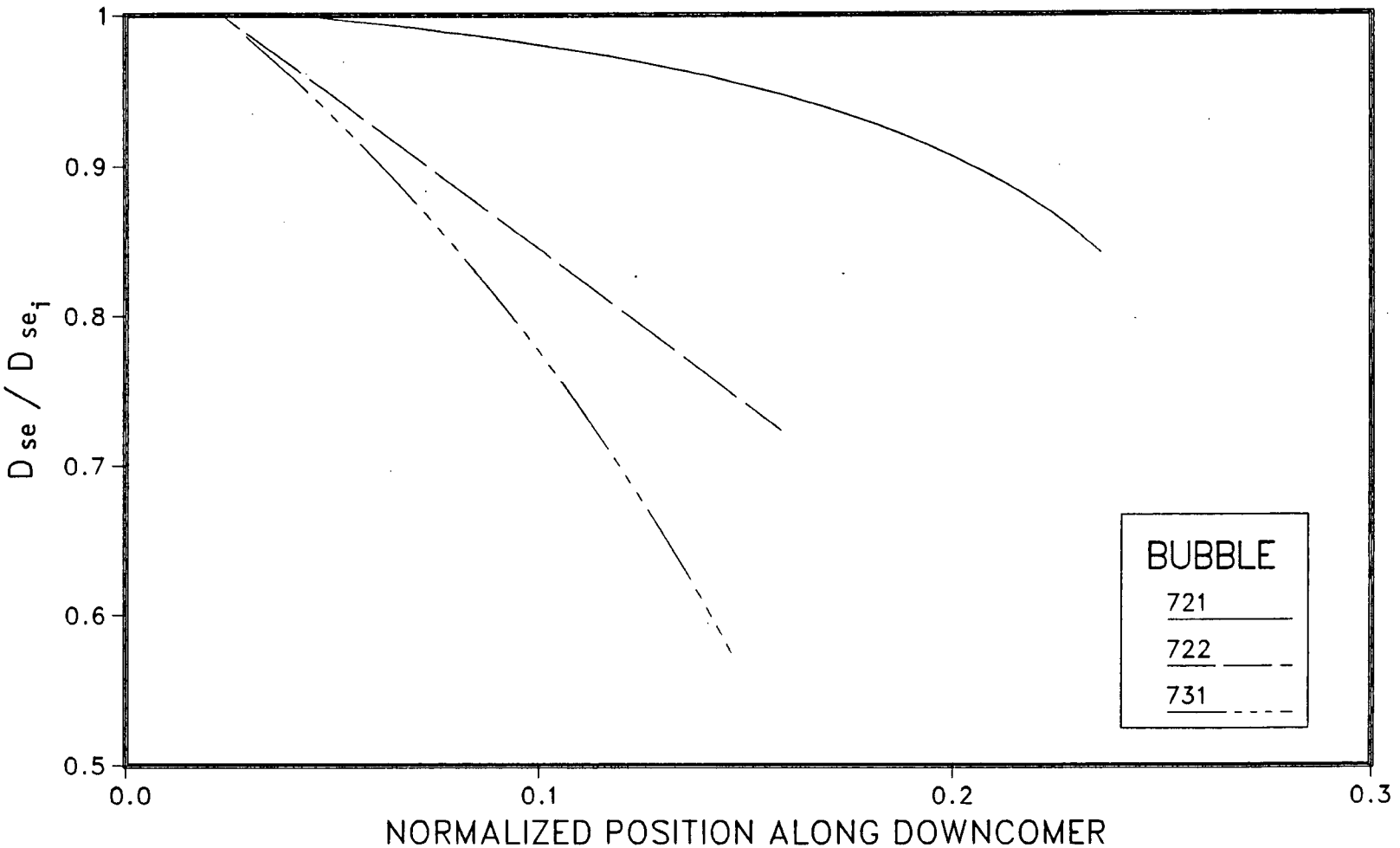

Fig. 5.12 Variation of the Bubble Spherical Equivalent Diameter with Normalized Position: T_ℓ = 12 °C

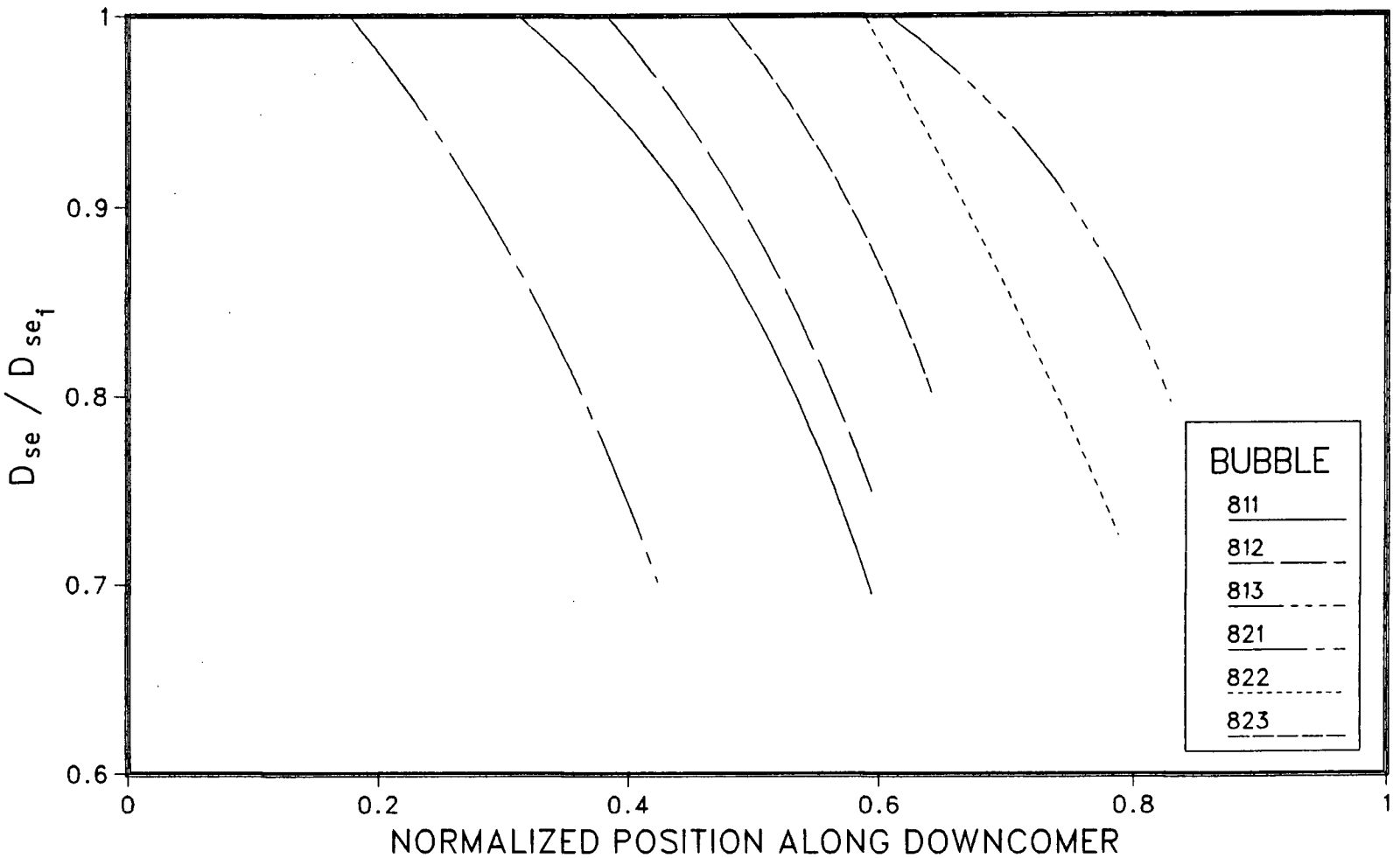

Fig. 5.13 Variation of the Bubble Spherical Equivalent Diameter with Normalized Position: T_ℓ = 13 °C

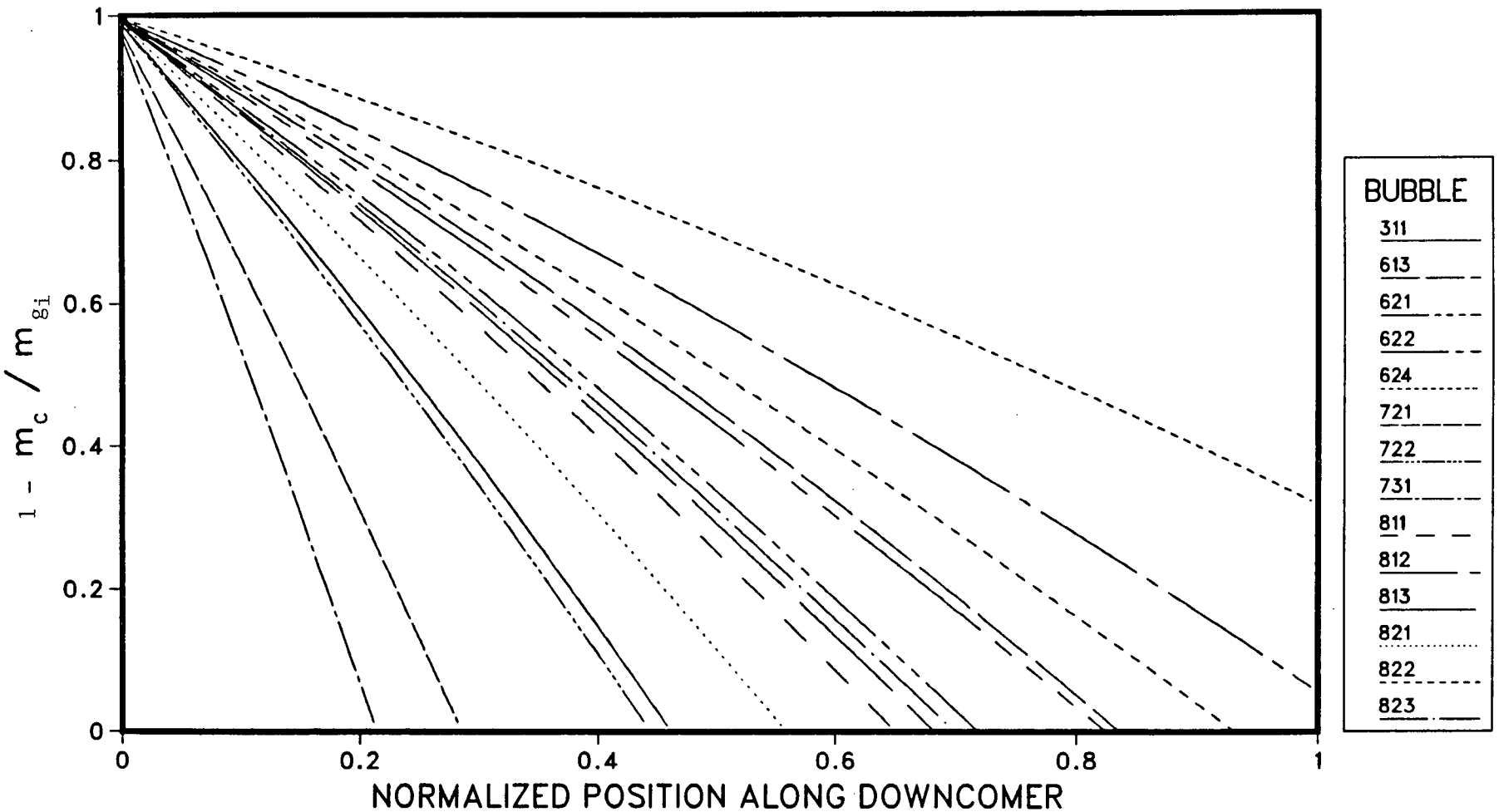

Fig. 5.14 Variation of the Bubble Condensation Mass Loss with Normalized Position: All Bubbles

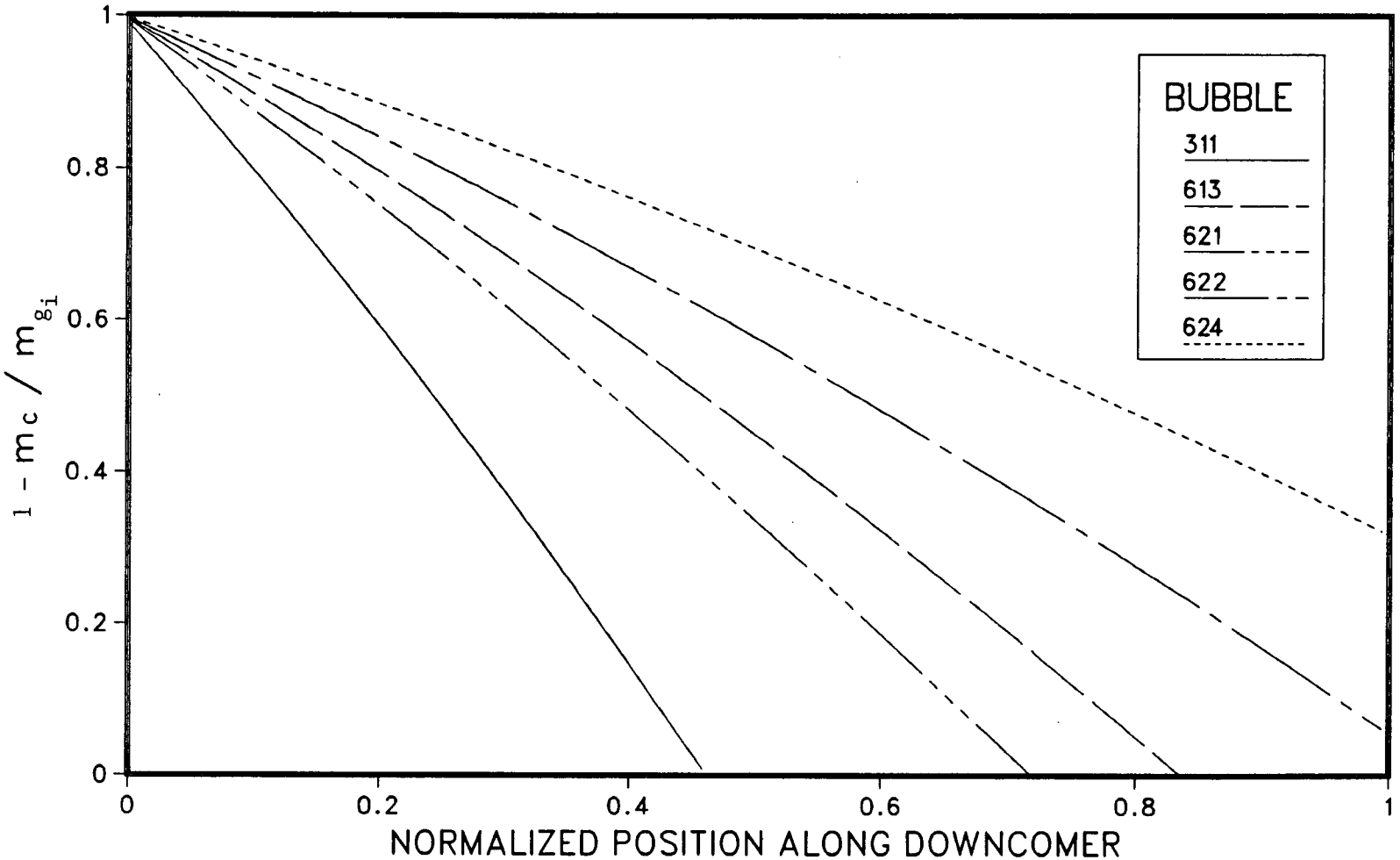

Fig. 5.15 Variation of the Bubble Condensation Mass Loss with Normalized Position: T_ℓ = 11 °C

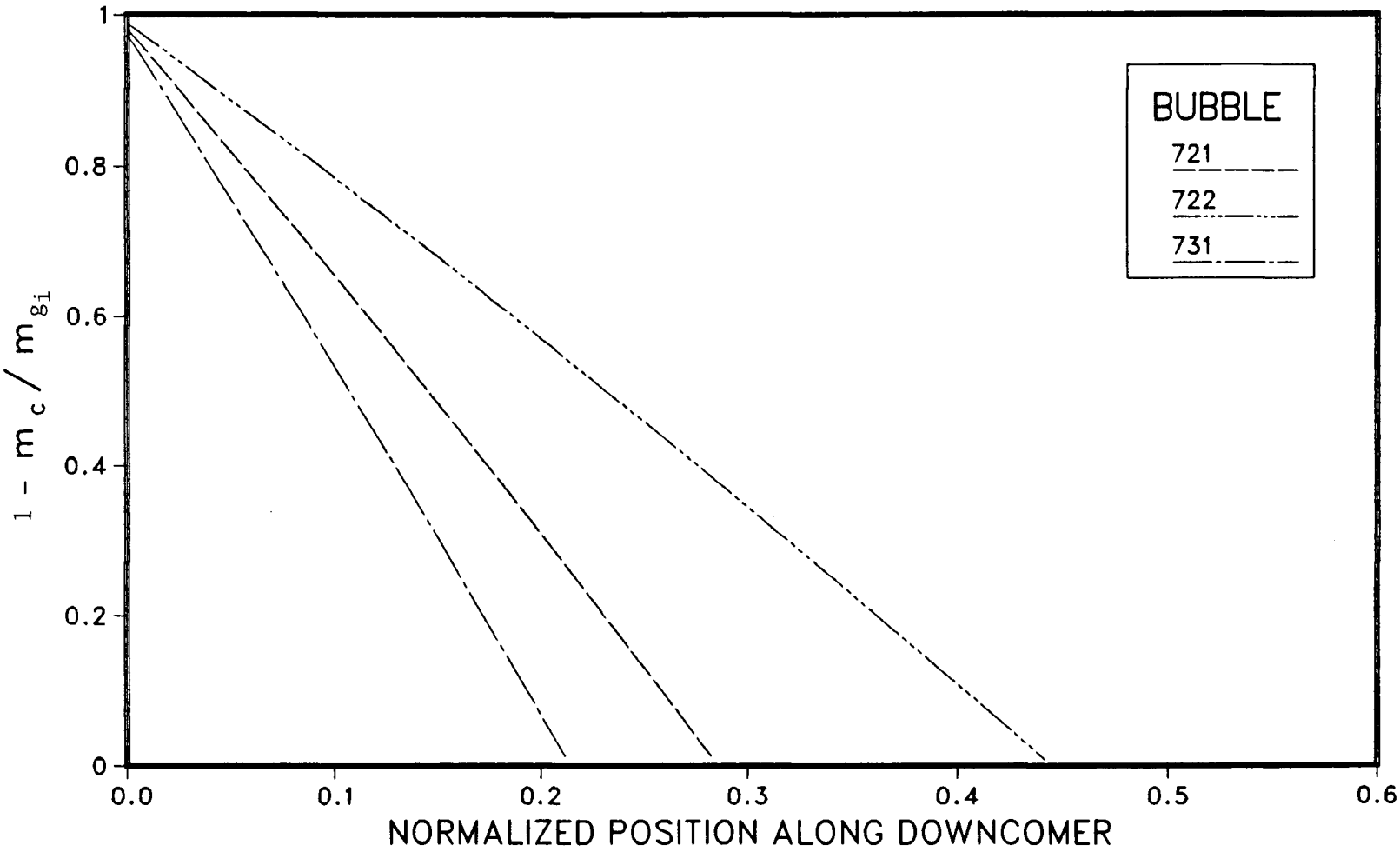

Fig. 5.16 Variation of the Bubble Condensation Mass Loss with Normalized Position: T_ℓ = 12 °C

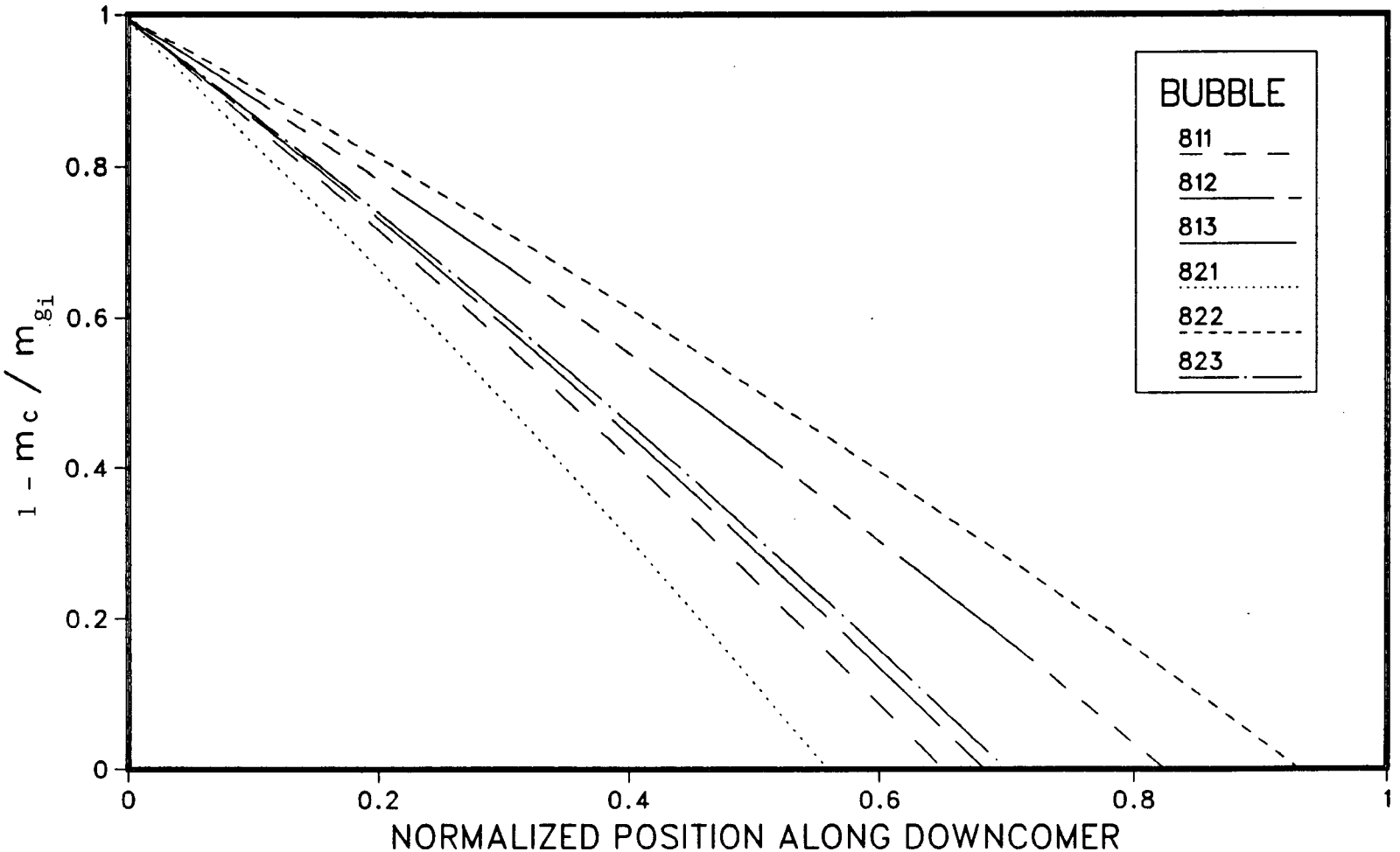

Fig. 5.17 Variation of the Bubble Condensation Mass Loss with Normalized Position: T_ℓ = 13 °C

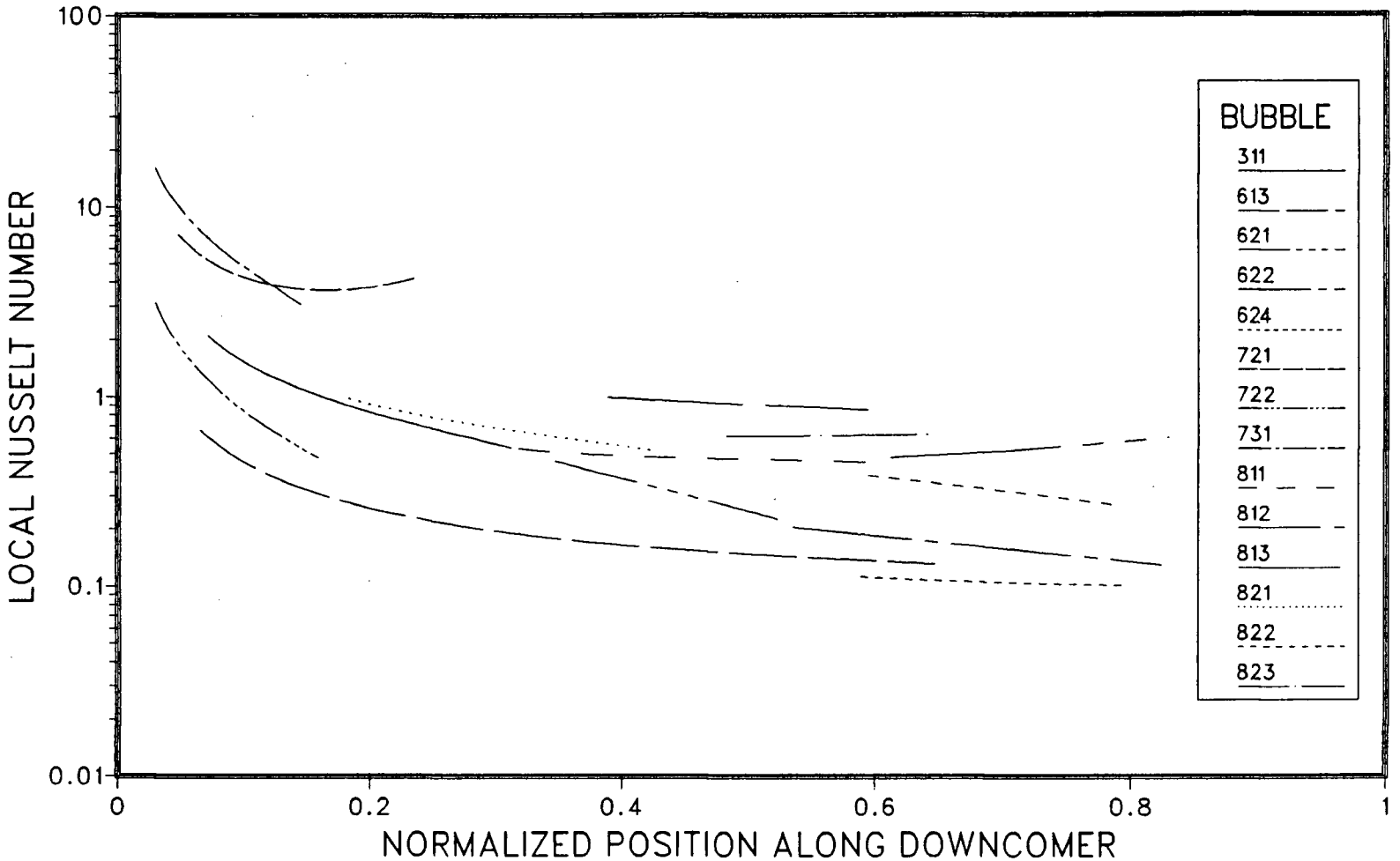

Fig. 5.18 Variation of the Local External Nusselt Number with Normalized Position: All Bubbles

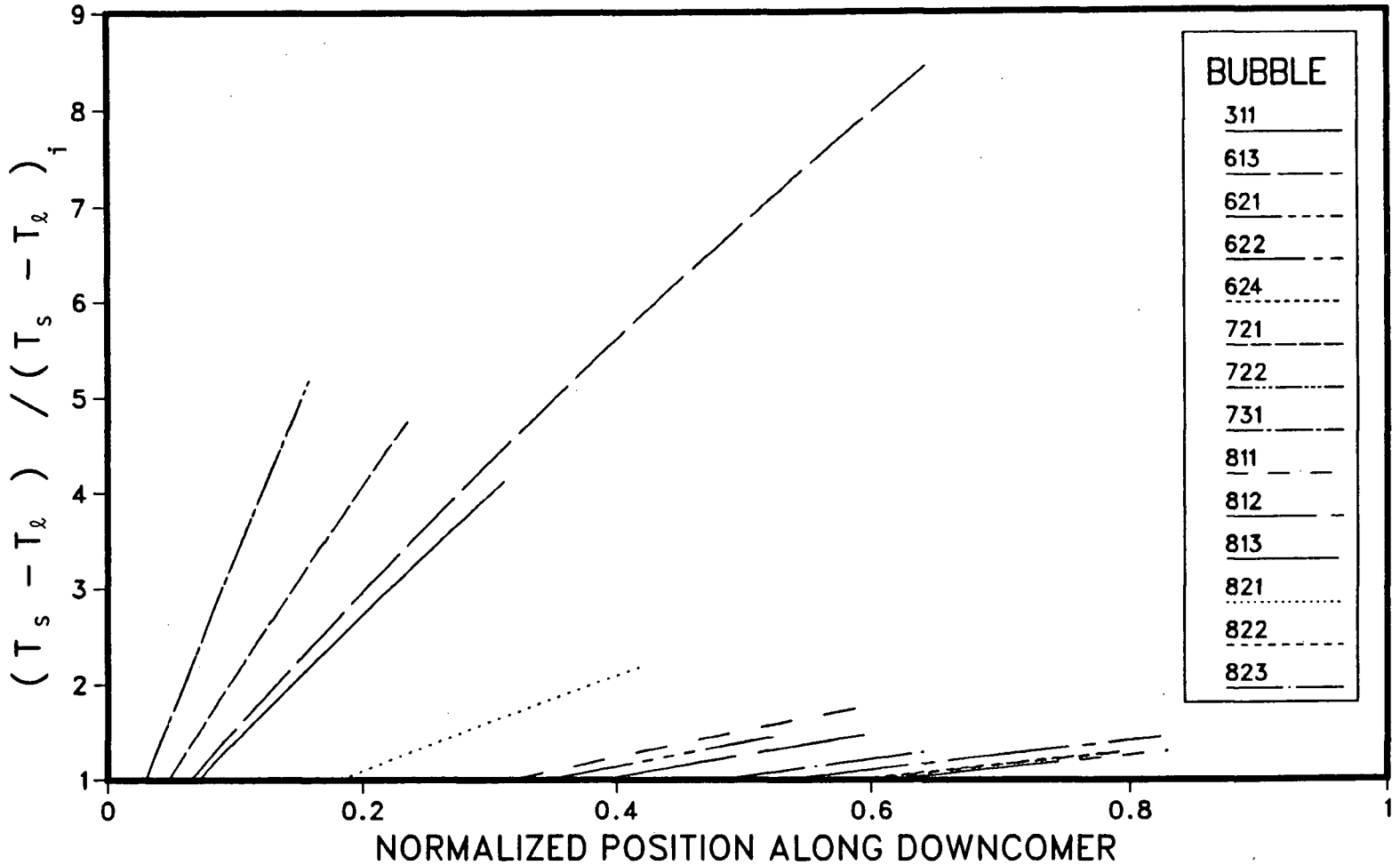

Fig. 5.19 Variation of the Dimensionless Driving Temperature Difference with Normalized Position: All Bubbles

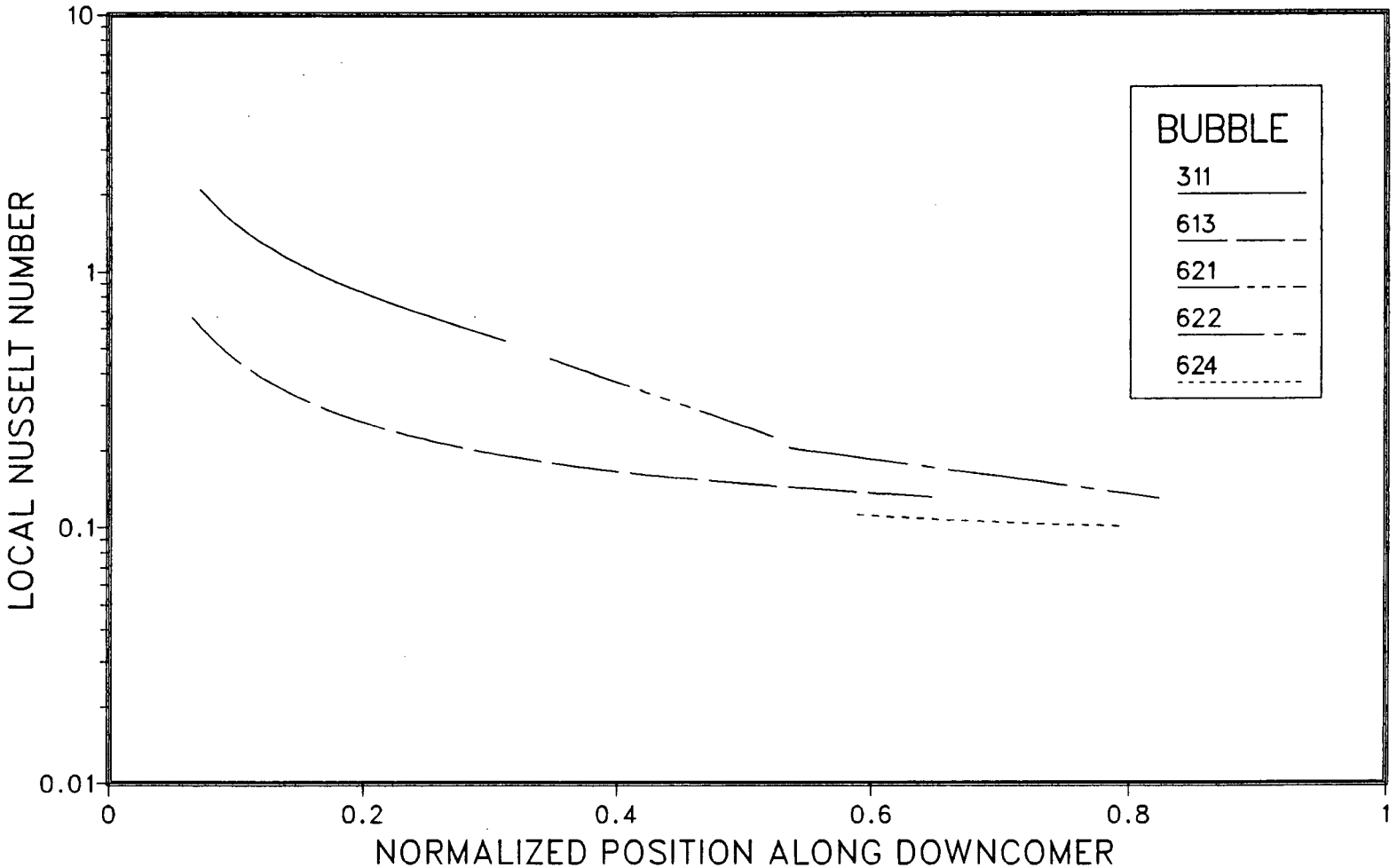

Fig. 5.20 Variation of the Local External Nusselt Number with Normalized Position: T_ℓ = 11 °C

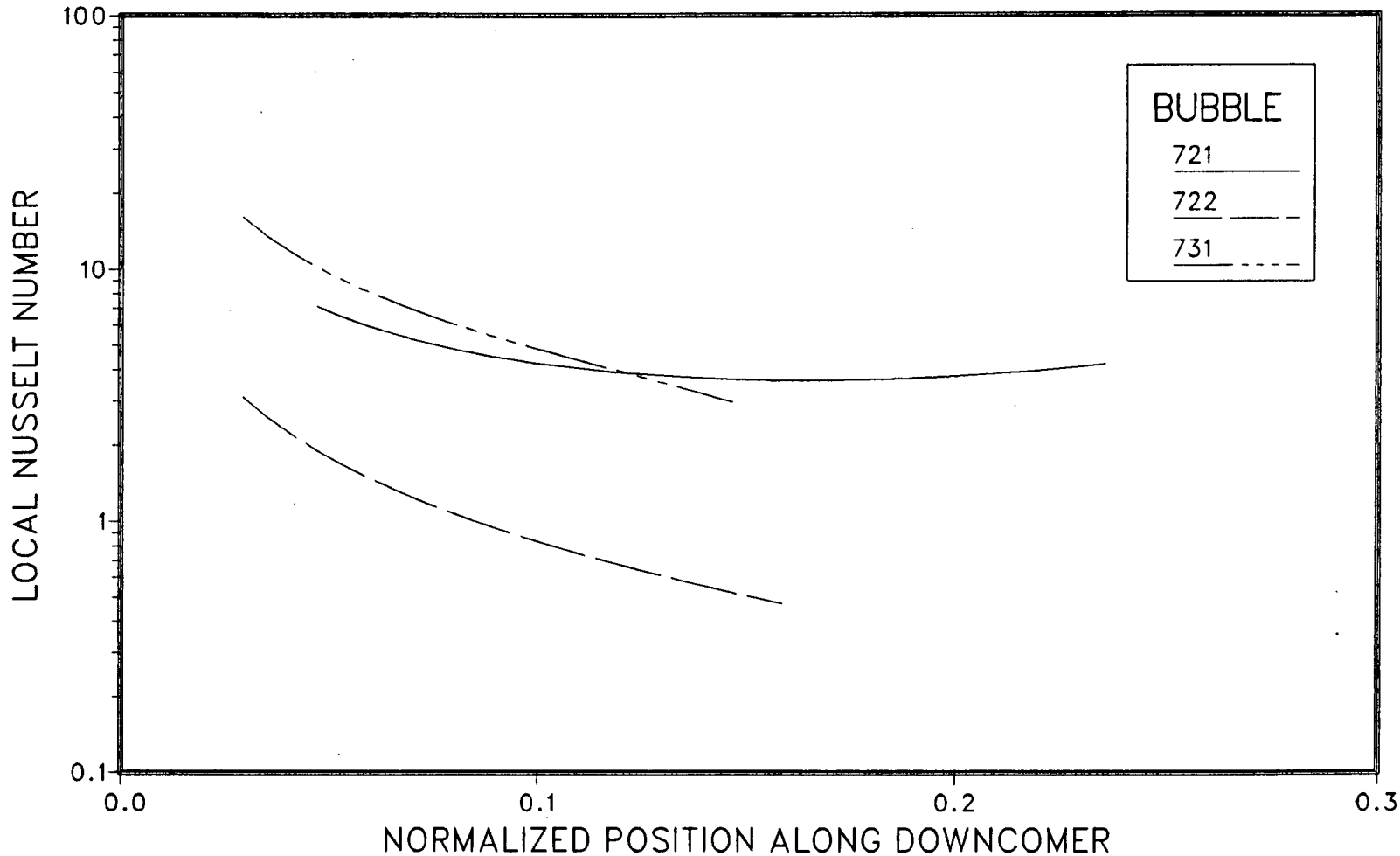

Fig. 5.21 Variation of the Local External Nusselt Number with Normalized Position: T_{ℓ} = 12 °C

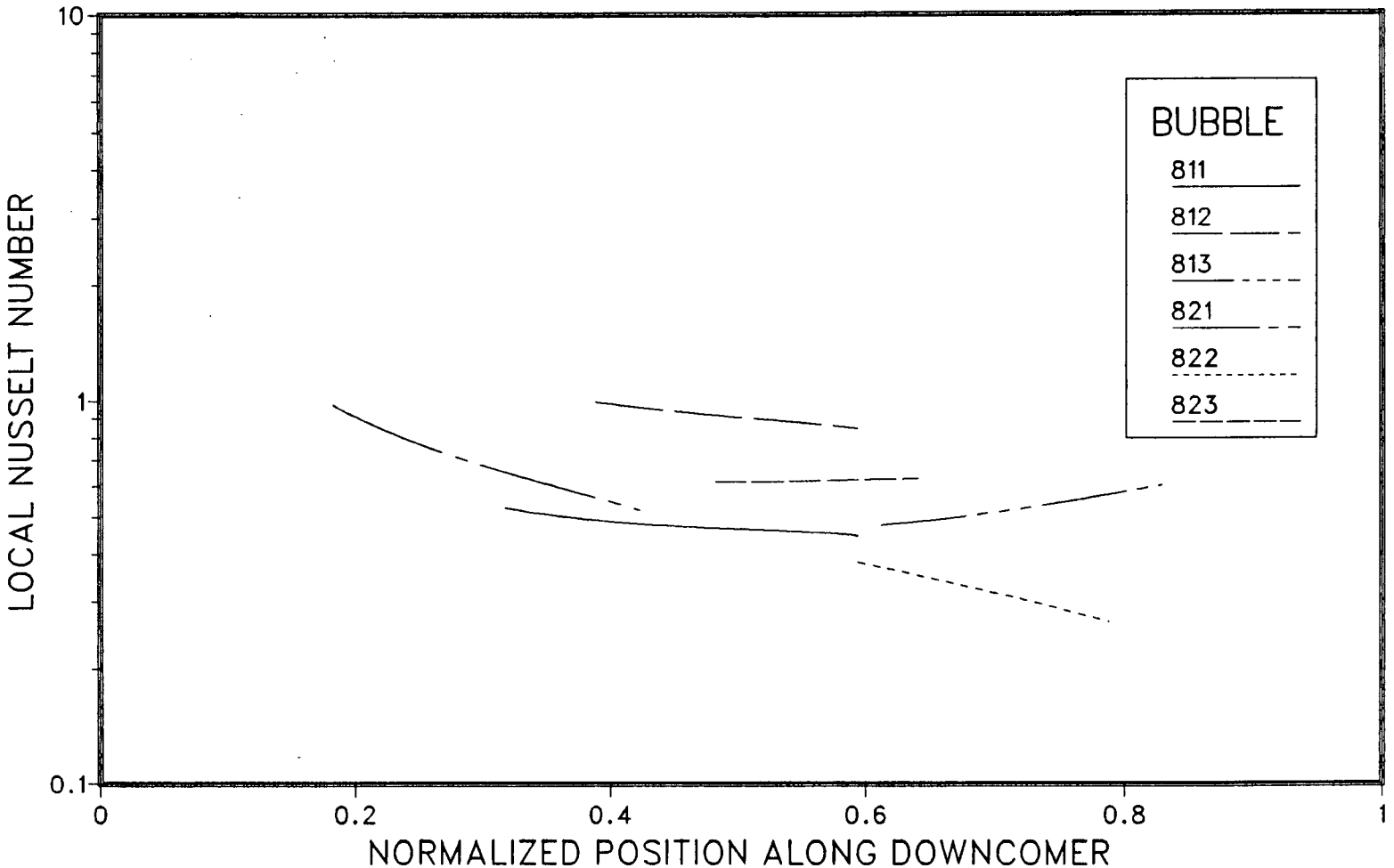

Fig. 5.22 Variation of the Local External Nusselt Number with Normalized Position: T_ℓ = 13 °C

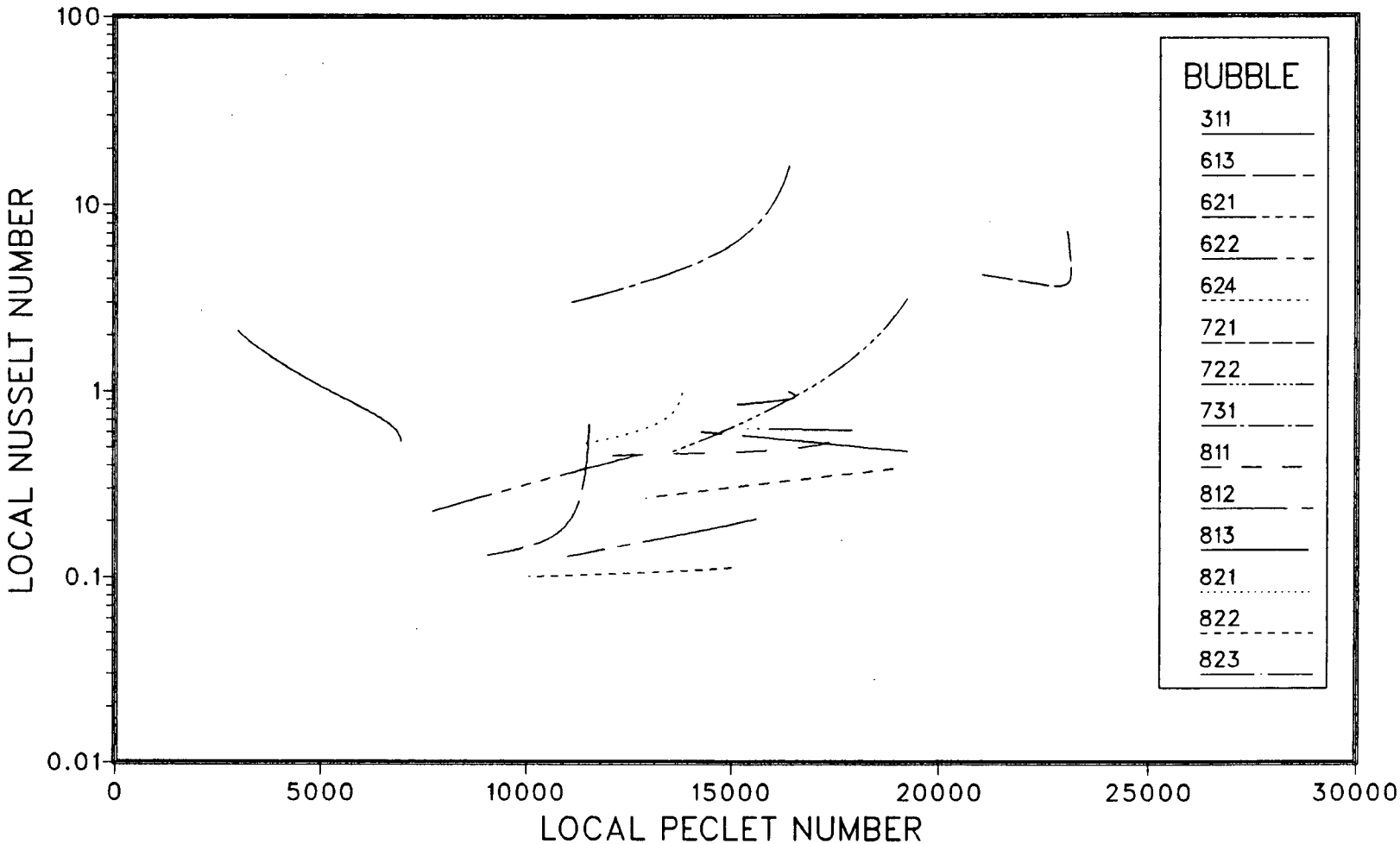

Fig. 5.23 Variation of the Local External Nusselt Number with the Nominal Relative Peclet Number

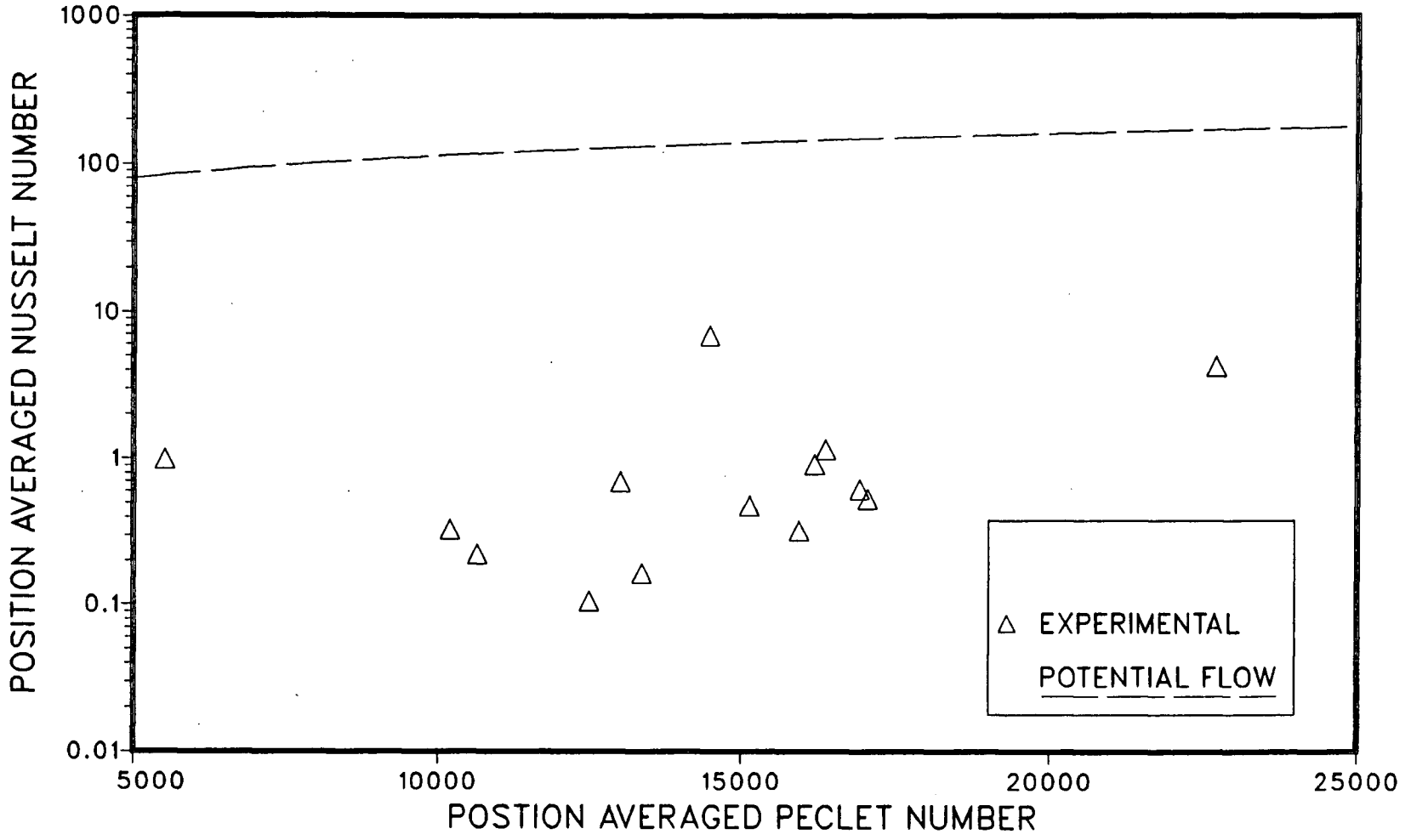

Fig. 5.24 Variation of the Position Averaged Nusselt Number with the Position Averaged Peclet Number

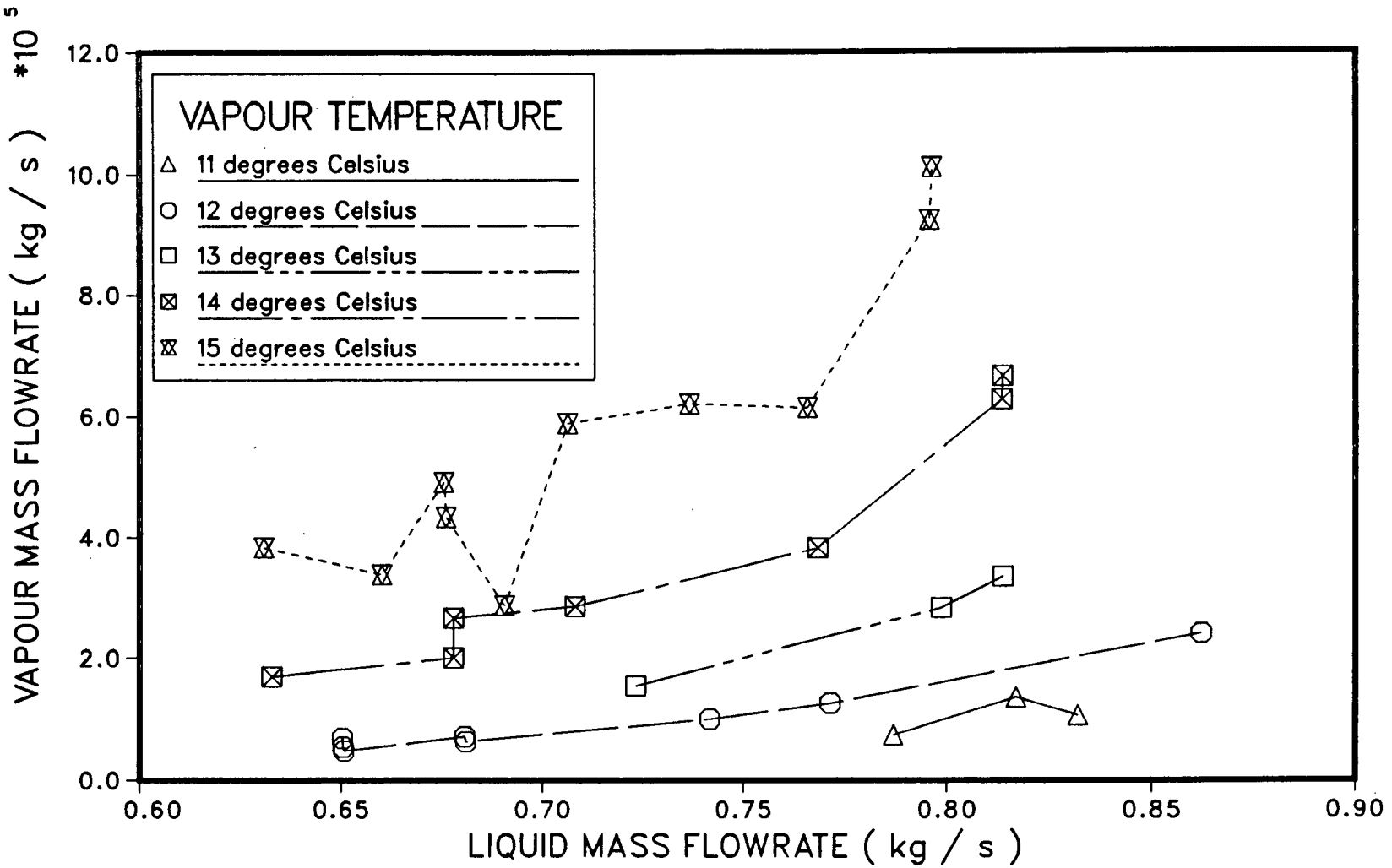

Fig. 5.25 Variation of the Vapour Mass Flowrate with the Liquid Mass Flowrate

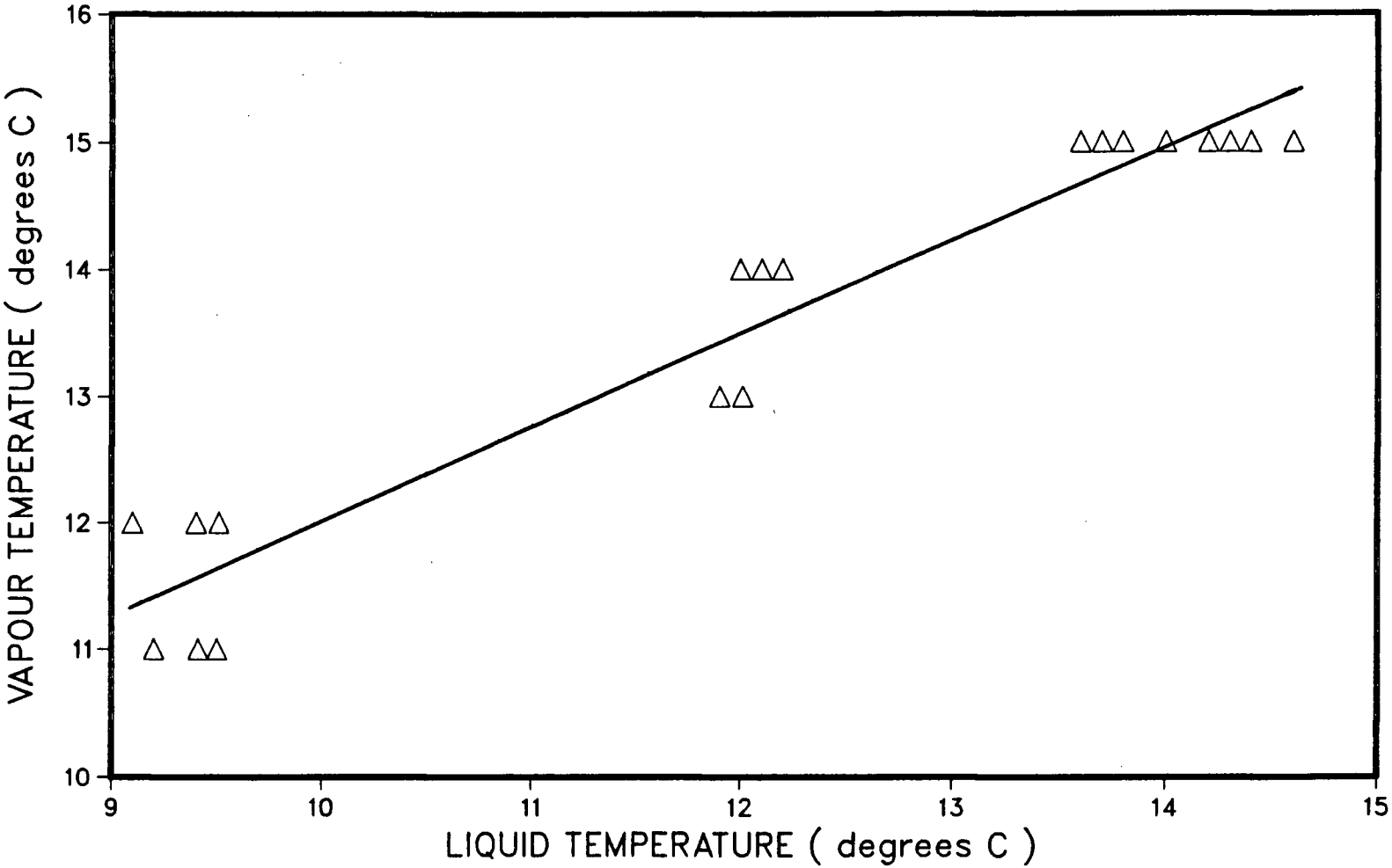

Fig. 5.26 Variation of the Inlet Liquid Temperature with the Outlet Vapour Temperature

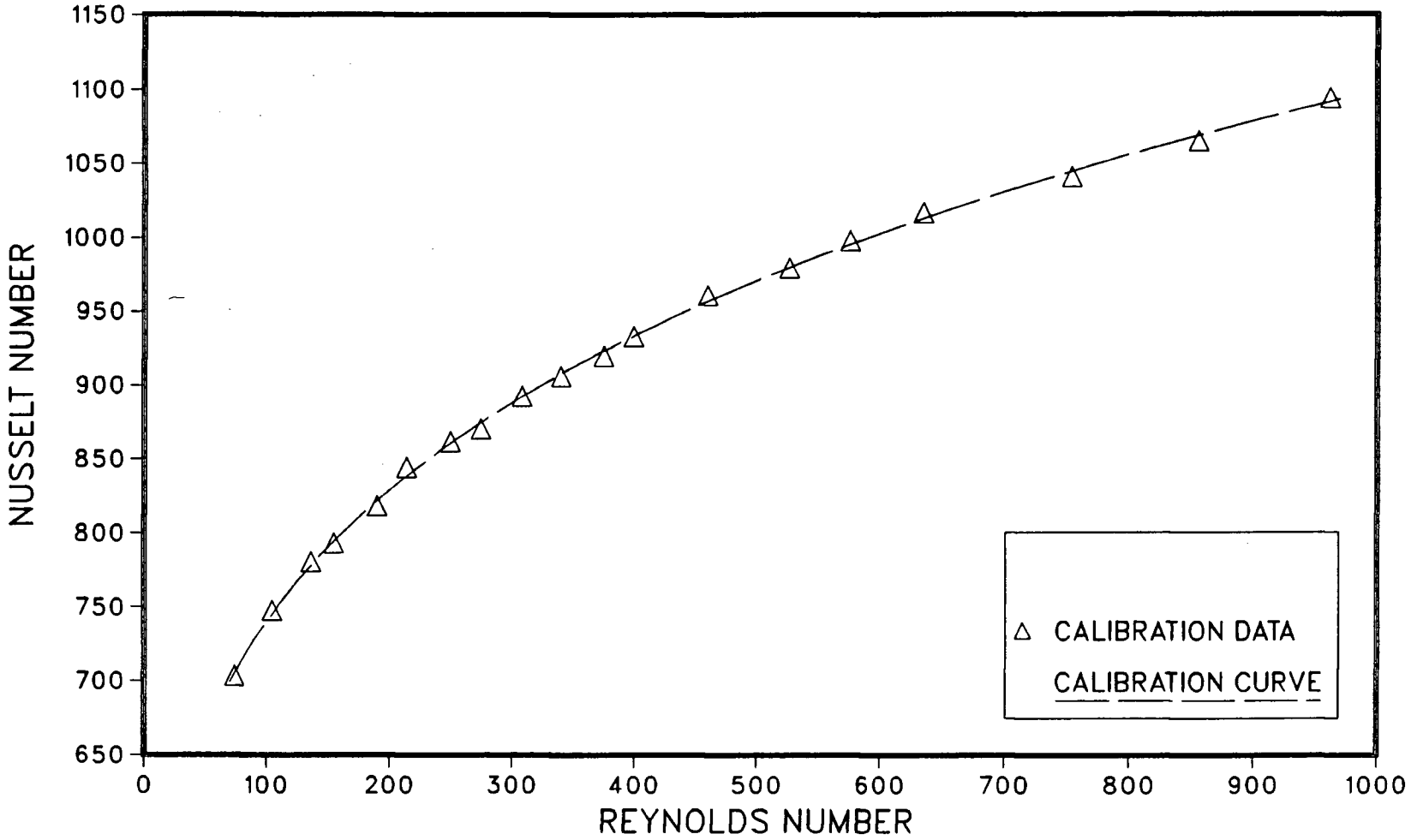

Fig. A.1 Hot Film Probe Calibration Curve

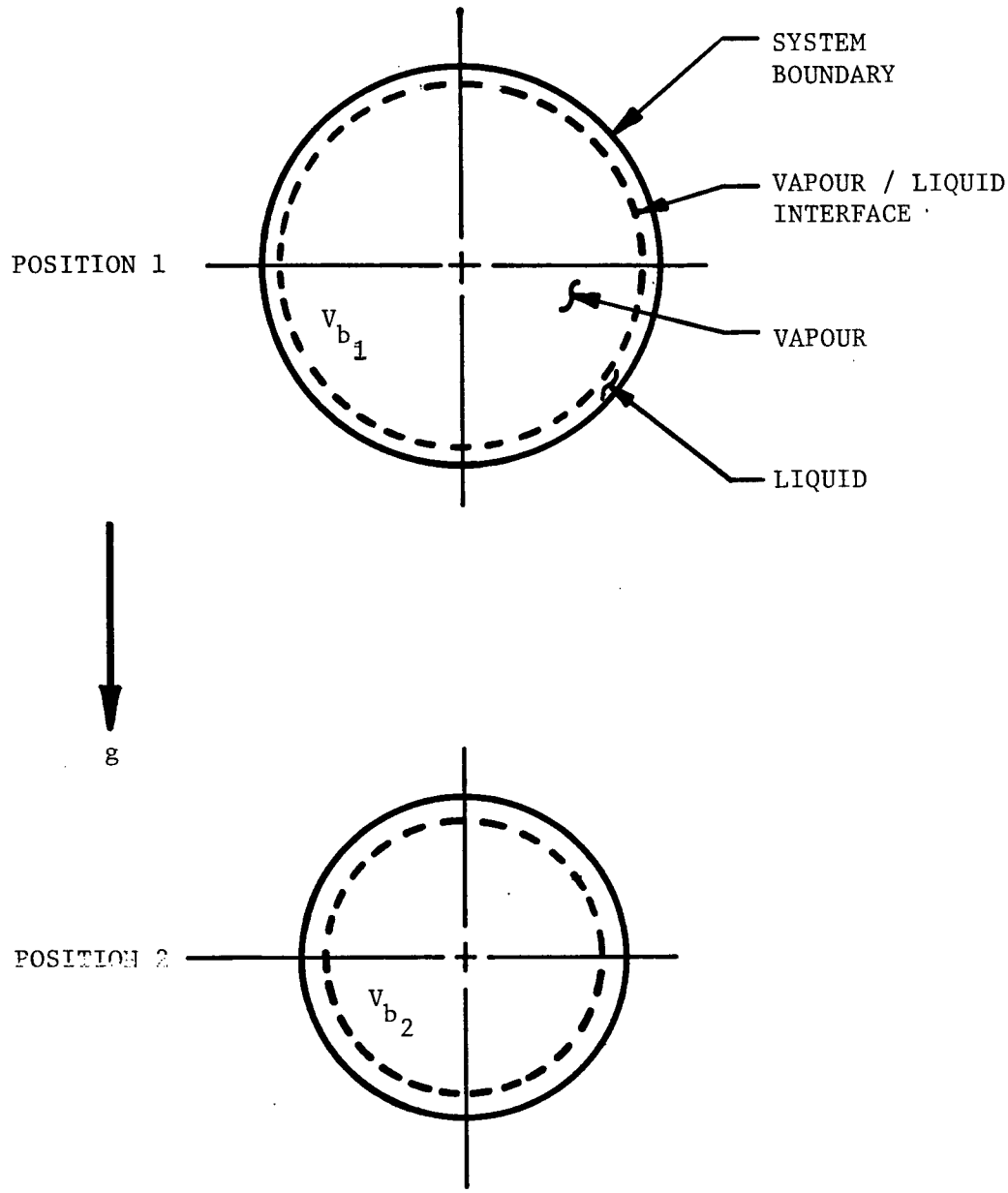

Fig. B.1 Schematic of the Bubble Compression Process.

Bubble	p_{vc} (kPa)	p_{st} (kPa)	Q_{ℓ} (ℓ/s)	T_e (°C)	$(z)_i$ (cm)	$(z)_f$ (cm)
311	80.50	107.18	0.36	11.3	12.0	54.0
613	80.08	107.08	0.36	10.9	11.0	110.0
621	75.57	102.10	0.47	10.9	59.0	89.0
622	75.57	102.10	0.47	10.9	91.0	141.0
624	75.57	102.10	0.47	10.9	100.0	136.0
721	76.66	104.00	0.32	12.0	8.0	41.0
722	76.66	104.00	0.32	12.0	5.0	27.5
811	76.61	104.03	0.50	13.1	54.0	101.0
812	76.61	104.03	0.50	13.1	66.0	101.5
813	76.61	104.03	0.50	13.1	104.0	141.5
821	78.94	105.53	0.42	13.3	31.0	72.5
822	78.94	105.53	0.42	13.3	101.0	135.0
823	78.94	105.53	0.42	13.3	82.0	110.0

Table 1. Experimental Data for the Bubble Photography Tests

Run	p_{vc} (kPa)	p_{st} (kPa)	Q_{ℓ} (ℓ/s)	T_e (°C)	T_g (°C)
1	74.65	101.90	0.57	9.5	12.0
2	74.45	101.75	0.54	9.5	11.0
3	75.83	103.24	0.51	9.4	12.0
4	78.08	105.14	0.43	9.4	12.0
5	77.89	105.29	0.43	9.5	12.0
6	77.69	105.04	0.45	9.4	12.0
7	74.55	101.80	0.54	12.2	14.0
8	74.45	101.60	0.54	12.1	14.0
9	76.38	103.69	0.47	12.0	14.0
10	77.10	104.84	0.45	12.0	14.0
11	74.26	101.50	0.53	11.9	13.0
12	74.45	101.65	0.53	14.3	15.0
13	75.14	102.35	0.51	14.2	15.0
14	77.30	104.39	0.45	14.4	15.0
15	77.65	104.69	0.44	14.6	15.0
16	77.10	104.09	0.46	14.3	15.0
17	75.37	102.77	0.55	9.4	11.0
18	77.13	104.31	0.52	9.2	11.0
19	77.58	105.06	0.49	9.1	12.0
20	78.96	106.30	0.45	9.1	12.0
21	79.54	106.90	0.43	9.1	12.0
22	75.58	102.77	0.54	12.0	13.0
23	76.74	103.91	0.51	12.0	14.0
24	77.82	104.91	0.48	12.0	13.0
25	78.66	105.86	0.45	12.0	14.0
26	79.27	106.31	0.42	12.0	14.0
27	76.82	103.17	0.53	13.8	15.0
28	79.70	104.76	0.47	13.7	15.0
29	77.01	104.16	0.49	13.6	15.0
30	79.01	106.01	0.42	14.0	15.0
31	78.44	105.31	0.45	13.8	15.0

Table 2. Experimental Data for the Vapour Mass Flowrate Tests

Bubble	$(A_b)_i$ (mm^2)	dA_b/dt (mm^2/s)	$(V_b)_i$ (mm^3)	dV_b/dt (mm^3/s)
311	18.50	- 5.34	5.34	- 2.88
613	25.56	- 2.75	7.73	- 1.16
621	17.57	- 6.11	5.04	- 2.26
622	16.05	- 1.12	4.94	- 1.16
624	20.03	- 2.40	5.50	- 0.94
721	53.96	- 29.48	20.03	- 11.78
722	13.11	- 0.15	3.73	- 1.06
731	12.08	- 7.08	3.84	- 4.33
811	24.96	- 7.22	6.92	- 2.65
812	23.48	- 8.96	8.06	- 4.47
813	22.77	- 8.59	6.93	- 3.19
821	31.39	- 7.08	10.09	- 3.59
822	20.15	- 1.79	7.47	- 1.98
823	21.81	- 6.15	7.90	- 3.04

Table 3. Data From the Linear Least Squares Fits of the Variation of the Bubble Surface Area and Volume with Time

Bubble	$\frac{(D_{se})_i}{(D_{sev})_i}$	$\bar{u}_g$ (m/s)	$\bar{u}_r$ (m/s)
311	0.799	0.43	0.33
613	0.740	0.26	0.50
621	0.809	0.40	0.59
622	0.874	0.33	0.66
624	0.752	0.38	0.61
721	0.661	0.27	0.72
722	0.887	0.23	0.84
731	0.982	0.39	0.68
811	0.704	0.29	0.79
812	0.828	0.39	0.66
813	0.772	0.30	0.76
821	0.719	0.28	0.78
822	0.917	0.25	0.80
823	0.880	0.22	0.83

Table 4. Calculated Data for the Bubble Photography Tests

Anemometer model	: TSI 1010A	
Bridge setting	: high sensitivity	
Bridge series resistance		R_3 = 40.0 ohms
Bridge standby voltage		= 3.1 volts
Probe model	: TSI 1235W parabolic hot film wedge	
Probe sensing area length		L_f = 1.016 mm
Probe sensing area width		W_f = 10.16 mm
Probe resistance at 0 °C (TSI specified)		= 6.47 ohms
Probe cold resistance (measured)		R_c = 6.76 ohms
Probe oprating resistance used		R_o = 7.44 ohms
Probe operating temperature used		T_p = 6.41 °C
Probe overheat ratio used		= 1.15

Table A.1. Hot Film Anemometry Details

Ambient pressure		± 100 Pa
Downcomer inlet liquid temperature	T_{ℓ}	± 0.2 °C
Separation tank vapour temperature	T_{g}	± 1.0 °C
Vacuum chamber pressure	p_{vc}	± 500 Pa
Separation tank pressure	p_{st}	± 500 Pa
Downcomer inlet liquid flowrate	Q_{ℓ}	± 0.005 l/s
Separation Tank Liquid depth	h_{st}	± 2 mm

Table C.1. Experimental Errors